Elemental composition and chemical evolution of geologic materials in Gale crater, Mars: APXS results from Bradbury Landing to the Vera Rubin Ridge

Jeff A. Berger[1*], R. Gellert[1], N. I. Boyd[1], P. L. King[2], M. A. McCraig[1], C. D. O'Connell-Cooper[3], M. E. Schmidt[4], J. G. Spray[3], L. M. Thompson[3], S. J. V. VanBommel[5], A. S. Yen[6]

[1]University of Guelph, Canada
[2]Australian National University, Australia
[3]University of New Brunswick, Canada
[4]Brock University, Canada
[5]Washington University in St. Louis, USA
[6]JPL-Caltech, USA

*Corresponding author now at NASA Johnson Space Center, USA, jeffrey.a.berger@nasa.gov

Keywords

MSL APXS

Mars surface geochemistry

Gale crater

Composition of the martian surface

Key Points

- APXS results from the first 2301 sols of the *Curiosity* Mars rover mission are presented
- Stratigraphic context of APXS targets in Gale crater is defined
- Gale crater sediment has a diverse provenance
- Alteration and diagenetic features demonstrate widespread aqueous activity

Plain Language Summary

The Mars rover, *Curiosity*, uses the Alpha Particle X-ray Spectrometer (APXS) located on *Curiosity*'s robotic arm to determine the composition of surface materials at the Mars Science Laboratory (MSL) landing site in Gale crater. The APXS has measured more than 700 2-cm-wide spots over a >20 km traverse during 2301 martian days, or 6.5 Earth years. This work presents those APXS data acquired to date, and an overview of the results from this period of *Curiosity'*s mission. The APXS results demonstrate that the geologic materials in Gale crater have diverse elemental compositions and include several broad groups. Most of the bedrock is made of small grains of rock transported by surface processes that may include fluvial, aeolian, impact, volcanic, and mass wasting into a lake system where they were deposited and cemented. Many of the bedrock layers show evidence for aqueous and diagenetic processes that can be traced using soluble elements in the rocks, veins, and concretions. We show that the elemental characteristics are consistent with bedrock alteration by acidic as well as neutral and/or alkaline waters. These results are key to the goal of *Curiosity*'s mission to determine if Gale crater had an environment where microbial life could have emerged.

Abstract

The Alpha Particle X-ray Spectrometer (APXS) on the rover, *Curiosity*, has analyzed the composition of geologic materials along a >20-kilometer traverse in Gale crater on Mars. The APXS dataset after 6.5 Earth years (2301 sols) includes 712 analyses of soil, sand, float, bedrock, and drilled/scooped fines. We present the APXS results over this duration and provide stratigraphic context for each target. We identify the best APXS analysis of each of the 22 drilled and scooped samples that were delivered to the instruments CheMin (X-ray diffractometer) and SAM (mass spectrometer and gas chromatograph) during this period. The APXS results demonstrate that the basaltic and alkalic units in the Bradbury group (sols 0-750) show minimal alteration indicating an arid climate. In contrast, the Murray formation of the Mount Sharp group (sols ~750-2301) has compositions indicating pervasive alteration. Diagenetic features are common and show fluid interaction with the sediment after (and possibly during) lithification, which is consistent with burial and diagenesis. A lithified sandstone unit, the Stimson formation, overlies part of the Murray formation. This has a composition similar to the basaltic sand and soil, suggesting a shared source. Cross-cutting, fracture-associated haloes are evidence of late-stage fluid alteration after lithification of the sediment. The APXS dataset, evaluated in concert with the full science payload of *Curiosity*, indicates that Gale crater was habitable, and that liquid water was stable for extended periods.

1. Introduction

The Alpha Particle X-ray Spectrometer (APXS) on the Mars rover *Curiosity* analyzed more than 700 targets during its first 2301 martian solar days since landing (sols; 1 sol = 24.6 h). The primary objectives of APXS investigations are to determine the elemental composition of geologic materials in Gale crater to infer the geologic and climate history, establish whether or not liquid water was stable for extended periods, constrain the geochemical conditions of ancient liquids, and deduce the provenance of sedimentary materials in the crater. APXS data are also key to interpreting results from the drilled and scooped samples that have been delivered to the Chemistry and Mineralogy (CheMin) X-ray diffractometer (Blake et al., 2012), and the Sample Analysis at Mars (SAM) mass spectrometer and gas chromatograph (Mahaffy et al., 2012).

In this work, we present an overview of APXS results from landing (sol 0) to the end of the Vera Rubin Ridge (VRR) campaign on sol 2301. These results encompass all APXS measurements acquired before *Curiosity* traversed into the unit named Glen Torridon (e.g., Fox et al., 2019). The results demonstrate that elemental trends in Gale crater record evidence of a changing climate, widespread interaction of liquid water with the rocks, and a basaltic and alkalic provenance. Here, we outline the broad compositional groups and common features that have emerged. The purpose of this work is to provide a context for more focused investigations so they can be better integrated for a deeper understanding of the geochemical history of Gale.

2. Geological Setting

Gale crater is a ~150 km wide complex impact crater with a central mound centered near the dichotomy boundary of the northern lowlands and southern highlands of Mars (5.4°S, 137.8°E). The Gale crater-forming impact occurred ~3.8 - 3.6 billion years ago (Ga; Thomson et al., 2011; Le Deit et al., 2013), and the crater floor was subsequently infilled with sediment likely

derived from mass wasting and fluvial erosion of the crater rim and central mound before 3.3 - 3.1 Ga (Grant et al., 2014; Grotzinger et al., 2015). The distal end of fan deposits sourced from the crater rim and nearby upland plains (Peace Vallis) reaches *Curiosity's* traverse near Bradbury Landing (Palucis et al., 2014). Exhumation of the crater floor deposits has exposed lithified sedimentary strata that were likely deposited in a lacustrine system (Grotzinger et al., 2014, 2015). Sandstone strata consistent with a dry aeolian system unconformably overlie the fluvio-lacustrine units (Banham et al., 2018). Surface exposure age dating indicates that one unit, the Sheepbed mudstone, has been at the surface for 78 ± 30 Ma (Farley et al., 2014). Localized alluvial deposits indicate aqueous activity on Aeolis Palus <2 Ga ago (Grant & Wilson, 2019).

Curiosity's traverse is effectively a cross-section of the layered sedimentary strata in Gale crater (Figure S1). The traverse began at Bradbury Landing, and the first detailed investigation was of outcropping sedimentary strata at Yellowknife Bay (YKB). From there, *Curiosity* traversed southwest across Aeolis Palus to an entry point onto lower Aeolis Mons (informally named Mt. Sharp), where the rover heading was changed on sol ~750 to drive south-southeast toward the central mound of Mt. Sharp. The rover has been ascending a succession of horizontal to sub-horizontal sedimentary units. The mean dip is roughly horizontal, thus elevation is an acceptable proxy for stratigraphic position (Grotzinger et al., 2015). Using elevation as a proxy where bedrock exposures and contacts are obscured, a composite stratigraphic column was assembled by (Grotzinger et al., 2015; Fedo et al., 2018; Stack et al., 2019; the MSL Science Team) from Bradbury Landing to the VRR (Figure 1). Note that the composite column represents a combination of two laterally separated columns, and the Bradbury group is hypothesized to be interfingered with the Mt. Sharp units (Grotzinger et al., 2015). The contacts for the stratigraphic

column are preliminary for units above approximately -4225 m elevation, and the unit names are informal.

3. Methods and Dataset

3.1. APXS Method

The APXS method combines particle-induced X-ray emission (PIXE) and X-ray fluorescence (XRF) techniques (Gellert et al., 2006, 2009; Campbell et al., 2012) to determine elemental concentrations in geologic samples. Curium-244 radioisotope sources emit radiation that induces characteristic X-rays from a specimen, a subset of which are in turn counted with a detector and converted into an energy dispersive spectrum. The relative areas of characteristic X-ray peaks correlate with the relative abundance of elements in the specimen, enabling the calculation of major, minor, and selected trace element concentrations for atomic number $Z \geq 11$ (Figure 2).

APXS data were reduced using a peak fitting routine with empirical concentration calculations derived from a laboratory calibration dataset, largely based on the one originally developed during the Mars Exploration Rover (MER) APXS calibration (Gellert et al., 2006), with adjustments specific to the MSL variant. The precision uncertainty (2σ) reported by the fit routine for each element decreases with improved counting statistics and resolution (VanBommel et al., 2019a, 2019b). However, errors reported here have supplemental corrections applied based on a set of empirically derived rules for each element to account for physical effects that can compound to degrade precision for certain elements more than others such as poor resolution or high standoff. Major, minor, and trace elements are reported in the form of sixteen oxides and elements normalized to 100 weight percent (wt%). Sulfur, chlorine, and iron are reported in weight percent

as SO_3, Cl, and FeO, noting that oxidation state is not measured by the APXS. Instrument accuracy and typical precision error are shown in Table 1 (Gellert & Clark, 2015).

3.2. Field Methods

Curiosity's APXS is an arm-mounted, robotically deployed field instrument that can analyze a variety of geologic materials under a range of environmental conditions (Figure S3). APXS targets include outcrop, veins, concretions, and unconsolidated materials. We differentiate unconsolidated materials as float, sand, soil, and dust. Float is arbitrarily defined here as loose fragments of rock on the surface that are much larger (>>2 mm) than grains in soils, sand, and dust (Weitz et al., 2018). Outcrop targets were typically given higher priority to systematically characterize the Gale rock units. However, float was analyzed regularly when outcrop was not reachable by the rover's arm (i.e., outside of the rover workspace) and/or to characterize the variety of materials encountered. Veins and concretions were surveyed and the different apparent types of features were analyzed and catalogued when possible. Veins and concretions in the APXS dataset are *not necessarily* representative of the frequency or distribution of the features over the traverse. For example, over most of the traverse, *Curiosity*'s tactical operations team attempted to exclude white veins from the APXS FOV because they were previously well characterized Ca-sulfate and complicate bedrock measurements of Ca and S.

Curiosity utilizes several different approaches for handling samples and placing the APXS in close (~mm to cm scale) proximity to surface samples with the rover's arm and there are consequences for data interpretation. Targets are measured by the APXS either as-is (i.e., undisturbed by rover hardware), after the surface was brushed by the Dust Removal Tool (DRT), after the target was disturbed by rover hardware (e.g., scratched by the rover's wheels), or as fines and fragments generated by the drill. Drill fines are measured by the APXS with multiple methods

(Table 2) involving the robotic arm and the sampling subsystem (SA/SPaH; Anderson et al., 2012). We refer to the different sample handling and deployment approaches as "preparation method", all of which are described in Table 2 with examples illustrated in Figure 3.

Context imagery and the inferred APXS FOV are used to determine what the APXS actually measured. Under optimal conditions, the rover arm placement accuracy is ~10 mm, precision is ~5 mm, and the APXS FOV is ~15-20 mm in diameter for measurements conducted within 5 mm of the target surface. The FOV increases with larger standoff distance (VanBommel et al., 2016, 2017). We estimate the APXS FOV footprint to be circular, with a signal intensity that is higher in the center of the FOV than at the margins, with a roughly gaussian cross-section of intensity across the diameter of the FOV. The standoff distance is estimated from the sum of all oxides (before normalization to 100 wt%), or the geometric norm, which indicates larger standoff distances when the sum is less than 100 wt% (Gellert et al., 2006), and this is converted to an average distance. To provide context imagery, APXS measurements are co-analyzed by the Mars Hand Lens Imager (MAHLI), which acquires microscopic images of the same targets (Edgett et al., 2012; Yingst et al., 2016). MAHLI images are usually acquired on the same sol before the APXS is deployed. Images of fine-grained particulates (e.g., sand or drill fines) are taken after the APXS is retracted to document if/when the APXS contact plate (Figure S3) touches the particulates. MAHLI data products are the highest resolution documentation of APXS targets, and nearly all APXS deployments include at least one MAHLI image with the optical axis aligned with the center of the APXS FOV at a working distance of ~5 cm. In this configuration, MAHLI captures an image area of approximately 5 cm by 3 cm. Acknowledging the arm placement accuracy and precision, we typically assume that the center of the 5 cm MAHLI image is the center of the APXS FOV. This is a valid assumption, but deviations occur in co-registration of APXS

and MAHLI as discussed by (VanBommel et al., 2016, 2017). MAHLI data products corresponding to APXS measurements share the same target name with APXS (Edgett et al., 2015). APXS targets are also documented in images by MastCam (Bell et al., 2012), the Navigation cameras (Navcams), and the Hazard Avoidance cameras (Hazcams; Maki et al., 2012). Raw image data is available on the Planetary Data System (PDS; https://pds-geosciences.wustl.edu/missions/msl/index.htm; Gellert, 2012). The Analyst's Notebook for MSL is a convenient source for browsing and compiling APXS data with corresponding imagery (e.g., Stein et al., 2019; https://an.rsl.wustl.edu/msl/mslbrowser).

3.3. Geochemical Dataset

Curiosity's APXS instrument has acquired >700 spectra on geologic materials along the rover's traverse up to sol 2301. Oxide and trace element concentrations for these targets are presented in Table 3. Statistical summaries of the groups discussed herein are presented in Table S1. Each target is part of a stratigraphic unit as defined by the MSL Science Team Sedimentology and Stratigraphy working group (Figure 1; e.g., Edgar et al., n.d.; Grotzinger et al., 2015). The stratigraphic unit names are convenient for grouping APXS targets by location along the traverse as well as in the composite stratigraphic column; however, the units are defined primarily by sedimentological and stratigraphic observations rather than chemical or mineralogical composition. Thus, some units contain more than one compositionally distinct rock type, and groups of different units have similar compositions. Soil and sand are classified as separate units and disconnected from the stratigraphic column.

The quality of APXS data is impacted by several factors that are constrained by rover operations: (1) the temperature of the APXS sensor head, (2) the length of the integration, and (3) the standoff distance from the target. Higher temperatures (>-20ºC) result in lower spectral

154 resolution, so the APXS conducts measurements when the ambient temperatures are low enough
155 for good data quality. For this reason, integrations are commanded during the morning (~09:00-
156 12:00) or evenings and overnight (~17:00-06:00). The spectral quality is approximated by the full-
157 width-at-half-maximum (FWHM) of the Fe Kα peak (Table 3). The signal/noise ratio increases
158 with longer integration times, which are given in Table 3 as the "lifetime" of the measurement.
159 The signal/noise ratio decreases with larger instrument standoff distance, and so the APXS is
160 deployed to within < 2 cm of the target, if possible, although topography of the target surface may
161 vary. The standoff distance, estimated from the APXS signal using the method of Gellert et al.
162 (2006), is given in Table 3. A detailed discussion of the effects of temperature, integration time,
163 and standoff distance on APXS data quality is presented by VanBommel et al. (2019b). Of the
164 measurements, 9 have very low-quality spectra (full width at half maximum at Fe K_α peak >250
165 eV) and we recommend conservative interpretation of those results (e.g., Figure S2).
166 In some cases, the APXS was moved by the arm to obtain multiple, generally overlapping,
167 measurements over an area and these are known as "rastered targets". Targets are rastered to
168 investigate heterogeneity on the mm-cm scale, particularly when multiple phases are apparent.
169 Common examples are white 5-10-mm-wide veins in bedrock and small concretions (VanBommel
170 et al., 2016, 2017). Multiple raster points on one target have the same name appended with
171 descriptors such as "_raster1, _raster2…_rasterN". Targets with two laterally adjacent APXS
172 integrations within ~2 cm or less are given the same name and appended with "_centre" and
173 "_offset".
174 *Curiosity*'s payload also contains a laser induced breakdown spectrometer (LIBS) on the
175 rover's mast that quantifies most major elements and some minor and trace elements (ChemCam;
176 Wiens et al., 2012, 2013). ChemCam targets typically consist of 3 – 5 LIBS spots in a line spaced

~1 – 10 mm apart (e.g., Mangold et al., 2015; Lasue et al., 2016; Nachon et al., 2017). The spot size of the LIBS shots increases from ~350 μm to ~550 μm in diameter with increasing distance of the instrument to the target (~1.6 – 7 m; Wiens et al., 2012). When ChemCam analyzes a target, it progressively ablates material with LIBS shots, and each spot typically has 30 shots. The depth is usually ~90 μm but can reach up to 1 mm in a consolidated rock target (Wiens et al., 2012). A spectrum (240-905 nm) of the plasma generated by the laser is acquired for each shot, enabling an analysis of surface dust (Lasue et al., 2018) as well as depth profiling (Lanza et al., 2016). In comparison, the APXS FOV is ~15 – 20 mm in diameter and the sampling depth varies as a function of the atomic number of the element being analyzed and the matrix composition. In a basalt matrix, for example, the sampling depth ranges from ~3 μm for Na to ~90 μm for Fe (Rieder et al., 2003; Brückner et al., 2008; Schmidt et al., 2018). The sample volume of the APXS is thus much larger than that of ChemCam. A consequence of this is that an APXS analysis of a fine-grained basalt, such as the APXS calibration target, approximates a bulk measurement (Campbell et al., 2014). In contrast, due to the smaller spot size, ChemCam requires 5-15 spots to converge on a bulk composition for a fine-grained rock (Anderson et al., 2011). The sampling differences between APXS and ChemCam lead to complexities in comparing the two datasets, and although valuable information can be derived by comparison, we do not do so herein.

4. Results

In this section we present an overview of APXS results for the first 2301 sols of *Curiosity*'s operations in Gale crater (Table 3). First, we summarize the APXS results for the high value drilled and scooped samples delivered to CheMin and SAM. Second, we present results from targets that are grouped broadly by elemental composition and stratigraphic units: (1) soil, sand, and dust (2)

lithified basaltic units, and (3) alkalic units. Then, we present selected results indicating element mobility: fracture-associated haloes and S, Cl, Br, and P characteristics. When discussing grouped targets, we state the median oxide or element concentrations and ± one standard deviation, as shown in Table S1, which presents statistical summaries of the target groups discussed herein.

4.1. Samples Delivered to CheMin and SAM

Drilled and scooped samples are the best-characterized that *Curiosity* obtains. They sample a larger volume of rock more likely to represent a rock's bulk composition, they have a relatively consistent grainsize after drilling, and they are delivered to the CheMin and SAM instruments inside the rover chassis. Drill samples were strategically planned to sample bedrock formations over intervals that best characterized the sedimentary units along the traverse (e.g., Rampe et al., 2020). The APXS was an important part of the sample triage process to find the most representative sample that the rover was able to drill.

Multiple APXS analyses are acquired at drill and scoop sites, and several different sample preparation methods are employed using the rover hardware (Table 2; Figure 3). This enables an evaluation of the degree of heterogeneity inside the drill hole and any elemental enrichments at the surface (top ~200 μm). Not all of the same sample preparation methods were used at every sampling site. The APXS campaigns at the 19 drill and 3 scoop sites varied depending on the science strategy and rover resources at the time of sampling. For different analyses of one site, APXS target names include the site name with appended descriptors (Table 3).

For every sampling site, we have determined which single APXS measurement is the best analogue for evaluating the sample splits ingested by CheMin and SAM (Tables 4 and 5). During a typical drill campaign, one or two analyses are conducted on the as-is and/or brushed surface, and then 2-4 analyses are obtained for the drilled fines. At most drill sites, APXS analyses of the

post-sieve fines (<150 μm grain size; abbreviated 'postsieve' in sample names) best represent the CheMin and SAM samples because the material followed the same sample collection, handling, and processing pathway as the material delivered to CheMin and SAM. However, a drill malfunction precluded the use of the sieves for samples after sol ~1500, and a method was developed (feed extended drilling; FED) by which the drill fines are delivered to CheMin and SAM directly from the drill bit assembly (DBA). For these samples, APXS analyses are conducted on fines dumped onto the ground from the DBA after the samples are delivered to CheMin and SAM. Because the fines are not sieved and homogenized in the sampling subsystem, the DBA fines that the APXS analyze may not represent exactly what the onboard instruments measure; compositional heterogeneities with depth or mechanical sorting due to material properties could be preserved in the DBA.

The most effective method for analyzing samples processed by SA/SPaH with the APXS is to dump the fines on the ground and deploy the APXS over the dump pile such that the FOV is filled and the thickness is 'infinite' with respect to the APXS sampling depth (approximately >200 μm). Post-sieve and DBA fines are a portion of the same material delivered to CheMin and SAM, therefore these APXS targets are the highest priority for drill sites. However, not every APXS analysis of a post-sieve dump pile was successful. In some cases, the pile was too thin and/or not centered in the APXS FOV due to movement of the sample by wind, uncertainty in the placement of the dump pile, or insufficient sample volume. Consequently, in some cases the drill tailings or pre-sieve fines are the best sample measured by APXS for particular drill holes. Based on assessments of the centered placement of the APXS and thickness of the dump piles, we have determined the best single drill fines targets for interpreting CheMin and SAM results (Tables 4 and 5). Results for these targets are presented in Table 3. Note that most of the post-sieve samples

collected before the change to feed extended drilling (after sol 2000) were dumped by SA/SPaH after being cached for a period during which the rover drove away from the sample site. The coordinates listed in Table 3 indicate the sampling location and *not* the dump location.

4.2. Soil, Sand, and Dust

Orbital, in situ, and meteoritic observations suggest that the average composition of the martian crust is basaltic (e.g, McSween et al., 2009), and this is reflected in the unconsolidated soil, sand, and dust in Gale crater. Nine soil targets and 39 sand targets were analyzed over the first 2301 sols of *Curiosity*'s traverse (Table 3, S2), and detailed results and interpretations have been presented previously (O'Connell-Cooper et al., 2017; O'Connell-Cooper et al., 2018). Airfall dust was measured on the rover's titanium observation tray on sols 177 and 571, as discussed by Berger et al. (2016). Soil is distinguished from sand primarily by two characteristics. First, soil has higher P_2O_5, SO_3, Cl, and Zn concentrations than sand. Second, aeolian processes are actively transporting the sand, whereas soil has a surface lag deposit and is more cohesive, indicating that it may be a less recently active deposit than sand, that is, soils are isolated, inactive bedforms (Sullivan et al., 2008; O'Connell-Cooper et al., 2017; Weitz et al., 2018).

The bulk chemical composition of the soil, sand, and dust is basaltic (Figure 4), with a volatile-free SiO_2 concentration of 46 ± 4 wt%, ($Na_2O + K_2O$) = 3.3 ± 1 wt%, FeO/MnO = 50 ± 8, and without systematic depletions or enrichments in other major or minor elements (Table 3, S2). The alkali content is higher than the SNC martian meteorites, (e.g, McSween et al., 2009), but approximately the same as the bulk polymict breccia martian meteorites (Agee et al., 2013). The sand targets have a wider range in major elements owing to aeolian sorting of mafic and felsic components: targets were selected intentionally to evaluate this effect (e.g., targeting ripple crests versus troughs; O'Connell-Cooper et al., 2017; O'Connell-Cooper et al., 2018).

Soil, sand, and dust are enriched in volatile elements S, Cl, and Zn, relative to bulk silicate Mars (Figure 5). Bulk Mars is likely enriched in volatile elements relative to the Earth (e.g., Dreibus & Wanke, 1985; Lodders & Fegley, 1997). However, the basaltic, unconsolidated soil, sand, and dust (as well as the lithified basaltic Gale crater sedimentary units) are all enriched in SO_3 (1-8 wt%), Cl (0.4-2 wt%), and Zn (130-940 ppm) compared to the ranges predicted for the crust and mantle (S ~110-1100 ppm; Cl ~25-390 ppm; Zn ~80 ppm; e.g., Lodders & Fegley, 1997; Taylor et al., 2010; Filiberto et al., 2019). Figure 5 shows SO_3, Cl, and Zn concentrations, as well as the consistent molar S/Cl ratio of 3.4 ± 0.2 in soils and dust. The same S/Cl ratio was found by the two MER rovers in basaltic soils (Yen et al., 2005). The molar S/Cl of sand (2.8 ± 0.2) is lower than soils and dust due to an apparent Cl enrichment and/or S depletion (O'Connell-Cooper et al., 2017). Sulfur, chlorine, and zinc are higher in soils than they are in sand (Figure 5). Sulfur and chlorine are yet higher in airfall dust than in soil and sand (Figure 5a). The MER APXS instruments found that Zn is enriched in surface dust relative to soil (Yen et al., 2005); this couldn't be confirmed with the MSL APXS because Zn was not detectable due to the thinness of the sample of airfall dust on top of the observation tray (Berger et al., 2016).

Phosphorus is positively correlated with S, Cl, and Zn in the in the sand and soil, but the sand has lower P_2O_5 (0.77 ± 0.09 wt%) than the soil (0.93 ± 0.05 wt%; Figure 6). Assuming the dust content is higher in the soil than in the sand, this is evidence of phosphorus enrichment in the dust. Phosphorus enrichment in airfall dust was also observed on the MER magnets (Goetz et al., 2005). The five sand outliers in Figure 6 with higher P_2O_5 (>0.90 wt%) at a given SO_3, Cl, and Zn are targets that had dust coatings on grains as well as larger average grain sizes (330-480 μm) than the sand with lower P_2O_5 (100-260 μm; Weitz et al., 2018). This is consistent with higher dust content, thin layer effects, and/or grain size effects.

The MER and MSL APXS observations show that the unconsolidated fine-grained materials on Mars are comprised of varying proportions of (1) regional sediment derived from basalt with a relatively uniform composition, (2) local materials (e.g., silica, sulfate, hematite, potassic rock), and (3) P-, S-, Cl-, and Zn-rich global dust (McSween & Keil, 2000; Bishop et al., 2002; McGlynn et al., 2011; Berger et al., 2016; O'Connell-Cooper et al., 2017). The dust is an important component because the similarity among the three landing sites is consistent with global mixing and a uniform dust unit, likely due to the recurring (1-3- martian years) global dust storms (Yen et al., 2005; Berger et al., 2016).

Based on the evidence summarized above, the basaltic soil has been hypothesized to represent the major and minor elemental composition of the average Mars crust by *Taylor & McLennan* (2010). This average crustal composition was compiled largely from MER APXS analyses of basaltic soils at Meridiani Planum and Gusev Crater renormalized after subtracting SO_3 and Cl (e.g., Yen et al., 2005; Gellert et al., 2006; Ming et al., 2008). Gale soils have a composition similar to basaltic soils analyzed by MER APXS (O'Connell-Cooper et al., 2017), as well as the airfall dust that settled on *Curiosity* (Berger et al., 2016). The overlapping basaltic soil and dust compositions and the constant S/Cl (3.7 ± 0.7) measured by APXS instruments at three rover landing sites (e.g., Franz et al., 2019) supports this conclusion. For this reason, here we define enrichment and depletion in Gale materials relative to Gale soil, which is reasonable as a representative composition of average martian surface materials. Here, we use the Sourdough soil measurement from sol 673 to represent average soils because it was the highest quality soil measurement.

313 **4.3. Rock Units**

314 **4.3.1. Lithified Basaltic Sedimentary Units**

315 Three lithified, layered sedimentary units have a volatile-rich, basaltic elemental
316 composition: (1) the Sheepbed member of the Yellowknife Bay (YKB) formation (McLennan et
317 al., 2013), (2) the Murray formation (Hurowitz et al., 2017; Rampe et al., 2017), and (3) the
318 Stimson formation of the Siccar Point group (Yen et al., 2017b; Banham et al., 2018). The
319 Sheepbed member and Stimson formation are both relatively similar to soil and sand; the Murray
320 formation, however, is distinct because it contains evidence of relatively uniform, open-system
321 alteration throughout the bedrock.

322 **4.3.1.1. Sheepbed Member**

323 The Sheepbed member is the stratigraphically lowermost unit investigated by *Curiosity* in
324 the Yellowknife Bay formation of the Bradbury group during sols ~130-290 (Figure 1). The area
325 explored (~800 m^2) is a small fraction of the ~4 km^2 extent of the Sheepbed member exposed at
326 the surface (Grotzinger et al., 2014). The very fine (< 50 μm) grain size and saponitic smectite
327 (~20%) content is consistent with a mudstone, which contains Ca-sulfate filled fractures and voids,
328 raised ridges, and nodules (Grotzinger et al., 2014; Vaniman et al., 2014).

329 Major and minor element concentrations in the Sheepbed member (Tables 3, S2) are
330 similar to soil (Figure 8e) and consistent with a basaltic composition (Figure 4). Plots of total alkali
331 versus silica (Figure 4) and Mg/Si versus Al/Si (Figure 7a) demonstrate the overlapping major
332 element compositions of the Sheepbed member with those of soil, sand, and dust. Minor and trace
333 elements differ from soil, having 40% higher Ni (700 ± 130 ppm), 160% higher Zn (800 ± 50
334 ppm), and 30% lower MnO (0.29 ± 0.04 wt%). The low MnO is reflected in a high FeO/MnO ratio
335 (70 ± 10), which is distinctive from the basaltic soils analyzed by the APXS on the MER and MSL

missions (~50 ± 5; O'Connell-Cooper et al., 2017). The Sheepbed member bedrock is also enriched in Ge (~85 ppm), whereas it is below the limit of detection (LOD) of ~30 ppm in the basaltic soils (Berger et al., 2017). Relative to concentrations predicted for the average basaltic crust, the Sheepbed member is enriched in volatile elements S, Cl, and Zn (Figure 5). Relative to soil, however, S/Cl is different, owing to the wider range of Cl contents (Figure 5b; see Section 4.4.3.).

4.3.1.2. Murray Formation

The greatest thickness of strata explored by *Curiosity* has been the Murray formation bedrock of the Mt. Sharp group (Figure 1), which comprises most of the traverse from sol ~750 to sol 2301 while climbing 320 m in elevation. The bedrock is primarily laminated mudstone. Some strata contain very fine sandstone mixed with siltstone and mudstone, and intermittent coarser sandstone lenses (e.g., Fedo et al., 2018; Stack et al., 2019). Diagenetic features are common and include cross-cutting white veins (see section 5.6) and concretions enriched in S, Fe, Mn, P, K, and Ni (e.g., VanBommel et al., 2016, 2017; Sun et al., 2019; Kronyak et al., 2019; Minitti et al., 2019).

The volatile-free composition of the Murray formation is basaltic and basaltic andesitic (Figure 4). However, Murray formation bedrock has notable differences from the other basaltic units. One distinction is a relative depletion in Mg and enrichment in Si, as evident in a plot of Mg/Si versus Al/Si (Figure 7b). For comparison, the basaltic and alkalic units define a mafic/felsic mixing line on this plot (Figure 7a), and the Murray formation deviates from this line. Note that there is a trend from low Mg/Si of the dust-free drill targets toward soil that is likely caused by mixing with Mg-rich airfall dust on unbrushed rock surfaces (Figure S10). Most of the Murray bedrock, when prominent Ca-sulfate veins (SO_3 >15 wt%) are omitted, is consistently low in Mn,

359 Mg, and Ca, and high in K, P, Ni, and Zn relative to soil (Figure 8b, 8c). The Murray units are thus
360 broadly distinguished chemically from average Mars by elevated SiO_2 (vein-free median is 48.0 ±
361 5.2 wt%) relative to soil (42.1 ± 0.5 wt%; Figure 4). The units are also uniformly enriched in Ge
362 (110 ± 25) by a factor of ~50 relative to martian meteorites and terrestrial basalts (Berger et al.,
363 2017).

364 The stratigraphically lowest Pahrump Hills member has similar element enrichments and
365 depletions compared to the overlying Murray formation units (Figure 8c). However, it is distinctive
366 from other Murray formation units (Figure 1) for its higher Al_2O_3 (10.4 ± 2.3 wt%) relative to the
367 overlying members (8.9 ± 0.76 wt%), resulting in a higher Al/Si for a given Mg/Si (Figure 7b).
368 For clarity in the geochemical plots and discussion presented herein, we refer to the Pahrump Hills
369 member as "lower Murray" (LM) and all of the Murray formation units above Pahrump Hills as
370 "upper Murray" (UM).

371 The Pahrump Hills member also contains unusual high-Si targets typified by the drill target
372 Buckskin (sols 1057-1091; Figure 8d). The Buckskin sample, which is within a high-Si unit in the
373 Pahrump Hills member, ranges to significantly higher SiO_2 (74 wt%) than the typical Murray
374 bedrock. This and ~8 other similar high-Si targets were limited to a < 5 m thick part of the unit.
375 Considering major and minor elements, the soil-normalized element pattern is broadly similar to
376 the other Murray formation units, except that some of the relative enrichments and depletions are
377 greater: Si and Ti are enriched, and Al, Fe, Mn, Mg, and Cr are depleted (Figure 8d). Key
378 differences are Ni and Zn, which are enriched in the Murray formation, are both depleted in
379 Buckskin. The SiO_2 enrichment and the associated depletion in MgO in Buckskin-like rocks leads
380 to lower Mg/Si, deviating from mafic/felsic mineral trends in Mg/Si and Al/Si associated with
381 igneous fractionation. Compared to the other Murray formation units, the high SiO_2 (73 ± 7 wt%)

382 Buckskin unit of Murray has even greater depletions in MnO and MgO, as well as lower FeO,
383 Al_2O_3, and Na_2O. The CheMin XRD results for Buckskin reveal that the total bulk Si is associated
384 primarily with tridymite (14 wt%) and the X-ray amorphous fraction (60 wt%; Morris et al., 2016).
385 Morris et al. (2016) conclude that the tridymite indicates silicic volcanism (ash or detrital), arguing
386 that low temperature formation (i.e., diagenetic) of this silica polymorph is kinetically inhibited.

387 **4.3.1.3. Stimson Formation**

388 Outcrop of the Stimson formation was encountered intermittently over sols 975 – 1350.
389 The Stimson formation bedrock of the Siccar Point group unconformably overlies the Murray
390 formation, and is comprised of coarse-grained, cross-bedded sandstone (Banham et al., 2018).
391 Crosscutting Ca-sulfate veins occur in the bedrock; however, they are less common in APXS
392 analyses than in the Sheepbed member and Murray formation. Fracture-associated haloes also
393 crosscut both the Murray and the Stimson formations (Yen et al., 2017b). The textures and
394 stratigraphy are consistent with formation via lithification of an aeolian sand (Banham et al., 2018).

395 Excluding fracture-associated haloes (Section 4.4.1) the Stimson formation shares similar
396 major element characteristics with soil, sand, and the Sheepbed member (Tables 3, S1). The
397 Stimson formation has a basaltic composition (Figure 4), and the plot of Mg/Si versus Al/Si
398 (Figure 7c) largely overlaps with soil on the inferred igneous mixing line. Several targets,
399 including the Big Sky drill tailings, have higher Al/Si in Figure 7c, which is attributed to higher
400 Al_2O_3 at approximately the same SiO_2. Volatile elements SO_3 and Cl have similar concentrations
401 and molar ratios as the Sheepbed member (Figure 5), which are enriched relative to the average
402 basaltic crust but not as narrowly constrained as soil and sand.

403 In the Stimson formation, trace elements and MnO are soil-like, which is unlike the
404 Sheepbed member and Murray formation. The Stimson formation has Ni (460 ± 70 ppm), Zn (315

± 150 ppm), MnO (0.39 ± 0.05 wt%), and FeO/MnO (50 ± 5) that are within the same range as soil. Exceptions are five targets with Zn >600 ppm, and these are located < 10m from contacts with the Murray formation, thus they may represent incorporation of Murray detritus into the Stimson bedrock and/or mobilization of Zn across the contact in diagenetic fluids (Berger et al., 2017). Germanium is below the limit of detection (LOD) of ~30 ppm in the Stimson formation, as it is in soil and sand (Berger et al., 2017).

4.3.2. Alkalic Sedimentary Units

The Bradbury group units overlying the Sheepbed member of the YKB formation are characterized by common alkalic sedimentary materials that are mixed with basaltic sedimentary materials. These rocks occur in a mix of sandstone and conglomerate strata and as unconsolidated regolith, or float (Figure 1; Figure 9; Grotzinger et al., 2014, 2015). The Windjana drill target (sols 612-704) in the Dillinger member of the Kimberley formation is the only drilled sample in the alkalic units of the Bradbury group (Treiman et al., 2016). Assessments of the distribution and APXS compositions of the alkalic Bradbury group targets were presented previously (Schmidt et al., 2014; Thompson et al., 2016). Herein, we denote results for the Sheepbed member of the Bradbury group with different symbols (gray triangles) than the rest of the Bradbury group (white diamonds) to distinguish the finer-grained, basaltic mudstone from the coarser-grained, alkalic units overlying it (Figure 1).

A limited number of alkalic rocks were found in the Mt. Sharp group as deposits of float (each roughly 0.01-0.03 km^2 in lateral extent) on top of the Murray formation These deposits have Bradbury-like, alkalic compositions that are distinct from the Murray bedrock (denoted BLF for "Bradbury-like float;" Figure 9). An unusual, small float deposit found on top of the Vera Rubin Ridge (VRR) at a waypoint named Bressay (17 targets over area of ~70 m^2, sols 2015-2022) also

428 has mugearitic and potassic rocks nearly identical in composition to those found in the Bradbury
429 group.

430 The alkalic rocks display two major element trends relative to the basaltic sedimentary
431 units (Table 3). One trend is toward high total alkali typified by the target JakeM (sol 46-47). The
432 JakeM rocks have high $Na_2O + K_2O$ (4-10 wt%; Figure 4) and Al_2O_3 (14-17 wt%) and low MgO
433 (< 5 wt%) and FeO (< 13 wt%). JakeM and similar rocks were classified as mugearitic based on
434 the bulk APXS composition (Stolper et al., 2013; Schmidt et al., 2014). The second trend is
435 potassic and is typified by the drill target Windjana in the Dillinger member of the Kimberley
436 formation. The potassic rocks have high K_2O (1.0-3.7 wt%), FeO (20-27 wt%), and MgO (9-13
437 wt%), but relatively low Na_2O (< 2.5 wt%). Windjana, the only alkalic sample drilled and analyzed
438 with CheMin XRD, is classified as a potassic basaltic sandstone (Treiman et al., 2016). CheMin
439 results indicate that all of the K_2O is in sanidine, which is ~20 wt% of the sample (Treiman et al.,
440 2016). The two major element trends are apparent in a total alkali versus silica diagram (Figure 4),
441 where the JakeM trend plots in the high-alkali basalt and alkalic fields with higher $Na_2O + K_2O$
442 and SiO_2, and the Windjana trend has lower SiO_2 and intermediate $Na_2O + K_2O$, plotting in the
443 alkali-basalt, tephrite/basanite, and foidite fields. The differences in Si, Al, and Mg are apparent
444 in Figure 7a, where the mugearitic trend has lower Mg/Si and higher Al/Si. For brevity, we refer
445 to the two trends as mugearitic and potassic; we acknowledge that this represents a range of
446 compositions for sedimentary rocks.

447 Minor and trace elements also delineate trends within the alkalic units. The mugearitic
448 rocks, distinguished from the other Bradbury group targets by higher Na_2O content, tend to have
449 lower MnO, Cr_2O_3, and Ni than soil and other basaltic to potassic basaltic materials (Figure 10).
450 Zinc in most of the mugearitic rocks (320 ± 270 ppm) is the same or lower than soil (310 ± 105

ppm). However, other rocks in the alkalic units have Zn enrichments that are commonly ~800 ppm and range up to 1900 ppm. The drilled Windjana target has a remarkable Zn enrichment of ~4500 ppm. The Zn-bearing phase was not identified by CheMin (Treiman et al., 2016) or SAM (Sutter et al., 2018). A possible veinlet, Stephen, located ~10 cm away from Windjana, has very high Zn (8160 ± 250 ppm), suggesting in situ Zn mobilization by fluids in the Kimberley formation (Berger et al., 2017). Germanium follows the same general trend as Zn, being enriched in the basaltic and potassic basaltic materials but not in the mugearitic rocks (Berger et al., 2017).

Ten targets grouped with the alkalic units deviate from the mafic/felsic mixing line defined by Mg/Si and Al/Si (Figure 7a). Et Then and Secure are float in the Bradbury group with high FeO (~27 wt%). Oscar and Ruker are Bradbury group targets with the high $Na_2O + K_2O$ (5-7 wt%) and low Ni (35-70 ppm) characteristic of mugearitic rocks, but relatively lower Al_2O_3 (9-11 wt%) results in lower molar Al/Si that differentiates the targets. Oscar, as well as the Bradbury-like float targets Little Devil, Sonneblom, and Zambezi, have FeO that is 15-50% higher than similar alkalic rocks on the mafic/felsic mixing line (Figure 7a). One target, Wildrose, is float located in the Bradbury group ~125 m from the Pahrump Hills member and is probably from that unit. Two targets found in the Bressay deposit (Askival raster and Sanquhar sols 2015-2022) have unusual SiO_2 enrichments up to 66 wt%.

4.4. Selected Mobile Element Trends

A number of features and trends highlight element mobility in the units investigated by *Curiosity* and are key to interpreting the history of Gale crater. In this section we present results and give an overview of the characteristics, occurrence, and distribution of the most prominent features and trends: (1) fracture-associated haloes, (2) sulfur, (3) chlorine and bromine, (4) and phosphorus.

4.4.1. Fracture-Associated Haloes

Fracture-associated haloes enriched in Si were discovered in Gale crater, and two that occur in the Stimson formation were investigated in detail with a drill campaign (Yen et al., 2017b). The halo targets trend toward the origin in a Mg/Si versus Al/Si plot in a similar manner to what is observed in the Murray formation bedrock because Mg and Al are lower, relative to Si (Figure 7b, 6c). Element gains and losses, relative to the less altered adjacent host bedrock, are well-characterized because two fractures were investigated by analyzing the halo and adjacent, less altered bedrock within ~1 m. Compared to the host Stimson bedrock, the haloes are enriched in Si, Ti, P, and S, and depleted in Al, Fe, Mn, Mg, Ni, Zn, and Cr (Figure 11). The element ratio pattern is notably similar to that of the Buckskin targets (Figure 8d). However, unlike Buckskin, the crystalline material in the two drilled halo samples, Greenhorn and Lubango, does not contain detectable tridymite (<1 wt%) and contains 20-25 wt% $CaSO_4 \cdot nH_2O$ minerals (Yen et al., 2017b). Note that crystalline material comprises only ~25-35 wt% of the halo samples and 50 wt% of the Buckskin sample (Morris et al., 2016; Yen et al., 2017b). The silica-rich haloes crosscut the Stimson formation as well as the Murray formation. Two adjacent (< 1 m apart) Murray bedrock targets, Cody and Ferdig (sols 1109-1110), show the same relative element trends, with the former being enriched in silica. Light-toned fracture haloes were also observed in Mastcam images of the Bradbury group (Gabriel et al., 2019); however, these were not investigated further with the APXS.

4.4.2. Sulfur

Sulfur is a major element (>1 wt%) in nearly all Gale crater materials (Table 3). Most targets (72%) thus far have SO_3 concentrations that fall into the same range found in sand, soil, and dust (2.3-8.3 wt%). Twenty-five percent of APXS targets have higher SO_3 concentrations (up to 44 wt%). Concentrations below 2 wt% were discovered in only four targets, including the

497 basaltic Stimson formation drill target Okoruso (SO_3 = 0.65 ± 0.03 wt%). Sulfur has clearly been
498 mobile in Gale, as evidenced by geochemical associations discovered in the Gale bedrock,
499 including associated diagenetic features (e.g., Kronyak et al., 2019; Sun et al., 2019).

500 The highest concentrations of S occur in white fracture- and void-filling material, which is
501 common, to varying degrees, in all of the Gale crater units (e.g., Nachon et al., 2014; Kronyak et
502 al., 2019; Sun et al., 2019). Not all rock types have white veins; for example, the mugearitic JakeM
503 class rocks (Schmidt et al., 2014; Thompson et al., 2016) do not have sulfate veins or nodules.
504 Nearly all of the 44 targets with SO_3 contents >15 wt% have positive correlation between SO_3 and
505 CaO at a ratio that approaches the weight ratio of CaO:SO_3 (Figure 12). An exception is the Garden
506 City vein complex (GC; sols 930-948), which is a mixture of white (Ca+S)-rich material and dark
507 Ca-rich material (VanBommel et al., 2017). White, cross-cutting and/or concordant veins were
508 visually confirmed in MAHLI and Mastcam images of 39 of the 44 high-S targets (SO_3 >15 wt%).
509 Five were ambiguous in the imagery, but we interpret the high (Ca + S) to be due to the same white
510 material (Table 3). Therefore, the white vein material in the APXS FOV is the source of the high
511 S concentrations for 90-100% of targets with SO_3 >15 wt%. Targets with intermediate SO_3 content
512 (~5-15 wt%) also typically have elevated CaO and thin (~1-2 mm) white veins in the APXS FOV.
513 The consistent CaO:SO_3 weight ratio (~3:2) in vein-bearing targets, and the confirmation of
514 crystalline Ca-sulfate phases (anhydrite, basanite, and gypsum) in CheMin XRD analyses (e.g.,
515 Vaniman et al., 2014; Bristow et al., 2018), provide strong evidence that the white, cross-cutting
516 and concordant veins observed by the APXS are Ca-sulfate. The mudstone-dominated units
517 (Sheepbed member, Murray formation) have the greatest density of veins, which is evident in the
518 distribution of CaO and SO_3 in the Gale stratigraphy (Figure S4). As stated above, the tactical
519 APXS operations group typically and intentionally avoids veins, and thus the actual distribution

of Ca-sulfate veins is not necessarily reflected accurately in the APXS dataset (e.g., Minitti et al., 2019). Notably, bedding-concordant veins are common in the Blunt's Point member and these were analyzed frequently by the APXS because they were difficult to resolve and identify in Navcam and Mastcam targeting images.

Note that figures 11b and 11d show an apparent systematic enrichment of SO_3 relative to CaO because most of the targets plot on the higher-SO_3 side of the CaO:SO_3 (1:1) line. Some of the SO_3 enrichment in targets with < ~30 wt% SO_3 is attributed to matrix effects arising from the necessary but incorrect assumption used in APXS analysis that the matrix is homogeneous on the sub-micrometer scale (Berger et al., 2020). The heterogeneous matrix effect is estimated to cause SO_3 concentrations to be ~5-30% high when the APXS FOV includes sulfate and silicate (Berger et al., 2020). However, the effect does not account for all of the excess sulfur with respect to Ca-sulfate, as evident in targets with S/Ca >1.3 (Figure 12d).

Sulfur is also associated elements other than Ca in localized features. Dendritic and sub-spherical concretions (~1 cm) in the Pahrump Hills and Hartmann's Valley members were analyzed with APXS rasters and show a positive correlation between MgO and SO_3 (Figure S5a; VanBommel et al., 2016, 2017). Deconvolution of the rasters using MAHLI image analysis indicates that the concretions are a mixture of the adjacent bedrock with ~10-15% pure $MgSO_4$ (VanBommel et al., 2017). Nickel is also highly enriched (up to 4000 ppm) in most, but not all of the concretions (Figure S5b). The concretions are interpreted to be Mg-sulfates that precipitated from diagenetic fluids in situ (VanBommel et al., 2017; Sun et al., 2019). The Mg-sulfate concretions are not as widespread as the Ca-sulfates; they are limited primarily to the Pahrump Hills member. One was measured in the Hartmann's Valley member (Pomona; sol 1191) and one was located on the Stimson formation within a few meters of the contact of the Hartmann's Valley

543 member with the Stimson formation (Sperrgebiet; sol 1277). Distinct from the Mg-sulfates, two
544 S-rich fracture-associated features found in the Murray formation occur with elevated K_2O and
545 FeO (Fresh Meadow and Thrumcap; sols 1504 and 1520). We reiterate that the APXS dataset does
546 not represent the true distribution of these features. For example, there were locations in the
547 vicinity of Pomona when there were extensive concretions, but they were outside the workspace
548 reachable by the rover's arm.

549 Sulfur is a component of the matrix of Gale bedrock (Figure 13a). Evidence in CheMin
550 XRD analyses indicates that the matrix of 9 of 12 Murray formation samples and the Stimson
551 formation fracture haloes contain >1 wt% crystalline Ca-sulfates (Vaniman et al., 2014; Rampe et
552 al., 2017; Yen et al., 2017b; Bristow et al., 2018). However, the coupling of S with Ca in sulfates
553 does not account for all of the sulfur in Gale bedrock. This is apparent in Figure 12, where targets
554 with elevated SO_3 do not necessarily trend toward the corresponding 1:1 molar S:Ca ratio expected
555 from simple addition of Ca-sulfate (Figure S6). Evidence of Mg-sulfates in Murray formation
556 nodules suggests that they could be present in the bedrock matrix; however, there is no direct
557 evidence of widespread Mg-sulfate in the bedrock matrix (Figure 13b). Deconvolving Ca-sulfate
558 from other possible S-bearing phase(s) is challenging with APXS alone, but the APXS analysis of
559 CheMin XRD samples enables the allocation of sulfur between crystalline and amorphous phases
560 (e.g., Morrison et al., 2018). Combined results from the APXS and CheMin show that ~50-90%
561 of the bulk S in bedrock samples is associated with the X-ray amorphous fraction in the bulk
562 sample (Table S2).

563 Some of the S X-ray signal in APXS analyses is attributed to airfall dust (Schmidt et al.,
564 2018), which contains 8.3 ± 0.4 wt% SO_3 (Berger et al., 2016). The effects of dust on APXS
565 analyses are discussed in detail by Schmidt et al. (2018), but the APXS analyses of drill fines

extracted from drill holes of 2-6 cm depth, in concert with CheMin and SAM results, confirm that sulfur is a major component of most Gale bedrock units, and S results are *not* simply a measurement of dust. For example, the vein-free bedrock of the Hartmann's Valley and Karasburg mbrs., which have relatively small variations in elemental compositions, do not have any apparent overall differences in SO_3 concentrations between unbrushed, brushed, and drill fines targets (Figure S7).

4.4.3. Chlorine and Bromine

Chlorine concentrations in Gale vary by an order of magnitude, ranging from 0.28 ± 0.01 wt% in the Buckskin drill fines up to 3.44 ± 0.09 wt% in an unusual, relatively erosion-resistant veinlet named Stephen (Figure 14a). Bromine also varies widely, with 44 targets below ~30 ppm and more than 15 targets with Br concentrations of 1000 to 2000 ppm (Figure 14b). The two elements are not well-correlated with each other, consistent with findings elsewhere on Mars (Haskin et al., 2005). For example, the diagenetic target Jones Marsh has the second-highest Cl in Gale (3.10 ± 0.09 wt%) but relatively low Br concentrations (155 ± 15 ppm). Despite lacking a clear correlation in absolute concentrations, Cl and Br are both consistently enriched in unbrushed and brushed surface targets compared to material exposed from depths of >1 mm by the drill (Figure 15). The Cl concentration in drilled material (0.56 ± 0.28 wt%) is about half of the Cl concentration in unbrushed surfaces (1.23 ± 0.51 wt%) and brushed surfaces (1.06 ± 0.54 wt%). The same difference in median Br concentrations is found between the surface (160 ppm) and the drilled material (70 ppm).

Elevated Cl at the surface (<1 mm depth) leads to the question: is the Cl analysis dominated by Cl-rich dust? Dust has a Cl concentration of 1.08 ± 0.12 wt% (Berger et al., 2016), which is within the range of the *median* unbrushed and brushed surface concentrations. However, the

589 distinctive S/Cl ratio of 3.4 ± 0.2 in dust (and soil) discussed above (section 5.1) is not consistent
590 with the surface targets. Excluding targets with S-rich veins and concretions, the median S/Cl of
591 surface targets is 2.2 ± 1.1 (Figure 15) because Cl is commonly higher at a given SO_3 concentration
592 than that found in dust and soil. We interpret this difference in S/Cl to be an indication that the
593 APXS analysis of Cl on the surface is not simply dust; Cl is enriched at the surface of most bedrock
594 relative to drilled material. Similar observations of elevated Cl on rock surfaces were made by the
595 MER APXS analyses of unbrushed, brushed, and abraded surfaces (Haskin et al., 2005).
596 Chlorine and bromine analyses do not show any systematic geochemical association with
597 any other single element in the Gale bedrock. For instance, considering only the 67 measurements
598 of bedrock drill fines, neither Cl nor Br have clear correlations ($-0.55 < r < 0.47$) with any of the
599 other 14 elements reported here. The same results hold for the unbrushed and brushed rock surfaces
600 ($-0.50 < r < 0.50$) when evaluated by the separate groupings discussed herein (Sheepbed, Bradbury,
601 LM, UM, Stimson). The upper Murray units have a very weak positive correlation between molar
602 Cl and Na ($r = 0.43$) that may indicate halite; Cl and K are not correlated ($r = 0.01$) thus KCl does
603 not control Cl concentrations if present (Figure 16). The lack of Cl and Br correlation with a single
604 cation in the bedrock indicates that chloride and oxychlorine species are associated with multiple
605 cations (e.g., Na, Mg, K, Ca). Mixed chloride and oxychlorine species are consistent with the
606 findings of the Phoenix and MSL missions. Analysis of the Phoenix Wet Chemistry Laboratory
607 experiments revealed evidence of perchlorate mixtures of ~60% $Ca(ClO_4)_2$ and ~40% $Mg(ClO_4)_2$
608 (Kounaves et al., 2014). Evolved gas analysis of Murray formation bedrock by SAM resulted in
609 O_2 peaks from oxychlorine phases that could be consistent with a mixture of $Ca(ClO_4)_2$,
610 $Mg(ClO_4)_2$, and $Mg(ClO_3)_2$ (Sutter et al., 2018). However, the upper Murray drilled samples do
611 not show chlorate/perchlorate detections in SAM analyses (Sutter et al., 2018). Akaganeite, a

612 possible Cl-bearing mineral [FeO(OH,Cl)], was also detected by CheMin in the Sheepbed
613 mudstone (1-2 wt%; Vaniman et al., 2014) and provisionally in the VRR sample Rock Hall (~7
614 wt%; Rampe, 2019).

615 Targets with the highest halide concentrations are localized features (i.e., veins, patchy
616 coatings/rinds) and have geochemical associations with multiple elements. In the Bradbury group,
617 the target Stephen, an approximately 10-cm-wide, linear ridge (likely a veinlet) adjacent to the
618 Windjana drill site, has the highest Cl concentration discovered by the APXS on Mars (3.36 ± 0.04
619 wt%). Stephen also has remarkable enrichments in MnO (4.05 ± 0.03) and Zn (8160 ± 250 ppm;
620 Thompson et al., 2016; VanBommel et al., 2016; Berger et al., 2017). Similarly, an APXS raster
621 of the Garden City vein cluster has evidence of an association between Cl, MnO, and Zn, all of
622 which are enriched (1.88 wt%, 1.01 wt% and 2438 ppm, respectively) in an uncommon, dark vein-
623 filling material by 3-4 times relative to the adjacent bedrock (Berger et al., 2017; VanBommel et
624 al., 2017). Jones Marsh (sol 1727), a patchy cm-scale darker-toned crust, is another example,
625 having very high Cl (3.1 wt%) and MnO (4.0 wt%). These diagenetic features indicate the mobility
626 of Cl in post-depositional fluids, which is key to understanding the aqueous history of Gale because
627 chloride is a conservative element in aqueous solutions (e.g., Garrels & Christ, 1965; Garrels &
628 MacKenzie, 1967). Additionally, halide species (e.g., perchlorate, chlorate and chloride) may act
629 as an oxidant and/or complexing ligand (e.g., Marion et al., 2010), and their presence at high
630 concentrations likely impacted geochemical processes on the martian surface.

631 **4.4.4. Phosphorus**

632 Systematic differences in P concentrations and evidence of P mobility have emerged along
633 *Curiosity*'s traverse. The Sheepbed member, Stimson formation (excluding the altered haloes), and
634 alkalic sedimentary units all have a relatively limited range of P_2O_5 concentrations (0.88 ± 0.22

635 wt%; Figure 17), and there is no correlation of P_2O_5 in these units with any of the other fifteen
636 elements reported here. The alkalic units of the Bradbury group have lower P_2O_5 (0.80 ± 0.16
637 wt%) than the Sheepbed member and Stimson formation (0.92 ± 0.09 wt%). Limited and/or
638 localized apatite enrichment in the alkalic units is suggested by the P_2O_5 enriched float targets
639 Nova (sol 687), Ruker (sol 387), and Waternish (sol 2022). Nova has high CaO and P_2O_5 (9.8 and
640 3.2 wt%, respectively), and Rucker and Waternish have elevated P_2O_5 (~1.5 wt%), and the targets
641 all have a CaO:P_2O_5 ratio of and is interpreted to be an apatite-rich igneous rock (Figure S8). The
642 Murray formation, in contrast, has greater P_2O_5 variance than the other sedimentary units (Figure
643 16). The Pahrump Hills member (LM) has slightly higher median P_2O_5 (1.25 ± 0.33 wt%) than the
644 upper Murray units (0.93 ± 0.52 wt%). Some of the Pahrump Hills rock targets with elevated SiO_2
645 (> 53 wt%) have higher P_2O_5 (1.5 – 2.5 wt%; Figure 18a).
646 Phosphorus enrichments occur in localized features in the Murray formation and in the
647 Stimson fracture haloes. Dark gray nodules and patches on bedrock (e.g., Timber Point, Maple
648 Spring, Berry Cove, and Jones Marsh) have correlated enrichments in MnO (0.8 – 4.0 wt%) and
649 P_2O_5 (3.0 – 7.5 wt%; Figure S9). Another occurrence of P enrichment is in the Garden City vein
650 complex, where the target Kern Peak, interpreted to be altered vein-hosting bedrock (Berger et al.,
651 2017), has elevated P_2O_5 (2.72 ± 0.14 wt%). The silica-rich fracture haloes in the Stimson
652 formation have elevated P_2O_5 (up to 2.51 wt%), which represents a 185% enrichment relative to
653 the less-altered adjacent bedrock (Figure 18b). Assuming TiO_2 has low mobility in diagenetic
654 fluids under most Eh-pH conditions (e.g., Young & Nesbitt, 1998), the increase of molar P/Ti from
655 1.1 ± 0.1 in the Stimson bedrock to ~1.6-1.9 in the altered haloes indicates an addition of P during
656 formation of the haloes.

5. Discussion

The APXS results demonstrate compositional diversity in Gale crater sedimentary bedrock and unconsolidated float, including elemental compositions that were not predicted to occur on Mars. Below, we discuss how the results are relevant to the primary objectives of the APXS investigation, which seeks to deduce the provenance of sedimentary materials in the crater, infer the paleoclimate, establish if liquid water was stable for extended periods, and constrain the geochemical conditions of ancient liquids. First, we compare compositions with igneous models to constrain the provenance of the materials in Gale crater. Then, we discuss the chemical evolution of the sedimentary units.

5.1. Comparison with Igneous Models to Constrain Provenance

5.1.1. Igneous Signatures of the Basaltic Units

Comparison of the APXS results with igneous geochemical models is useful for constraining the provenance of the sedimentary units in Gale crater, and for discerning secondary alteration and salt-forming processes. First, we consider the molar element ratio:

$$(0.25*Al+0.5*Fe+0.5*Mg+1.5*Ca+2.75*Na)/Ti$$

which models the fractionation via magmatic evolution and/or crystal sorting of a basaltic mineral assemblage containing olivine, plagioclase, and clinopyroxene (Stanley & Madeisky, 1996b). A positive correlation of this ratio (OL+CPX+PL)/Ti with molar Si/Ti and a slope of ~1 indicates igneous fractionation and/or sorting of mafic and felsic components of basalt (Figure 19a-c). Most cases of open system alteration cause points to deviate from the 1:1 line. The basalt geochemical indicator is thus sensitive to the addition of major elements via cement (e.g., silica, Fe-oxides) or salts (e.g., Mg-, Ca-sulfates) and removal of major elements via dissolution and leaching. A second

679 element ratio model is molar (Fe + Mg)/Al versus Si/Al (Figure 19d-f), which can indicate an
680 olivine control on element concentrations when targets plot with a 2:1 slope (Barnes et al., 2004).
681 Deviation from the 2:1 olivine control line indicates open-system alteration. Note that these
682 geochemical indicators are not sensitive to closed system (isochemical) alteration, and that
683 crystalline and amorphous alteration products can preserve the bulk chemical composition of the
684 parent material.

685 Compared to the basalt and olivine models, soil, sand, and the Sheepbed mudstone have a
686 relatively narrow range of elemental concentrations that are consistent with basaltic materials
687 (Figure 19a, d). The Stimson formation bedrock has the same range of compositions, with two
688 exceptions (Figure 19c, f). First, the fracture-associated haloes deviate from the basalt and olivine
689 models, reflecting the depletion of Al, Fe, Mn, and Mg relative to the less-altered bedrock (Figure
690 11; section 4.4.1). Second, several targets (Big Sky, Kwakwas, Nomeib) have 20-40% higher
691 Al_2O_3 than soil and other Stimson formation bedrock, resulting in a lower Si/Al, which may
692 indicate minor alteration. Overall, the Sheepbed member and Stimson formation share the
693 geochemical signatures of basalt. Therefore, the provenance of the two sedimentary units was very
694 likely basalt with a composition similar to the soil and sand.

695 The Murray formation deviates from the basalt and olivine chemical control models in
696 three ways (Figure 19b, e). First, the apparent depletion of Mg and Ca, and the enrichment in Si in
697 the large number of vein-free bedrock targets (n ~325; Figure 8b, c) results in lower molar
698 (OL+CPX+PL)/Ti and (Fe+Mg)/Al. Second, the Buckskin unit has very low (OL+CPX+PL)/Ti
699 and very high Si/Al. Third, localized diagenetic features with high Fe (e.g., Morancy Stream,
700 Newport Ledge, and Sagadahoc Bay) have corresponding high (OL+CPX+PL)/Ti, and the Ti-
701 depleted Haroldswick raster has high Si/Ti. The Murray formation observations support the

interpretation that the bedrock has a basaltic provenance, and that widespread open-system alteration occurred (Hurowitz et al., 2017; Rampe et al., 2017). The geochemical evidence and implications of this are addressed further in Section 5.2.

5.1.2. Igneous Signatures of the Alkalic Units

The variable compositions of the alkalic units (section 4.3.2.) suggest a diverse igneous provenance for the sedimentary materials in Gale crater. The basaltic and alkalic targets have a range of alkali contents that can be described by a mixing model with three endmembers: mugearitic, potassic, and basaltic. The three compositional endmembers correlate with the basalt control line (Figure 20a) and olivine control line (Figure 20b) discussed for the basaltic units above. The three endmembers are further illustrated in a plot of K/Ti versus Na/Ti, which can be sensitive to alkali feldspar fractionation and/or physical sorting (Figure 20c; e.g., Stanley & Madeisky, 1996a). In this plot, the higher total alkalis of the mugearitic rocks results in a positive correlation, whereas the potassic rocks trend to higher K/Ti and lower Na/Ti with a steep, negative slope. Many of the alkalic targets fall between the three assumed endmembers, likely representing intermediate mixtures of the three endmembers via physical sedimentary processes.

The basaltic and mugearitic endmembers have elemental compositional trends that are similar to ocean island volcanics, such as Tenerife (Canary Islands) and Mauna Kea (Hawai'i), where compositions follow the alkalic differentiation series basalt-hawaiite-mugearite-benmoreite (Figure 4; Schmidt et al., 2014; Stolper et al., 2013). The positive correlation of K/Ti with Na/Ti (Figure 20c) and the ~1:1 correlation of (Ca+Na)/Ti with Al/Ti (Figure 20d) is consistent with plagioclase enrichment in the mugearitic endmember (Stanley & Madeisky, 1996b). Post-shield volcanics on Mauna Kea exhibit very similar trends in the element ratio indicator plots discussed herein (Figure S12). The elemental characteristics of the basaltic and mugearitic endmembers may

be evidence of a common petrogenetic evolution, as seen in terrestrial post-shield volcanics (e.g., Wolfe et al., 1997).

Constraints on the potassic endmember are provided by the drill target Windjana, which has evidence of a magma source separate from the basaltic and mugearitic endmembers. Windjana is not a singular igneous composition; the presence of pigeonite and sanidine together indicates at least two sources because a sanidine-rich protolith would contain augite and not pigeonite (Treiman et al., 2016). Windjana has mineralogical evidence of three sediment sources, which correspond with the three igneous endmembers evident in the APXS results: basalt, a plagioclase-rich source, and potassic trachyte (Treiman et al., 2016). Based primarily on CheMin XRD results, Treiman et al. (2016) concluded that the potassic component of Windjana (sanidine) was sediment derived from a potassic trachyte lava, although potassic metasomatism could not be ruled out.

We suggest that igneous processes and simple physical mixing can convincingly create most of the alkalic compositions found in the Bradbury group. It is thus not necessary to call upon generation of these compositions using physical sorting of sediment derived from a basalt protolith alone (cf. Siebach et al., 2017). On Earth, physical sorting of basaltic sediment does not necessarily result in significant chemical fractionation. For example, the Dyngjusandur basaltic glacial outwash sand sheet in Iceland has only a small increase in olivine content (apparent in the 8% relative increase in MgO) with fluvial and aeolian transport over a distance of 30 km (Sara, 2017). Similarly, an enrichment in olivine was found at the Lambahraun sandy–lava plain in Iceland over a distance of ~12 km of aeolian transport, but the major elements vary by less than 9% (Mangold et al., 2011). For comparison, the Sheepbed member is ~30-60 km from the Peace Valles catchment that may have been a source region. Indeed, the active sands in Gale have been transported more than ~10 kilometers with relatively limited sorting and minimal changes to the

748 original basaltic bulk composition (O'Connell-Cooper et al., 2017; O'Connell-Cooper et al.,
749 2018).

750 An important consideration for an igneous endmember model is the elevated
751 concentrations of volatile elements SO_3 (1-8 wt%) and Cl (0.5-1.9 wt%), which are confirmed by
752 drill fines results to be a component of the bedrock to a depth of ~5 cm and are not simply a thin
753 dust coating. The source of S and Cl is uncertain: were they added by aqueous processes after
754 deposition or incorporated as a detrital or airfall dust component? We can say with certainty that
755 they were both mobile in fluids after deposition because Ca-sulfate veins crosscut nearly every
756 unit. Furthermore, the Stephen target, which is an apparent veinlet adjacent to the Windjana
757 potassic basaltic drilled sandstone, is highly enriched in Cl (3.5 wt%). Therefore, the igneous
758 chemical signatures were likely modified, at a minimum, by addition of S and Cl.

759 **5.2. Chemical Evolution of the Sedimentary Units**

760 Considering the evidence presented above, we can reasonably conclude that the
761 sedimentary units of Gale crater contain the geochemical signatures of a basaltic provenance, with
762 mugearitic and potassic sources contributing to most of the Bradbury group and to the Bradbury-
763 like float on lower Mt. Sharp. Chemical evidence of alteration was found throughout the strata,
764 and localized enrichments in veins, concretions, and other features demonstrate in situ
765 mobilization and concentration of elements. Results from CheMin XRD confirm profoundly that,
766 while the bedrock has a petrogenesis that is related to igneous processes based on the presence of
767 the detrital basaltic mineral assemblage of plagioclase and pyroxene with some olivine, oxides,
768 and apatite, other processes are also recorded by the occurrence of typical alteration minerals:
769 silica polymorphs, X-ray amorphous materials, phyllosilicates, Ca-sulfates, jarosite, akaganeite,
770 and iron oxides (Rampe et al., 2020). Most authors have thus explained the chemistry of Gale

771 crater in terms of volcanic genesis followed by sedimentary processes that include mineral sorting,
772 weathering, and diagenesis (e.g., Siebach et al., 2017; Hurowitz et al., 2017; Frydenvang et al.,
773 2017; Bedford et al., 2019). Below we discuss the chemical evolution of the sedimentary units in
774 Gale crater and the implications for its geologic history.

775 **5.2.1. Sedimentological and Stratigraphic Background**

776 Sedimentological and stratigraphic observations have led to the interpretation that Gale
777 crater contained fluvial, deltaic, and lacustrine environments (Grotzinger et al., 2014, 2015).
778 *Curiosity*'s traverse through the sequence of eroded sedimentary rocks (Figure 1) has revealed
779 evidence that the lowermost unit, the Sheepbed mudstone of Yellowknife Bay (YKB), was a
780 subaqueous lacustrine deposit (Grotzinger et al., 2014, 2015). The Sheepbed mudstone underlies
781 the conglomerate and massive, cross-stratified, and clinoform sandstone of the Bradbury group,
782 which was likely deposited in a fluvial environment (Grotzinger et al., 2014, 2015). The Murray
783 formation of the Mount Sharp group is the next sedimentary unit and is proposed to be linked to
784 the Sheepbed mudstone by a similar lacustrine depositional setting (Grotzinger et al., 2015). The
785 Murray formation is primarily laminated mudstone, but thin sandstone units occur (Fedo et al.,
786 2018). Much of the lithologic variability is found in the Sutton Island member, which is a mix of
787 mudstone, siltstone, and sandstone. Depositional transitions and changes in lacustrine
788 environments (i.e., perennial to episodic) are suggested by the mixed rock types. This is supported
789 by possible desiccation features in the Sutton Island member (Stein et al., 2018). The
790 sedimentological relationship(s) between the Pettegrove Point and Jura members comprising the
791 VRR and other Murray formation units is(are) under investigation (e.g., O'Connell-Cooper et al.,
792 2019; Thompson, 2019). The Stimson formation of the Siccar Point group unconformably overlies

793 the Murray formation, and is interpreted to be lithified sand dune deposits that imply a change in
794 climate from wet to arid (Banham et al., 2018).

795 **5.2.2. Mudstones of the Mt. Sharp and Bradbury Groups**

796 The mudstones of the Sheepbed member and Murray formation are comprised primarily of
797 fine-grained rock that may be genetically linked by a lacustrine depositional environment and share
798 a similar basaltic provenance (although the provenance of the Murray formation is less certain).
799 The chemical evolution of the two units, however, was distinct, as reflected in compositional
800 differences.

801 **5.2.2.1. Sheepbed Member**

802 The similarity of the Sheepbed member to basaltic soil (Figure 8e) suggests that (1) the
803 sediment source was basaltic and (2) the alteration evident in CheMin analyses was largely
804 isochemical (McLennan et al., 2013; Vaniman et al., 2014). McLennan et al. (2013) interpreted
805 the conditions under which the Sheepbed member formed to be cold, arid, and rock dominated,
806 which indicates rapid erosion and deposition. CheMin XRD results led Vaniman et al. (2014) to
807 hypothesize that ~75% less olivine, three times more magnetite, and the ~20 wt% smectite in two
808 Sheepbed member samples, relative to the nearby Rocknest soil sample (Blake et al., 2013), was
809 evidence that basaltic detrital material with a soil-like composition was altered such that most of
810 the olivine was converted to magnetite and smectite. The isochemical nature of this alteration
811 process suggests it was authigenic (McLennan et al., 2013; Vaniman et al., 2014). A minor amount
812 of open system processes may be evident in the depleted Mn, which may have been dissolved in
813 fluid and removed from the rock.

814 The model outlined above for the formation of the Sheepbed mudstone does not account
815 for Zn, which is more than two times higher than soil, and the remarkable Ge enrichment (80 ± 25

816 ppm). High concentrations of moderately volatile trace elements invoke enrichment processes
817 (e.g., hydrothermal; see Section 5.2.6) that are at odds with the hypothesis that basaltic sediment
818 was isochemically altered at low temperatures. The trace element signature therefore suggests a
819 more complex history.

820 **5.2.2.2. Murray Formation**

821 Evidence of aqueous processes are apparent in the Murray formation bedrock composition
822 as well as the common diagenetic features. The Murray formation and Sheepbed member
823 mudstones likely have similar basaltic provenance and are hypothesized to represent a common
824 lacustrine depositional setting, with the overlying Murray formation representing younger deposits
825 (e.g., Hurowitz et al., 2017). The two mudstones, however, have distinct compositions. In this
826 section, we explore two models of the aqueous geochemical conditions under which the Murray
827 formation could have been altered. In general, we assume that the temperatures were below ~75
828 °C, which is the maximum temperature modeled for buried Gale sediment, assuming no external
829 heat source (Borlina et al., 2015) at the likely maximum burial depth of ~2600 m (Lewis et al.,
830 2019). The timing of fluid interactions in the Murray formation are partially constrained by K-Ar
831 dating of the drilled sample Mojave 2 (sols 867-888) by the SAM instrument, which determined a
832 bulk age of 2.57 ± 0.39 Ga (Martin et al., 2017). Detrital feldspar formed at 4.07 ± 0.63 Ga, and
833 the observed low temperature K-Ar release indicates that jarosite in the sample crystallized 2.12 ±
834 0.36 Ga, providing evidence that low pH aqueous processes occurred ~1 Ga after deposition
835 (Martin et al., 2017), which likely occurred before 3.3 - 3.1 Ga (Grant et al., 2014; Grotzinger et
836 al., 2015). Below, we discuss the APXS results in the context of two contrasting models for the
837 chemical evolution of the Murray formation: acid sulfate alteration and circumneutral chemical
838 weathering.

839 ***Acid sulfate alteration***

840 In the Murray formation, element enrichments and depletions relative to soil (Figure 8b, c)
841 are similar to those of the altered Stimson fracture haloes (Figure 11). This leads us to consider if
842 the acid sulfate alteration interpretation for the haloes (Yen et al., 2017b) can also account for
843 variations observed in the Murray formation bedrock. The presence of jarosite in Murray samples
844 (Rampe et al., 2017) is also a strong indicator of low pH fluids because it precipitates at pH <5
845 (King & McSween, 2005), and commonly coprecipitates with phyllosilicates and hematite in
846 acidic sedimentary systems (e.g., Baldridge et al., 2009). The geochemical and mineralogical
847 evidence led Rampe et al. (2017) to propose a model for the Pahrump Hills member (Lower
848 Murray) in which acidic groundwater interacted with the sediment and mobilized Al, Fe, Mn, Ni,
849 and Zn. In this model, the Buckskin unit was leached of these elements (Figure 8d), and they were
850 translocated down-section and precipitated due to buffering by weathering reactions to higher pH,
851 causing Al, Zn, and Ni enrichment in the underlying Pahrump Hills bedrock.

852 The acidic alteration model for the Pahrump Hills member can be extended to all of the
853 ~320 m of overlying Murray formation strata. The element ratio pattern (Figure 8c) shows that,
854 relative to the basaltic soil, Murray formation bedrock has elevated SiO_2, the same or greater TiO_2,
855 FeO, K_2O, and P_2O_5, and depleted MnO, MgO, and CaO. These chemical trends are similar to
856 terrestrial rocks altered by acid sulfate processes. For example, Morris et al. (2000) showed that
857 acid-sulfate altered tephra from Mauna Kea, Hawai'i retains SiO_2 and TiO_2 in the altered rock
858 residue. Iron is oxidized and forms secondary Fe-oxides that can be retained in the altered tephra.
859 Sodium and potassium are leached from the rock and precipitate with alunite group sulfates (e.g.,
860 jarosite), and phosphate derived from apatite dissolution is retained in the secondary alteration
861 assemblage. Elements removed from the rock are Mn, Mg, and Ca. The result is a bulk composition

862 with same or greater TiO_2, FeO, K_2O, and P_2O_5, and depleted MnO, MgO, and CaO, which is the
863 same trend observed in the Murray formation bedrock. Elements that were mobilized and removed
864 from the bulk rock are accounted for in the closed Gale crater basin by the Mg- and Ca-sulfates in
865 veins and concretions, and in highly localized Mn-rich features (Berger et al., 2019).
866 Several characteristics are problematic for the acid sulfate alteration model. Minor amounts
867 of fluorapatite (1-2 wt%) co-exist with jarosite (0-3 wt%; Rampe et al., 2017), but fluorapatite is
868 soluble at low pH (Chaïrat et al., 2007) and so would be expected to dissolve. This may be evidence
869 that only minor, localized jarosite formed by oxidation of sulfides (Hurowitz et al., 2017).
870 Furthermore, it is difficult to maintain extensive amounts of strongly acidic solutions in the
871 presence of the other observed minerals because acid-base reactions will neutralize the solution
872 (King & McSween, 2005).

873 ***Chemical weathering and SiO_2 enrichment in neutral to alkaline fluids***

874 Chemical weathering and silica addition via precipitation from neutral to alkaline fluids
875 has been proposed to explain the Murray characteristics, particularly the elevated SiO_2 (Figure 8;
876 Frydenvang et al., 2017; Hurowitz et al., 2017). If circumneutral (i.e., pH between ~6 and 8)
877 chemical weathering occurred at Gale crater before, during, and after transport of the lake
878 sediment, it is likely that the fluids which interacted with the sediment contained dissolved silica
879 (Hurowitz et al., 2017). Since Gale crater is a closed basin and has probably remained as such over
880 its history (Malin & Edgett, 2000), mass balance requires addition of the dissolved components to
881 the sediment after the lake and groundwater evaporated. The addition of a silica cement (e.g.,
882 Siever, 1957) would result in higher SiO_2 in the bulk rock. This model requires that the silica-
883 depleted, weathered residue was not re-incorporated into the sediment, because that would result
884 in ~zero net change in the bulk composition. According to Hurowitz et al. (2017), the SiO_2

885 enrichment in the Pahrump Hills member, typified by the drill target Buckskin, can be explained
886 by the simple addition of pure SiO_2 and $CaSO_4$ to a bedrock composition representative of average
887 bedrock for that unit (Telegraph Peak drill sample).

888 A simple silica addition model is inconsistent with APXS observations. Hurowitz et al.
889 (2017) predicts that the composition of the high-SiO_2 Buckskin unit is modeled by a mixture of
890 three endmembers: pure SiO_2, $CaSO_4$, and Pahrump Hills bedrock (represented by the Telegraph
891 Peak target). We tested this model to determine how accurately it predicts the Buckskin
892 composition. A linear, least squares deconvolution was used to estimate the fractions of each of
893 the three endmembers proposed for the Buckskin sample (see supplementary text S1). According
894 to the deconvolution, pure SiO_2, $CaSO_4$, and Telegraph Peak comprise 55%, 8%, and 32% of the
895 Buckskin sample, respectively. This result is comparable to Hurowitz et al. (2017), who estimated
896 Telegraph Peak was ~30% of Buckskin. However, when the three endmember components are
897 combined to model the Buckskin sample, significant differences are apparent (Figure 21a). Most
898 notable are TiO_2, K_2O, and P_2O_5, which are respectively ~3X, ~2X, and ~2X higher in the actual
899 Buckskin sample than in the model. A fingerprint of acid sulfate alteration, as discussed above in
900 terrestrial samples (Morris et al., 2000), is the retention of these three elements in the altered
901 residue and secondary phases. These characteristics should therefore should not be dismissed in
902 interpretations of the Murray formation chemical evolution. In summary, the silica + $CaSO_4$
903 addition model may be oversimplified; the geochemical characteristics of the bedrock are, overall,
904 not consistent with the model.

905 The circumneutral weathering model may also be inconsistent with K_2O and Na_2O
906 observations. If the protolith was chemically weathered by a circumneutral fluid that released silica
907 into solution, then we would expect concomitant mobilization of the more-soluble ions K^+ and Na^+

908 (Nesbitt & Wilson, 1992). Both K^+ and Na^+ are conservative elements and would likely accumulate
909 in a brine and precipitate in evaporitic deposits, not in a cement with silica (Garrels & Christ,
910 1965). This prediction is not consistent with the K_2O enrichment and soil-like Na_2O concentrations
911 in the Murray formation bedrock (Figure 8 b, 8c, 8d).

912 Chemical weathering of basalt in a circumneutral, open system can be quantified with the
913 chemical index of alteration (CIA; Nesbitt & Young, 1982). The CIA is calculated using molecular
914 proportions:

915 $$CIA = [Al_2O_3 / Al_2O_3 + CaO + Na_2O + K_2O] \times 100.$$

916 Higher CIA values, relative to the unaltered protolith, indicate chemical weathering because Al
917 usually has low solubility at circumneutral pH and is retained in weathered residue, whereas Ca,
918 Na, and K are more soluble and are more likely to be removed from the system via weathering
919 (Nesbitt & Young, 1982). We find that the CIA is not a useful alteration index for APXS results
920 in Gale crater for the following reasons:

921 1. The CIA does not consider Mg, which has been demonstrated as a sensitive indicator of
922 chemical weathering on Mars (Figure 7; e.g., Ming et al., 2006) in part because olivine is
923 likely the most susceptible mineral to incipient low temperature alteration in martian
924 sediments (Vaniman et al., 2014; Yen et al., 2017b), which is consistent with terrestrial
925 samples (e.g., Nesbitt & Wilson, 1992).
926 2. The CIA is only applicable if the secondary salts can be subtracted from the chemical
927 analysis, which is problematic for Gale crater targets because Ca-sulfate is ubiquitous
928 (section 4.4.2). The amount of Ca-sulfate is poorly constrained in samples that have not
929 been analyzed by CheMin and therefore Ca-sulfate cannot be subtracted from most samples
930 without an unacceptable amount of uncertainty.

3. Much of the S in the bulk sample is likely associated with the amorphous component (Table S2; McAdam et al., 2014; Morrison et al., 2018). In this amorphous material, S is likely coupled with Mg and/or Fe in amorphous sulfates. Thus, the amount of sulfate salts cannot be unambiguously subtracted from APXS analyses because S is coupled with Ca, Mg, and Fe, all of which are major elements associated with primary igneous phases.
4. Evidence of Al mobility is found in the Pahrump Hill member (Rampe et al., 2017) and in the Stimson formation fracture haloes (Yen et al., 2017b). If Al is mobile, then it is not suitable to use as the immobile element against which to compare Ca, K, and Na mobility in the CIA.

5.2.3. Bradbury Group Sandstone, Conglomerate, and Float

The geochemical characteristics of the Bradbury group (excluding the Sheepbed member mudstone) are generally consistent with a mixture of unaltered and/or isochemically altered igneous endmembers. The physical mixing model proposed in Section 5.1.2 reasonably accounts for most of the sandstone, conglomerate, and float compositions by way of mixtures of the basaltic, mugearitic, and potassic basaltic endmembers. This is consistent with the results from the only drill target in Bradbury units above the Sheepbed member, Windjana, which is a mixture of igneous components that were likely cemented by magnetite and ferrihydrite (Treiman et al., 2016). Iron-rich cement is also apparent in several Bradbury targets with higher FeO that deviates from igneous mixing models (e.g., Oscar, Et Then; Figure 7a; Schmidt et al., 2014). The APXS observations suggest that the Bradbury materials were transported, deposited, and lithified under conditions with limited chemical weathering.

An important consideration is the veinlet Stephen next to the drill target Windjana. Stephen is highly enriched in Zn, Mn, and Cl (Sections 4.3.2, 4.4.3), which is strong evidence of in situ

mobilization of those elements, likely after lithification. The timing of the formation of Stephen is not well constrained because the fin-shaped feature protrudes from the bedrock and does not preserve clear cross-cutting relationships. In addition, aqueous activity was possible >1 Gy after the bulk of the sediments were deposited because localized Aeolis Palus alluvial deposits dated at <2 Ga could have introduced fluids into the system (Grant & Wilson, 2019). Nevertheless, Stephen demonstrates aqueous activity in the Bradbury group sandstone that concentrated fluid-mobile elements.

5.2.4. Stimson Formation Sandstone

The Stimson formation bedrock has a composition consistent with basaltic soil and sand that has experienced limited, largely isochemical alteration of basaltic material (section 4.3.4.3). Olivine is below the 1-2 wt% detection limit of CheMin in the Big Sky and Okoruso drill targets, and the 10-11 wt% magnetite in the samples, which probably comprises the cementing agent, could be secondary diagenetic products of olivine alteration (Yen et al., 2017b). The sedimentological interpretation of the Stimson formation is that it formed in an arid aeolian system, and stratigraphic relationships suggest the unconformity between the underlying Murray formation and the Stimson formation represent a period of erosion and time (Banham et al., 2018). The geochemical differences between the two formations also indicate distinct geochemical evolution of the bedrock. However, features indicating similar aqueous activity are common to both formations: (1) cross-cutting sulfate veins, (2) cross-cutting fracture-associated haloes, and (3) Mg-sulfate nodules near the unconformity (e.g., Sperrgebiet). Therefore, the chemical evolution of the two formations is not entirely decoupled.

975 **5.2.5. Fracture Halo Formation**

976 Fracture-associated haloes (Section 4.4.1) cross-cut the Murray formation, Stimson
977 formation (Yen et al., 2017b), and the Bradbury group (Gabriel et al., 2019), postdating the
978 lithification of those units. Ca-sulfate veins, which also cross-cut sedimentary bedding, delineate
979 sharp boundaries between unaltered and altered rock, indicating that the sulfate veins formed
980 before the haloes, therefore the haloes likely represent the youngest geochemical alteration
981 event(s) discovered by *Curiosity* (Yen et al., 2017b).

982 Two of the models proposed for the fracture haloes have contrasting hypotheses on the pH
983 of the fluids that interacted with the rock. The chemical and mineralogical characteristics of the
984 fracture haloes led Yen et al. (2017b) to conclude that initially acidic fluids leached Al, Fe, Mn,
985 Mg, Ni, Zn, ±Na, and ±K, causing the passive enrichment of silica and TiO_2 in the residue. The
986 depletion of Al is notable because it typically has low solubility in circumneutral fluids and
987 remains in altered residue; mobility of Al is an indicator for low pH. Excess Si, relative to Ti,
988 indicates later alkaline fluids deposited additional silica, thus silica enrichment was both passive
989 and active. Frydenvang et al. (2017) proposed a model involving only active enrichment of silica:
990 groundwater interacted with the underlying Si-rich Buckskin unit and carried dissolved silica to
991 the fractures where it was precipitated via decrease in temperature and/or alkalinity. The model
992 suggests that the haloes are parent bedrock diluted with Ca-sulfate and pure silica. This three
993 endmember model is the same as proposed for the Murray formation (Hurowitz et al., 2017), and
994 we tested it with the same linear, least-squares deconvolution discussed in Section 5.2.2.2 (see also
995 supplementary text S1). The model results have a significant mismatch of the modeled versus
996 measured concentrations of Ti, Na, K, P and ±Cr (Figure 21b, 21c). The silica + $CaSO_4$ addition
997 model deviates from the observed composition in the same manner for both the fracture haloes and

998 the Murray formation (Figure 21a). We conclude that it is not a compelling model for the formation
999 of the fracture haloes.

1000 **5.2.6. Hydrothermal Indicators**

1001 In the Murray formation, the trace elements Zn and Ge are enriched (1060 ± 460 ppm and
1002 110 ± 20 ppm, respectively) tens to hundreds of times greater than predicted from martian
1003 meteorites and crustal formation models (Berger et al., 2017). Because the two elements are
1004 commonly coupled in hydrothermal fluids, their enrichment indicates a hydrothermal signature in
1005 the Murray formation. The Murray units do not contain hydrothermal mineral assemblages
1006 expected with a basaltic protolith (e.g., serpentine–chlorite–(amphibole–talc– magnetite) ± garnet
1007 ± quartz) (Schwenzer & Kring, 2009). However, the Murray formation does contain assemblages
1008 of minerals associated with hydrothermal processes: hematite, magnetite, Si-rich X-ray amorphous
1009 material, phyllosilicates, and, most importantly because it is the only unambiguous high
1010 temperature phase, tridymite (Morris et al., 2016; Bristow et al., 2018). These observations led
1011 Berger et al. (2017) to conclude that hydrothermal deposits exist(ed) in the Gale source region and
1012 were dispersed with siliciclastic material during transport and deposition. Alternatively, the
1013 localized occurrence of high-temperature silica mineralization (~870 °C; e.g., Swamy et al., 1994)
1014 has led to speculation that hydrothermal fluids interacted with the Murray formation bedrock after
1015 deposition (Yen et al., 2017a). The presence of a possible hydrothermal deposit is a key finding
1016 because it expands the number of habitable environments that could have existed in Gale.

1017 Enriched Zn and Ge also occur at concentrations similar to the Murray formation in the
1018 Sheepbed member and alkalic units (with the exception of the mugearitic endmembers), suggesting
1019 that this trace element signature is common in Gale (Berger et al., 2017). In these units, like the

Murray formation, hydrothermal alteration mineral assemblages expected for a basaltic protolith were not unambiguously identified.

6. Conclusions

Curiosity's APXS has acquired a dataset of >700 measurements over a >20 km traverse, determining the elemental composition of geologic materials on the martian surface. The APXS has made a number of other contributions, including sample triage for drill site selection, providing constraints on crystal chemistry for CheMin (e.g., Morrison et al., 2018) and sulfur and chlorine speciation for SAM (e.g., Sutter et al., 2018), and enabling K-Ar dating with SAM results (Farley et al., 2014; Martin et al., 2017). The APXS has also made it possible to directly compare the elemental composition of martian surface materials at the Viking, Pathfinder, MER-A, and MER-B landing sites, building on a global compositional dataset.

How does the geochemical data from the APXS contribute to an integrated model of the provenance and chemical evolution of Gale crater? APXS-based observations from Gale crater have led to a number of conclusions, including:

1. Unconsolidated fine material, or sand, soil, and dust, has a basaltic composition that is effectively the same as basaltic soil found at the MER and Pathfinder sites. This establishes an average basaltic composition for the martian crust.

2. The Bradbury group has a wide range of compositions, indicating the source region is a diverse igneous complex containing basalts, mugearites, and potassic basalts.

3. The preserved igneous bulk elemental compositions of the Bradbury group sandstone, conglomerate, and float indicate deposition in an arid climate and rapid erosion, with minimal open-system chemical weathering.

4. The Sheepbed member mudstone and Murray formation mudstone both have evidence of a basaltic provenance; however, their geochemical characteristics are different. The Sheepbed member largely preserves the bulk chemical composition of basalt, indicating limited, closed-system alteration. In contrast, the Murray formation has indications of pervasive open-system alteration in the bedrock. If the Sheepbed member mudstone and Murray formation mudstone are linked by a similar lacustrine depositional paleoenvironment, their chemical evolution pathways were distinct.

5. The Stimson formation is an aeolian sandstone with a basaltic composition similar to sand and soil. The basaltic composition is largely preserved, indicating deposition in an arid environment and limited, closed-system alteration during lithification.

6. Diverse diagenetic features are common on *Curiosity's* traverse, and include nodules, veins, concretions, and patchy crusts with enrichments in Mn, Fe, Zn, Ni, P, Cl, and S. These enrichments indicate widespread element mobility in fluids.

7. Ca-sulfate veins crosscut every unit, demonstrating fluid activity after lithification of the sediment.

8. Extensive open-system alteration occurred in localized, fracture-associated haloes, thus fluid activity occurred after lithification of the Murray formation and unconformably overlying Stimson formation, and after formation of the cross-cutting Ca-sulfate veins.

ACKNOWLEDGEMENTS

All APXS spectra and reductions are available at the planetary data system, https://pds-geosciences.wustl.edu/msl/msl-m-apxs-4_5-rdr-v1/mslapx_1xxx/. We are indebted to NASA-JPL, the Canadian Space Agency, and Australian Research Council (DP150104604) for supporting our work and the MSL mission. A portion of this work was conducted at the Jet Propulsion Laboratory, California Institute of Technology under a contract with the National Aeronautics and Space Administration.

REFERENCES

Agee, C. B., Wilson, N. V., McCubbin, F. M., Ziegler, K., Polyak, V. J., Sharp, Z. D., et al. (2013). Unique Meteorite from Early Amazonian Mars: Water-Rich Basaltic Breccia Northwest Africa 7034. *Science*. https://doi.org/10.1126/science.1228858

Anderson, R. B., Morris, R. V., Clegg, S. M., Bell III, J. F., Wiens, R. C., Humphries, S. D., et al. (2011). The influence of multivariate analysis methods and target grain size on the accuracy of remote quantitative chemical analysis of rocks using laser induced breakdown spectroscopy. *Icarus*, *215*(2), 608–627. https://doi.org/10.1016/j.icarus.2011.07.034

Anderson, R. C., Jandura, L., Okon, A. B., Sunshine, D., Roumeliotis, C., Beegle, L. W., et al. (2012). Collecting Samples in Gale Crater, Mars; an Overview of the Mars Science Laboratory Sample Acquisition, Sample Processing and Handling System. *Space Science Reviews*, *170*(1–4), 57–75. https://doi.org/10.1007/s11214-012-9898-9

Baldridge, A. M., Hook, S. J., Crowley, J. K., Marion, G. M., Kargel, J. S., Michalski, J. L., et al. (2009). Contemporaneous deposition of phyllosilicates and sulfates: Using Australian acidic saline lake deposits to describe geochemical variability on Mars. *Geophysical Research Letters*, *36*(19). https://doi.org/10.1029/2009GL040069

Banham, S. G., Gupta, S., Rubin, D. M., Watkins, J. A., Sumner, D. Y., Edgett, K. S., et al. (2018). Ancient Martian aeolian processes and palaeomorphology reconstructed from the Stimson formation on the lower slope of Aeolis Mons, Gale crater, Mars. *Sedimentology*, *65*(4), 993–1042. https://doi.org/10.1111/sed.12469

Barnes, S. J., Hill, R. E. T., Perring, C. S., & Dowling, S. E. (2004). Lithogeochemical exploration for komatiite-associated Ni-sulfide deposits: strategies and limitations. *Mineralogy and Petrology*, *82*(3), 259–293. https://doi.org/10.1007/s00710-004-0051-7

Bedford, C. C., Bridges, J. C., Schwenzer, S. P., Wiens, R. C., Rampe, E. B., Frydenvang, J., & Gasda, P. J. (2019). Alteration trends and geochemical source region characteristics preserved in the fluviolacustrine sedimentary record of Gale crater, Mars. *Geochimica et Cosmochimica Acta*, *246*, 234–266. https://doi.org/10.1016/j.gca.2018.11.031

Bell, J. F., Malin, M. C., Caplinger, M. A., Ravine, M. A., Godber, A. S., Jungers, M. C., et al. (2012). Mastcam Multispectral Imaging on the Mars Science Laboratory Rover: Wavelength Coverage and Imaging Strategies at the Gale Crater Field Site. In *Lunar Planet. Sci. Conf, XLIII* (p. Abstract 2541).

Bell, J. F., Godber, A., McNair, S., Caplinger, M. A., Maki, J. N., Lemmon, M. T., et al. (2017). The Mars Science Laboratory Curiosity rover Mastcam instruments: Preflight and in-flight calibration, validation, and data archiving. *Earth and Space Science*, *4*(7), 396–452. https://doi.org/10.1002/2016EA000219

Berger, J. A., Schmidt, M. E., Gellert, R., Campbell, J. L., King, P. L., Flemming, R. L., et al. (2016). A global Mars dust composition refined by the Alpha-Particle X-ray Spectrometer in Gale Crater. *Geophysical Research Letters*, *43*(1), 67–75. https://doi.org/10.1002/2015GL066675

Berger, J. A., Schmidt, M. E., Gellert, R., Boyd, N. I., Desouza, E. D., Flemming, R. L., et al. (2017). Zinc and germanium in the sedimentary rocks of Gale Crater on Mars indicate hydrothermal enrichment followed by diagenetic fractionation. *Journal of Geophysical Research: Planets*, *122*(8), 1747–1772. https://doi.org/10.1002/2017JE005290

Berger, J. A., King, P. L., Gellert, R., Clark, B. C., O'Connell-Cooper, C. D., Thompson, L. M., et al. (2019). Manganese Enrichment Pathways Relevant to Gale Crater, Mars: Evaporative Concentration and Chlorine-Induced Precipitation. In *Lunar and Planetary Science Conference* (Vol. 50, p. 2487).

Berger, J. A., Schmidt, M. E., Campbell, J. L., Flannigan, E. L., Gellert, R., Ming, W., & Morris, R. V. (2020). Particle Induced X-ray Emission spectrometry (PIXE) of Hawaiian volcanics: An analogue study to evaluate the APXS field analysis of geologic materials on Mars. *Icarus*, 113708. https://doi.org/10.1016/j.icarus.2020.113708

Bishop, J. L., Murchie, S. L., Pieters, C. M., & Zent, A. P. (2002). A model for formation of dust, soil, and rock coatings on Mars: Physical and chemical processes on the Martian surface. *J. Geophys. Res.*, *107*(5097), 17. https://doi.org/doi:10.1029/2001JE001581

Blake, D., Vaniman, D., Achilles, C., Anderson, R., Bish, D., Bristow, T., et al. (2012). Characterization and Calibration of the CheMin Mineralogical Instrument on Mars Science Laboratory. *Space Science Reviews*, *170*(1–4), 341–399. https://doi.org/10.1007/s11214-012-9905-1

Blake, D. F., Morris, R. V., Kocurek, G., Morrison, S. M., Downs, R. T., Bish, D., et al. (2013). Curiosity at Gale Crater, Mars: Characterization and Analysis of the Rocknest Sand Shadow. *Science*, *341*(6153), 1239505. https://doi.org/10.1126/science.1239505

Borlina, C. S., Ehlmann, B. L., & Kite, E. S. (2015). Modeling the thermal and physical evolution of Mount Sharp's sedimentary rocks, Gale Crater, Mars: Implications for diagenesis on the MSL Curiosity rover traverse. *Journal of Geophysical Research: Planets*, *120*(8), 2015JE004799. https://doi.org/10.1002/2015JE004799

Bristow, T. F., Rampe, E. B., Achilles, C. N., Blake, D. F., Chipera, S. J., Craig, P., et al. (2018). Clay mineral diversity and abundance in sedimentary rocks of Gale crater, Mars. *Science Advances*, *4*(6), eaar3330. https://doi.org/10.1126/sciadv.aar3330

Brückner, J., Dreibus, G., Gellert, R., Squyres, S. W., Wänke, H., Yen, A., & Zipfel, J. (2008). Mars Exploration Rovers: chemical composition by the APXS. In J. F. Bell III (Ed.), *The Martian Surface* (Vol. 1, pp. 58–101). New York: Cambridge University Press.

Campbell, J. L., Perrett, G. M., Gellert, R., Andrushenko, S. M., Boyd, N. I., Maxwell, J. A., et al. (2012). Calibration of the Mars Science Laboratory Alpha Particle X-ray Spectrometer. *Space Science Reviews*, *170*(1–4), 319–340. https://doi.org/10.1007/s11214-012-9873-5

Campbell, J. L., King, P. L., Burkemper, L., Berger, J. A., Gellert, R., Boyd, N. I., et al. (2014). The Mars Science Laboratory APXS calibration target: Comparison of Martian measurements with the terrestrial calibration. *Nucl. Instrum. Methods Phys. Res. B*, *323*, 49–58. https://doi.org/10.1016/j.nimb.2014.01.011

Chaïrat, C., Schott, J., Oelkers, E. H., Lartigue, J.-E., & Harouiya, N. (2007). Kinetics and mechanism of natural fluorapatite dissolution at 25°C and pH from 3 to 12. *Geochimica et Cosmochimica Acta*, *71*(24), 5901–5912. https://doi.org/10.1016/j.gca.2007.08.031

Dreibus, G., & Wanke, H. (1985). Mars, a volatile-rich planet. *Meteoritics*, *20*, 367–381.

Edgar, L. A., Fedo Christopher M., Gupta Sanjeev, Banham Steven, Fraeman Abigail A., Grotzinger John P., et al. (n.d.). A lacustrine paleoenvironment recorded at Vera Rubin ridge, Gale crater: Overview of the sedimentology and stratigraphy observed by the Mars Science Laboratory Curiosity rover. *Earth and Space Science Open Archive*. https://doi.org/10.1002/essoar.10501350.1

Edgett, K. S., Yingst, R. A., Ravine, M. A., Caplinger, M. A., Maki, J. N., Ghaemi, F. T., et al. (2012). Curiosity's Mars Hand Lens Imager (MAHLI) Investigation. *Space Science Reviews*, *170*(1–4), 259–317. https://doi.org/10.1007/s11214-012-9910-4

Edgett, K. S., Yingst, R. A., & McBride, M. J. (2015). *Curiosity's Mars Hand Lens Imager (MAHLI) Mars Science Laboratory Principal Investigator's Notebook: Sols 90–179*. MSL MAHLI Technical Report 0003, Version. Retrieved from http://www.researchgate.net/profile/Ken_Edgett/publication/279179730_Curiositys_Mars_Hand_Lens_Imager_(MAHLI)_Mars_Science_Laboratory_(MSL)_Principal_Investigators_Notebook_Sols_90179/links/558c524508aee43bf6ae2b0e.pdf

Farley, K. A., Malespin, C., Mahaffy, P., Grotzinger, J. P., Vasconcelos, P. M., Milliken, R. E., et al. (2014). In Situ Radiometric and Exposure Age Dating of the Martian Surface. *Science*, *343*(6169), 1247166. https://doi.org/10.1126/science.1247166

Fedo, C. M., Grotzinger, J. P., Gupta, S., Fraeman, A., Edgar, L., Edgett, K., et al. (2018). Sedimentology and stratigraphy of the Murray formation, Gale crater, Mars. In *49 th Lunar and Planetary Science Conference, Abstract* (Vol. 2078).

Filiberto, J., McCubbin, F. M., & Taylor, G. J. (2019). Chapter 2 - Volatiles in Martian Magmas and the Interior: Inputs of Volatiles Into the Crust and Atmosphere. In J. Filiberto & S. P. Schwenzer (Eds.), *Volatiles in the Martian Crust* (pp. 13–33). Elsevier. https://doi.org/10.1016/B978-0-12-804191-8.00002-7

Fox, V. K., Bennett, K. A., Bristow, T., Ehlmann, B. L., House, C., Fairén, A. G., et al. (2019). Exploring the Clay-Bearing Unit with the Curiosity Rover, *50*, 2826.

Franz, H. B., King, P. L., & Gaillard, F. (2019). Chapter 6 - Sulfur on Mars from the Atmosphere to the Core. In J. Filiberto & S. P. Schwenzer (Eds.), *Volatiles in the Martian Crust* (pp. 119–183). Elsevier. https://doi.org/10.1016/B978-0-12-804191-8.00006-4

Frydenvang, J., Gasda, P. J., Hurowitz, J. A., Grotzinger, J. P., Wiens, R. C., Newsom, H. E., et al. (2017). Diagenetic silica enrichment and late-stage groundwater activity in Gale crater, Mars. *Geophysical Research Letters*, *44*(10), 2017GL073323. https://doi.org/10.1002/2017GL073323

Gabriel, T. S. J., Hardgrove, C., Achilles, C., Rampe, E. B., Czarnecki, S., Rapin, W., et al. (2019). Pervasive water-rich, fracture-associated alteration halos in Gale crater, Mars. In *AGU Fall Meeting Abstracts* (Vol. 43). Retrieved from http://adsabs.harvard.edu/abs/2019AGUFM.P43B..08G

1189 Garrels, R. M., & Christ, C. L. (1965). Minerals, solutions, and equilibria. *Minerals, Solutions,*
1190 *and Equilibria*.

1191 Garrels, R. M., & MacKenzie, F. T. (1967). Origin of the Chemical Compositions of Some
1192 Springs and Lakes. In *Equilibrium Concepts in Natural Water Systems* (Vol. 67, pp. 222–
1193 242). AMERICAN CHEMICAL SOCIETY. https://doi.org/10.1021/ba-1967-0067.ch010

1194 Gellert, R., & Clark, B. C. (2015). Compositional measurements of rocks and soils on NASA's
1195 Mars rovers with the alpha-particle X-ray spectrometer (APXS). *Elements*, *11*, 39–44.

1196 Gellert, R. (2012) Mars Science Laboratory Alpha Particle X-Ray Spectrometer EDR Data V1.0,
1197 MSL-M-APXS-2-EDR-V1.0, NASA Planetary Data System.

1198 Gellert, R., Rieder, R., Brückner, J., Clark, B. C., Dreibus, G., Klingelhöfer, G., et al. (2006).
1199 Alpha Particle X-Ray Spectrometer (APXS): Results from Gusev crater and calibration
1200 report. *Journal of Geophysical Research*, *111*(E02S05).
1201 https://doi.org/200610.1029/2005JE002555

1202 Gellert, R., Campbell, J. L., King, P. L., Leshin, L. A., Lugmair, G. W., Spray, J. G., et al.
1203 (2009). The Alpha-Particle-X-Ray-Spectrometer (APXS) for the Mars Science
1204 Laboratory (MSL) Rover Mission. In *Lunar Planet. Sci., XL* (p. Abstract 2364).

1205 Goetz, W., Bertelsen, P., Binau, C. S., Gunnlaugsson, H. P., Hviid, S. F., Kinch, K. M., et al.
1206 (2005). Indication of drier periods on Mars from the chemistry and mineralogy of
1207 atmospheric dust. *Nature*, *436*(7047), 62–65. https://doi.org/10.1038/nature03807

1208 Grant, J. A., & Wilson, S. A. (2019). Evidence for Late Alluvial Activity in Gale Crater, Mars.
1209 *Geophysical Research Letters*, *46*(13), 7287–7294.
1210 https://doi.org/10.1029/2019GL083444

1211 Grant, J. A., Wilson, S. A., Mangold, N., Calef, F., & Grotzinger, J. P. (2014). The timing of
1212 alluvial activity in Gale crater, Mars. *Geophysical Research Letters*, *41*(4), 1142–1149.
1213 https://doi.org/10.1002/2013GL058909

1214 Grotzinger, J. P., Sumner, D. Y., Kah, L. C., Stack, K., Gupta, S., Edgar, L., et al. (2014). A
1215 Habitable Fluvio-Lacustrine Environment at Yellowknife Bay, Gale Crater, Mars.
1216 *Science*, *343*(6169), 1242777. https://doi.org/10.1126/science.1242777

1217 Grotzinger, J. P., Gupta, S., Malin, M. C., Rubin, D. M., Schieber, J., Siebach, K., et al. (2015).
1218 Deposition, exhumation, and paleoclimate of an ancient lake deposit, Gale crater, Mars.
1219 *Science*, *350*(6257), aac7575. https://doi.org/10.1126/science.aac7575

1220 Haskin, L. A., Wang, A., Jolliff, B. L., McSween, H. Y., Clark, B. C., Des Marais, D. J., et al.
1221 (2005). Water alteration of rocks and soils on Mars at the Spirit rover site in Gusev crater.
1222 *Nature*, *436*(7047), 66–69. https://doi.org/10.1038/nature03640

1223 Hurowitz, J. A., Grotzinger, J. P., Fischer, W. W., McLennan, S. M., Milliken, R. E., Stein, N., et
1224 al. (2017). Redox stratification of an ancient lake in Gale crater, Mars. *Science*,
1225 *356*(6341), eaah6849. https://doi.org/10.1126/science.aah6849

1226 King, P. L., & McSween, H. Y. (2005). Effects of H2O, pH, and oxidation state on the stability
1227 of Fe minerals on Mars. *Journal of Geophysical Research*, *110*, 15 PP.
1228 https://doi.org/200510.1029/2005JE002482

Kounaves, S. P., Chaniotakis, N. A., Chevrier, V. F., Carrier, B. L., Folds, K. E., Hansen, V. M., et al. (2014). Identification of the perchlorate parent salts at the Phoenix Mars landing site and possible implications. *Icarus*, *232*, 226–231. https://doi.org/10.1016/j.icarus.2014.01.016

Kronyak, R. E., Kah, L. C., Edgett, K. S., VanBommel, S. J., Thompson, L. M., Wiens, R. C., et al. (2019). Mineral-Filled Fractures as Indicators of Multigenerational Fluid Flow in the Pahrump Hills Member of the Murray Formation, Gale Crater, Mars. *Earth and Space Science*, *6*(2), 238–265. https://doi.org/10.1029/2018EA000482

Lanza, N. L., Wiens, R. C., Arvidson, R. E., Clark, B. C., Fischer, W. W., Gellert, R., et al. (2016). Oxidation of manganese in an ancient aquifer, Kimberley formation, Gale crater, Mars. *Geophysical Research Letters*, 2016GL069109. https://doi.org/10.1002/2016GL069109

Lasue, J., Clegg, S. M., Forni, O., Cousin, A., Wiens, R. C., Lanza, N., et al. (2016). Observation of> 5 wt% zinc at the Kimberley outcrop, Gale crater, Mars. *Journal of Geophysical Research: Planets*. https://doi.org/10.1002/2015JE004946

Lasue, J., Cousin, A., Meslin, P.-Y., Mangold, N., Wiens, R. C., Berger, G., et al. (2018). Martian Eolian Dust Probed by ChemCam. *Geophysical Research Letters*, *45*(20), 10,968-10,977. https://doi.org/10.1029/2018GL079210

Le Deit, L. L., Hauber, E., Fueten, F., Pondrelli, M., Rossi, A. P., & Jaumann, R. (2013). Sequence of infilling events in Gale Crater, Mars: Results from morphology, stratigraphy, and mineralogy. *Journal of Geophysical Research: Planets*, *118*(12), 2012JE004322. https://doi.org/10.1002/2012JE004322

Lewis, K. W., Peters, S., Gonter, K., Morrison, S., Schmerr, N., Vasavada, A. R., & Gabriel, T. (2019). A surface gravity traverse on Mars indicates low bedrock density at Gale crater. *Science*, *363*(6426), 535–537. https://doi.org/10.1126/science.aat0738

Lodders, K., & Fegley, B. (1997). An Oxygen Isotope Model for the Composition of Mars. *Icarus*, *126*(2), 373–394. https://doi.org/10.1006/icar.1996.5653

Mahaffy, P., Webster, C., Cabane, M., Conrad, P., Coll, P., Atreya, S., et al. (2012). The Sample Analysis at Mars Investigation and Instrument Suite. *Space Science Reviews*, *170*(1–4), 401–478. https://doi.org/10.1007/s11214-012-9879-z

Maitre, R. W. L., Streckeisen, A., Zanettin, B., Bas, M. J. L., Bonin, B., & Bateman, P. (2002). *Igneous Rocks: A Classification and Glossary of Terms: Recommendations of the International Union of Geological Sciences Subcommission on the Systematics of Igneous Rocks*. Cambridge University Press.

Maki, J., Thiessen, D., Pourangi, A., Kobzeff, P., Litwin, T., Scherr, L., et al. (2012). The Mars Science Laboratory Engineering Cameras. *Space Science Reviews*, *170*(1–4), 77–93. https://doi.org/10.1007/s11214-012-9882-4

Malin, M. C., & Edgett, K. S. (2000). Sedimentary Rocks of Early Mars. *Science*, *290*(5498), 1927–1937. https://doi.org/10.1126/science.290.5498.1927

Mangold, N., Baratoux, D., Arnalds, O., Bardintzeff, J.-M., Platevoet, B., Grégoire, M., & Pinet, P. (2011). Segregation of olivine grains in volcanic sands in Iceland and implications for

Mars. *Earth and Planetary Science Letters*, *310*(3), 233–243. https://doi.org/10.1016/j.epsl.2011.07.025

Mangold, N., Forni, O., Dromart, G., Stack, K., Wiens, R. C., Gasnault, O., et al. (2015). Chemical variations in Yellowknife Bay formation sedimentary rocks analyzed by ChemCam on board the Curiosity rover on Mars. *Journal of Geophysical Research: Planets*, *120*(3), 2014JE004681. https://doi.org/10.1002/2014JE004681

Marion, G. M., Catling, D. C., Zahnle, K. J., & Claire, M. W. (2010). Modeling aqueous perchlorate chemistries with applications to Mars. *Icarus*, *207*(2), 675–685. https://doi.org/10.1016/j.icarus.2009.12.003

Martin, P. E., Farley, K. A., Baker, M. B., Malespin, C. A., Schwenzer, S. P., Cohen, B. A., et al. (2017). A Two-Step K-Ar Experiment on Mars: Dating the Diagenetic Formation of Jarosite from Amazonian Groundwaters. *Journal of Geophysical Research: Planets*, *122*(12), 2803–2818. https://doi.org/10.1002/2017JE005445

McAdam, A. C., Franz, H. B., Sutter, B., Archer, P. D., Freissinet, C., Eigenbrode, J. L., et al. (2014). Sulfur-bearing phases detected by evolved gas analysis of the Rocknest aeolian deposit, Gale Crater, Mars. *Journal of Geophysical Research: Planets*, *119*(2), 373–393. https://doi.org/10.1002/2013JE004518

McGlynn, I. O., Fedo, C. M., & McSween, H. Y. (2011). Origin of basaltic soils at Gusev crater, Mars, by aeolian modification of impact-generated sediment. *Journal of Geophysical Research: Planets*, *116*(E7), E00F22. https://doi.org/10.1029/2010JE003712

McLennan, S. M., Anderson, R. B., Bell, J. F., Bridges, J. C., Calef, F., Campbell, J. L., et al. (2013). Elemental Geochemistry of Sedimentary Rocks at Yellowknife Bay, Gale Crater, Mars. *Science*, 1244734. https://doi.org/10.1126/science.1244734

McSween, H. Y., & Keil, K. (2000). Mixing relationships in the Martian regolith and the composition of globally homogeneous dust. *Geochimica et Cosmochimica Acta*, *64*(12), 2155–2166. https://doi.org/10.1016/S0016-7037(99)00401-9

McSween, H. Y., Taylor, G. J., & Wyatt, M. B. (2009). Elemental Composition of the Martian Crust. *Science*, *324*(5928), 736–739. https://doi.org/10.1126/science.1165871

Ming, D. W., Mittlefehldt, D. W., Morris, R. V., Golden, D. C., Gellert, R., Yen, A., et al. (2006). Geochemical and mineralogical indicators for aqueous processes in the Columbia Hills of Gusev crater, Mars. *Journal of Geophysical Research: Planets*, *111*(E2), n/a–n/a. https://doi.org/10.1029/2005JE002560

Ming, D. W., Gellert, R., Morris, R. V., Arvidson, R. E., Brückner, J., Clark, B. C., et al. (2008). Geochemical properties of rocks and soils in Gusev Crater, Mars: Results of the Alpha Particle X-Ray Spectrometer from Cumberland Ridge to Home Plate. *Journal of Geophysical Research*, *113*(E12S39), 28 PP. https://doi.org/200810.1029/2008JE003195

Minitti, M. E., Malin, M. C., Van Beek, J. K., Caplinger, M., Maki, J. N., Ravine, M., et al. (2019). Distribution of primary and secondary features in the Pahrump Hills outcrop (Gale crater, Mars) as seen in a Mars Descent Imager (MARDI) “sidewalk” mosaic. *Icarus*, *328*, 194–209. https://doi.org/10.1016/j.icarus.2019.03.005

Morris, R. V., Golden, D. C., Bell, J. F., Shelfer, T. D., Scheinost, A. C., Hinman, N. W., et al. (2000). Mineralogy, composition, and alteration of Mars Pathfinder rocks and soils: Evidence from multispectral, elemental, and magnetic data on terrestrial analogue, SNC meteorite, and Pathfinder samples. *Journal of Geophysical Research: Planets*, *105*(E1), 1757–1817. https://doi.org/10.1029/1999JE001059

Morris, R. V., Vaniman, D. T., Blake, D. F., Gellert, R., Chipera, S. J., Rampe, E. B., et al. (2016). Silicic volcanism on Mars evidenced by tridymite in high-SiO2 sedimentary rock at Gale crater. *Proceedings of the National Academy of Sciences*, *113*(26), 7071–7076. https://doi.org/10.1073/pnas.1607098113

Morrison, S. M., Downs, R. T., Blake, D. F., Vaniman, D. T., Ming, D. W., Hazen, R. M., et al. (2018). Crystal chemistry of martian minerals from Bradbury Landing through Naukluft Plateau, Gale crater, Mars. *American Mineralogist*, *103*(6), 857–871. https://doi.org/10.2138/am-2018-6124

Nachon, M., Clegg, S. M., Mangold, N., Schröder, S., Kah, L. C., Dromart, G., et al. (2014). Calcium sulfate veins characterized by ChemCam/Curiosity at Gale crater, Mars. *Journal of Geophysical Research: Planets*, *119*(9), 1991–2016. https://doi.org/10.1002/2013JE004588

Nachon, M., Mangold, N., Forni, O., Kah, L. C., Cousin, A., Wiens, R. C., et al. (2017). Chemistry of diagenetic features analyzed by ChemCam at Pahrump Hills, Gale crater, Mars. *Icarus*, *281*, 121–136. https://doi.org/10.1016/j.icarus.2016.08.026

Nesbitt, H. W., & Wilson, R. E. (1992). Recent chemical weathering of basalts. *Am J Sci*, *292*(10), 740–777. https://doi.org/ 10.2475/ajs.292.10.740

Nesbitt, H. W., & Young, G. M. (1982). Early Proterozoic climates and plate motions inferred from major element chemistry of lutites. *Nature*, *299*(5885), 715–717.

O'Connell-Cooper, C. D., Spray, J. G., Thompson, L. M., Gellert, R., Berger, J. A., Boyd, N. I., et al. (2017). APXS-derived chemistry of the Bagnold dune sands: Comparisons with Gale crater soils and the global martian average. *Journal of Geophysical Research: Planets*, 2017JE005268. https://doi.org/10.1002/2017JE005268

O'Connell-Cooper, C. D., Thompson, L. M., Spray, J. G., Berger, J. A., VanBommel, S. J., Gellert, R., et al. (2018). Chemical Diversity of Sands Within the Linear and Barchan Dunes of the Bagnold Dunes, Gale Crater, as Revealed by APXS Onboard Curiosity. *Geophysical Research Letters*, *45*(18), 9460–9470. https://doi.org/10.1029/2018GL079026

O'Connell-Cooper, C. D., Thompson, L. M., Spray, J. G., Gellert, R., Berger, J. A., Boyd, N. I., et al. (2019). Compositional Trends Within the Murray formation, from the Base of Pahrump Hills to the End of the VRR Campaign, as Determined by APXS (Vol. 50, p. 3237). Presented at the Lunar and Planetary Science Conference. Retrieved from http://adsabs.harvard.edu/abs/2019LPI....50.3237O

Palucis, M. C., Dietrich, W. E., Hayes, A. G., Williams, R. M. E., Gupta, S., Mangold, N., et al. (2014). The origin and evolution of the Peace Vallis fan system that drains to the Curiosity landing area, Gale Crater, Mars. *Journal of Geophysical Research: Planets*, *119*(4), 2013JE004583. https://doi.org/10.1002/2013JE004583

Rampe, E. B., Ming, D. W., Blake, D. F., Bristow, T. F., Chipera, S. J., Grotzinger, J. P., et al. (2017). Mineralogy of an ancient lacustrine mudstone succession from the Murray formation, Gale crater, Mars. *Earth and Planetary Science Letters*, *471*, 172–185. https://doi.org/10.1016/j.epsl.2017.04.021

Rampe, E. B., Blake, D. F., Bristow, T. F., Ming, D. W., Vaniman, D. T., Morris, R. V., et al. (2020). Mineralogy and geochemistry of sedimentary rocks and eolian sediments in Gale crater, Mars: A review after six Earth years of exploration with Curiosity. *Geochemistry*, 125605. https://doi.org/10.1016/j.chemer.2020.125605

Rampe, E. B. B. (2019). The Mineralogical Record of Ancient Fluvio-Lacustrine Environments in Gale Crater as Measured by the MSL CheMin Instrument. Presented at the 9th International Conference on Mars, Pasadena, CA, United States. Retrieved from https://ntrs.nasa.gov/search.jsp?R=20190029095

Rieder, R., Gellert, R., Brückner, J., Klingelhöfer, G., Dreibus, G., Yen, A., & Squyres, S. W. (2003). The new Athena alpha particle X-ray spectrometer for the Mars Exploration Rovers. *Journal of Geophysical Research*, *108*(E12), 8066. https://doi.org/200310.1029/2003JE002150

Sara, M. (2017). Dyngjusandur sand sheet, Iceland, as a depositional analog to the Stimson Fm. in Gale Crater, Mars. *Theses and Dissertations*. https://doi.org/10.17077/etd.25rc5gg2

Schmidt, M. E., Campbell, J. L., Gellert, R., Perrett, G. M., Treiman, A. H., Blaney, D. L., et al. (2014). Geochemical diversity in first rocks examined by the Curiosity Rover in Gale Crater: Evidence for and significance of an alkali and volatile-rich igneous source. *Journal of Geophysical Research: Planets*, *119*(1), 64–81. https://doi.org/10.1002/2013JE004481

Schmidt, M. E., Perrett, G. M., Bray, S. L., Bradley, N. J., Lee, R. E., Berger, J. A., et al. (2018). Dusty Rocks in Gale Crater: Assessing Areal Coverage and Separating Dust and Rock Contributions in APXS Analyses. *Journal of Geophysical Research: Planets*, *123*(7), 1649–1673. https://doi.org/10.1029/2018JE005553

Schwenzer, S. P., & Kring, D. A. (2009). Impact-generated hydrothermal systems capable of forming phyllosilicates on Noachian Mars. *Geology*, *37*(12), 1091–1094. https://doi.org/10.1130/G30340A.1

Siebach, K. L., Baker, M. B., Grotzinger, J. P., McLennan, S. M., Gellert, R., Thompson, L. M., & Hurowitz, J. A. (2017). Sorting out Compositional Trends in Sedimentary Rocks of the Bradbury Group (Aeolus Palus), Gale Crater, Mars. *Journal of Geophysical Research: Planets*. Retrieved from http://onlinelibrary.wiley.com/doi/10.1002/2016JE005195/full

Siever, R. (1957). The Silica Budget in the Sedimentary Cycle. *American Mineralogist*, *42*(11–12), 821–841.

Stack, K. M., Grotzinger, J. P., Lamb, M. P., Gupta, S., Rubin, D. M., Kah, L. C., et al. (2019). Evidence for plunging river plume deposits in the Pahrump Hills member of the Murray formation, Gale crater, Mars. *Sedimentology*, *66*(5), 1768–1802. https://doi.org/10.1111/sed.12558

Stanley, C. R., & Madeisky, H. E. (1996a). Lithogeochemical exploration for metasomatic zones associated with hydrothermal mineral deposits using Pearce Element Ratio Analysis. *Short Course Notes on Pearce Element Ratio Analysis*.

Stanley, C. R., & Madeisky, H. E. (1996b). Lithogeochemical exploration for metasomatic zones associated with hydrothermal mineral deposits using Pearce element ratio analysis: Mineral Deposit Research Unit. *University of British Columbia, Short Course Notes*.

Stein, N., Grotzinger, J. P., Schieber, J., Mangold, N., Hallet, B., Newsom, H., et al. (2018). Desiccation cracks provide evidence of lake drying on Mars, Sutton Island member, Murray formation, Gale Crater. *Geology*, *46*(6), 515–518. https://doi.org/10.1130/G40005.1

Stein, T. C., Arvidson, R. E., Van Bommel, S. J., Wagstaff, K. L., & Zhou, F. (2019). MSL Analyst's Notebook: Curiosity APXS Concentration Data Integration and Mars Target Encyclopedia and Interface Updates. *Lunar and Planetary Science Conference*, 1820.

Stolper, E. M., Baker, M. B., Newcombe, M. E., Schmidt, M. E., Treiman, A. H., Cousin, A., et al. (2013). The Petrochemistry of Jake_M: A Martian Mugearite. *Science*, *341*(6153), 1239463. https://doi.org/10.1126/science.1239463

Sullivan, R., Arvidson, R., Bell, J. F., Gellert, R., Golombek, M., Greeley, R., et al. (2008). Wind-driven particle mobility on Mars: Insights from Mars Exploration Rover observations at "El Dorado" and surroundings at Gusev Crater. *Journal of Geophysical Research: Planets (1991–2012)*, *113*(E6). https://doi.org/doi:10.1029/2008JE003101

Sun, V. Z., Stack, K. M., Kah, L. C., Thompson, L., Fischer, W., Williams, A. J., et al. (2019). Late-stage diagenetic concretions in the Murray formation, Gale crater, Mars. *Icarus*, *321*, 866–890. https://doi.org/10.1016/j.icarus.2018.12.030

Sutter, B., McAdam, A. C., Mahaffy, P. R., Ming, D. W., Edgett, K. S., Rampe, E. B., et al. (2018). Evolved gas analyses of sedimentary rocks and eolian sediment in Gale Crater, Mars: Results of the Curiosity rover's sample analysis at Mars instrument from Yellowknife Bay to the Namib Dune. *Journal of Geophysical Research: Planets*, *122*(12), 2574–2609. https://doi.org/10.1002/2016JE005225

Swamy, V., Saxena, S. K., Sundman, B., & Zhang, J. (1994). A thermodynamic assessment of silica phase diagram. *Journal of Geophysical Research: Solid Earth*, *99*(B6), 11787–11794. https://doi.org/10.1029/93JB02968

Taylor, G. J., Boynton, W. V., McLennan, S. M., & Martel, L. M. V. (2010). K and Cl concentrations on the Martian surface determined by the Mars Odyssey Gamma Ray Spectrometer: Implications for bulk halogen abundances in Mars. *Geophysical Research Letters*, *37*(12). https://doi.org/10.1029/2010GL043528

Taylor, S. R., & McLennan, S. (2010). *Planetary Crusts: Their Composition, Origin and Evolution* (1st ed.). Cambridge University Press.

Thompson, L. M., Schmidt, M. E., Spray, J. G., Berger, J. A., Fairén, A. G., Campbell, J. L., et al. (2016). Potassium-rich sandstones within the Gale impact crater, Mars: The APXS perspective. *Journal of Geophysical Research: Planets*, 2016JE005055. https://doi.org/10.1002/2016JE005055

1433 Thompson, L. M. (2019). Compositional Characteristics and Trends Within the Vera Rubin
1434 Ridge, Gale Crater, Mars as Determined by APXS: Sedimentary, Diagenetic and
1435 Alteration History. Presented at the 50th Lunar and Planetary Science Conference,
1436 Woodlands, TX, United States. Retrieved from
1437 https://ntrs.nasa.gov/search.jsp?R=20190001846

1438 Thomson, B. J., Bridges, N. T., Milliken, R., Baldridge, A., Hook, S. J., Crowley, J. K., et al.
1439 (2011). Constraints on the origin and evolution of the layered mound in Gale Crater,
1440 Mars using Mars Reconnaissance Orbiter data. *Icarus*, *214*(2), 413–432.
1441 https://doi.org/10.1016/j.icarus.2011.05.002

1442 Treiman, A. H., Bish, D. L., Vaniman, D. T., Chipera, S. J., Blake, D. F., Ming, D. W., et al.
1443 (2016). Mineralogy, provenance, and diagenesis of a potassic basaltic sandstone on Mars:
1444 CheMin X-ray diffraction of the Windjana sample (Kimberley area, Gale Crater). *Journal*
1445 *of Geophysical Research: Planets*, *121*(1), 2015JE004932.
1446 https://doi.org/10.1002/2015JE004932

1447 VanBommel, S. J., Gellert, R., Berger, J. A., Campbell, J. L., Thompson, L. M., Edgett, K. S., et
1448 al. (2016). Deconvolution of distinct lithology chemistry through oversampling with the
1449 Mars Science Laboratory Alpha Particle X-Ray Spectrometer. *X-Ray Spectrometry*,
1450 *45*(3), 155–161. https://doi.org/10.1002/xrs.2681

1451 VanBommel, S. J., Gellert, R., Berger, J. A., Thompson, L. M., Edgett, K. S., McBride, M. J., et
1452 al. (2017). Modeling and mitigation of sample relief effects applied to chemistry
1453 measurements by the Mars Science Laboratory Alpha Particle X-ray Spectrometer. *X-Ray*
1454 *Spectrometry*. https://doi.org/10.1002/xrs.2755

1455 VanBommel, S. J., Gellert, R., Boyd, N. I., & Hanania, J. U. (2019a). Empirical simulations for
1456 further characterization of the Mars Science Laboratory Alpha Particle X-ray
1457 Spectrometer: An introduction to the ACES program. *Nuclear Instruments and Methods*
1458 *in Physics Research Section B: Beam Interactions with Materials and Atoms*, *441*, 79–87.
1459 https://doi.org/10.1016/j.nimb.2018.12.040

1460 VanBommel, S. J., Gellert, R., Berger, J. A., Yen, A. S., & Boyd, N. I. (2019b). Mars Science
1461 Laboratory Alpha Particle X-ray spectrometer trace elements: Situational sensitivity to
1462 Co, Ni, Cu, Zn, Ga, Ge, and Br. *Acta Astronautica*, *165*, 32–42.
1463 https://doi.org/10.1016/j.actaastro.2019.08.026

1464 Vaniman, D. T., Bish, D. L., Ming, D. W., Bristow, T. F., Morris, R. V., Blake, D. F., et al.
1465 (2014). Mineralogy of a Mudstone at Yellowknife Bay, Gale Crater, Mars. *Science*,
1466 *343*(6169), 1243480. https://doi.org/10.1126/science.1243480

1467 Weitz, C. M., Sullivan, R. J., Lapotre, M. G. A., Rowland, S. K., Grant, J. A., Baker, M., &
1468 Yingst, R. A. (2018). Sand Grain Sizes and Shapes in Eolian Bedforms at Gale Crater,
1469 Mars. *Geophysical Research Letters*, *45*(18), 9471–9479.
1470 https://doi.org/10.1029/2018GL078972

1471 Wiens, R. C., Maurice, S., Barraclough, B., Saccoccio, M., Barkley, W. C., Bell, J. F., et al.
1472 (2012). The ChemCam Instrument Suite on the Mars Science Laboratory (MSL) Rover:
1473 Body Unit and Combined System Tests. *Space Science Reviews*, *170*(1), 167–227.
1474 https://doi.org/10.1007/s11214-012-9902-4

Wiens, R. C., Maurice, S., Lasue, J., Forni, O., Anderson, R. B., Clegg, S., et al. (2013). Pre-flight calibration and initial data processing for the ChemCam laser-induced breakdown spectroscopy instrument on the Mars Science Laboratory rover. *Spectrochimica Acta Part B: Atomic Spectroscopy*, *82*, 1–27.

Wolfe, E. W., Wise, W. S., & Dalrymple, G. B. (1997). The Geology and Petrology of Mauna Kea Volcano, Hawaii: A Study of Postshield Volcanism. *US Geological Survey Professional Paper*, (1557), 1–129.

Yen, A. S., Gellert, R., Schröder, C., Morris, R. V., Bell, J. F., Knudson, A. T., et al. (2005). An integrated view of the chemistry and mineralogy of martian soils. *Nature*, *436*(7047), 49–54. https://doi.org/10.1038/nature03637

Yen, A. S., Morris, R. V., Gellert, R., Berger, J. A., Sutter, B., Downs, R. T., et al. (2017a). Hydrothermal Signatures at Gale Crater, Mars, and Possible In-Situ Formation of Tridymite. *AGU Fall Meeting Abstracts*, *2017*, P24B-04.

Yen, A. S., Ming, D. W., Vaniman, D. T., Gellert, R., Blake, D. F., Morris, R. V., et al. (2017b). Multiple stages of aqueous alteration along fractures in mudstone and sandstone strata in Gale Crater, Mars. *Earth and Planetary Science Letters*. https://doi.org/10.1016/j.epsl.2017.04.033

Yingst, R. A., Edgett, K. S., Kennedy, M. R., Krezoski, G. M., McBride, M. J., Minitti, M. E., et al. (2016). MAHLI on Mars: lessons learned operating a geoscience camera on a landed payload robotic arm. *Geoscientific Instrumentation, Methods and Data Systems*, *5*(1), 205–217.

Young, G. M., & Nesbitt, H. W. (1998). Processes controlling the distribution of Ti and Al in weathering profiles, siliciclastic sediments and sedimentary rocks. *Journal of Sedimentary Research*, *68*(3), 448–455. https://doi.org/10.2110/jsr.68.448

FIGURES

Figure 1: Distribution of APXS targets in the Gale stratigraphy.

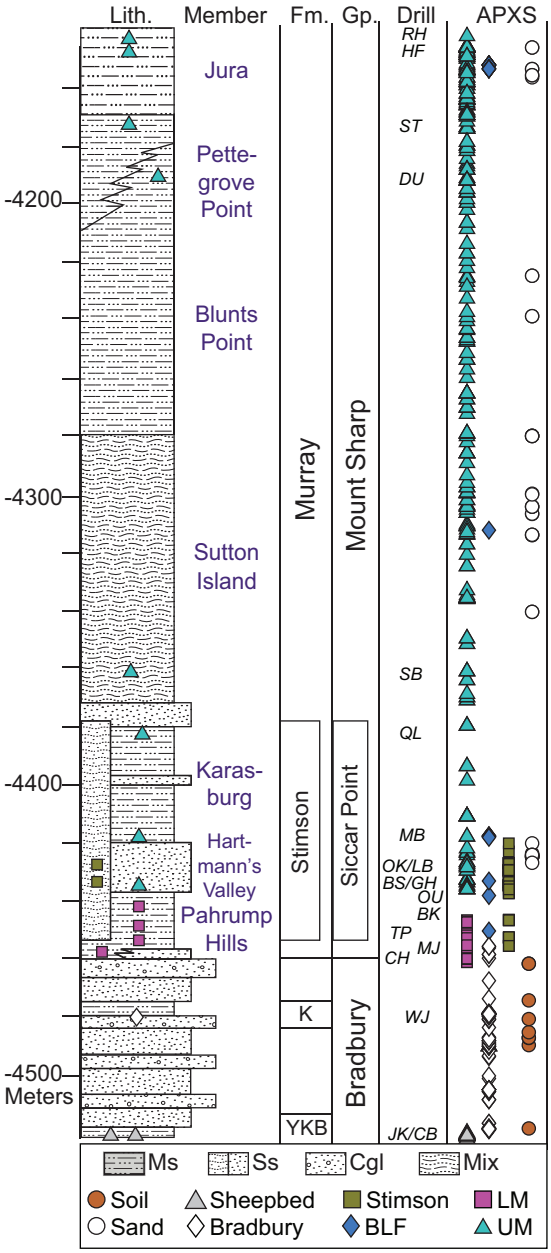

Figure 1: Distribution of APXS targets in the Gale stratigraphy adapted from (Grotzinger et al., 2015; Fedo et al., 2018; Stack et al., 2019) and the MSL Science Team. The y-axis shows elevation and the x-axis is unitless. The Kimberley and Yellowknife Bay formations are indicated with K and YKB, respectively. Approximate drill locations are shown with symbols on the unit lithology (lith.) and abbreviations are shown under the 'drill' column (see Tables 4 and 5). The key indicates mudstone (Ms), mixed mudstone, siltstone, and sandstone (Mix), sandstone (Ss), and conglomerate (Cgl). APXS targets are grouped primarily by stratigraphic unit, and secondarily by composition (see text). Murray formation targets are divided into lower Murray (LM) and upper Murray (UM). Bradbury-like float on top of Murray units is grouped separately (BLF). The APXS symbology is consistent with all figures herein.

Figure 2: Typical APXS spectra.

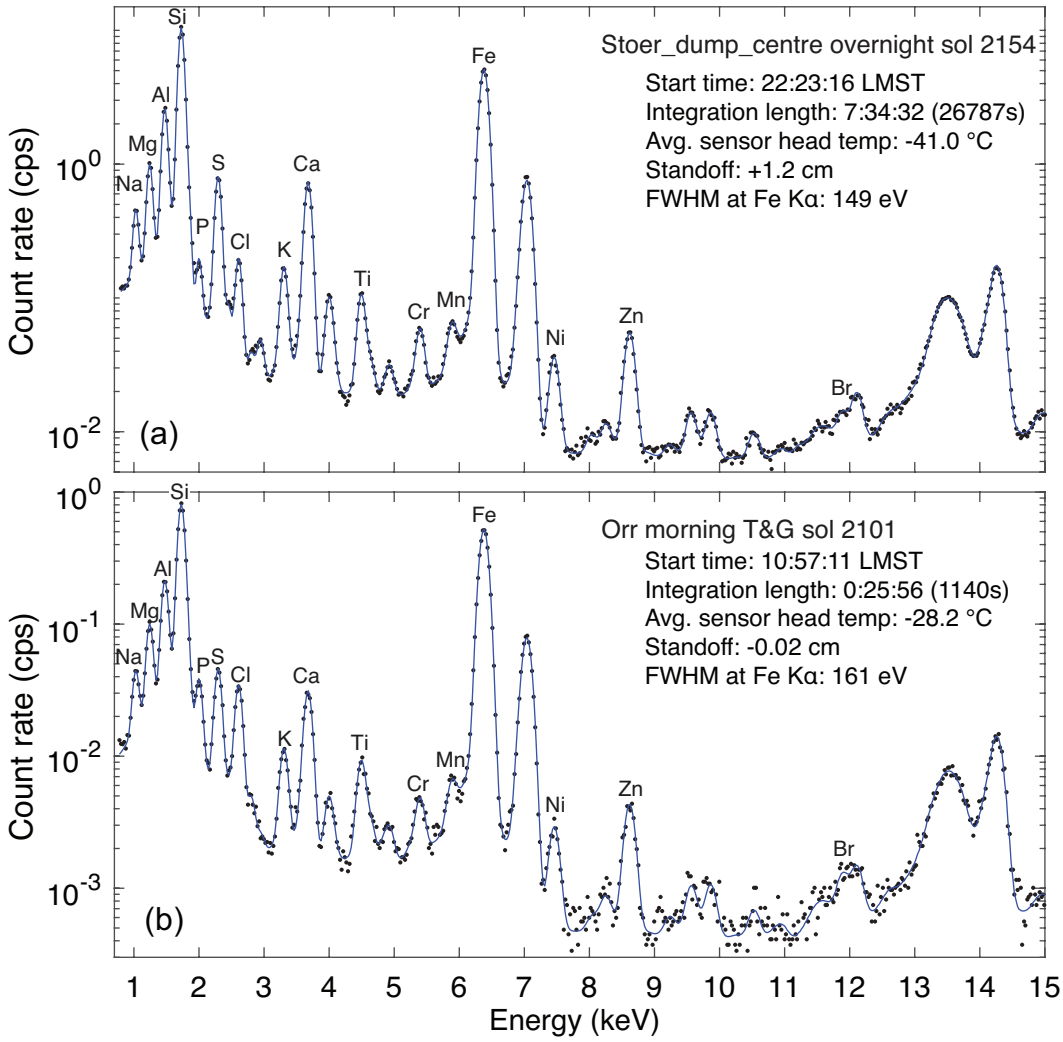

Figure 2: Typical APXS spectra showing the data (dots) and fit (line). (a) This spectrum was acquired on sol 2154 on the dumped DBA fines of the drill target Stoer and is representative of a high-quality overnight (8 h) measurement. (b) This touch-and-go (T&G) spectrum was acquired on sol 2101 on the target Orr and demonstrates that high quality spectra are possible with short integrations (25 m) in mornings before the temperature is too high. For comparison, one of the ~9 low-quality spectra is shown in Figure S2. Kα peaks of the 16 elements reported in Tables 3 and S1 are indicated. The full APXS spectrum is not shown (15-25 keV is omitted).

Figure 3: MAHLI images of example APXS drill campaign (Okoruso)

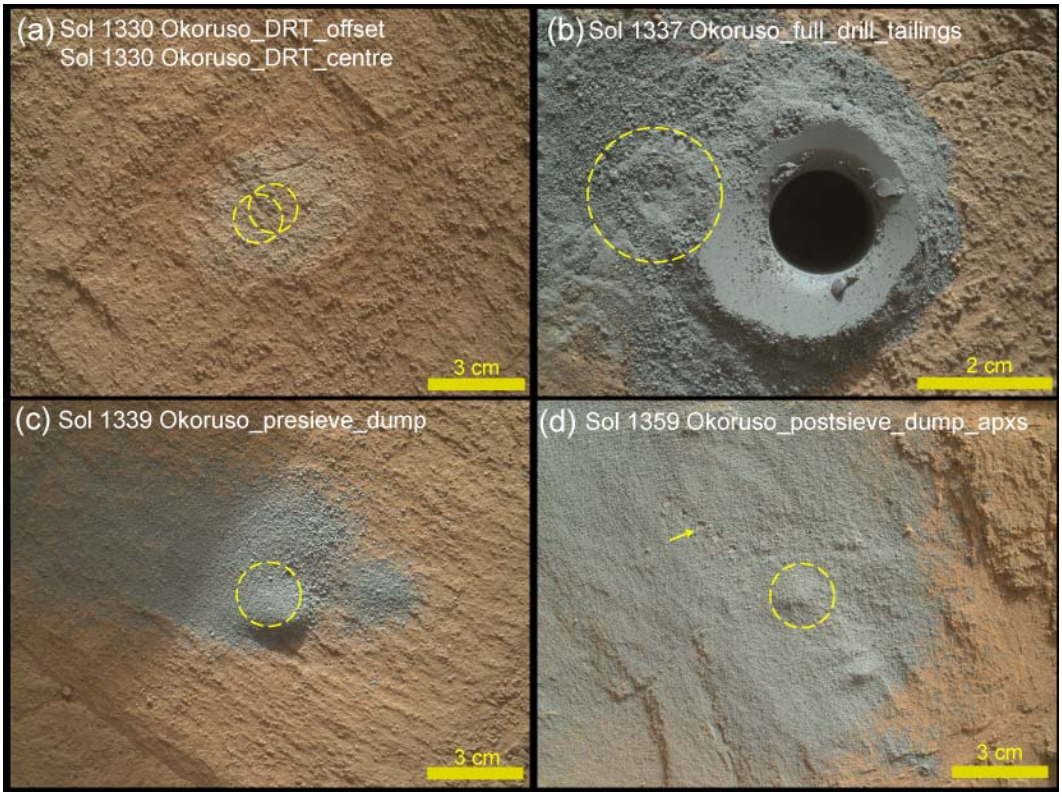

Figure 3: MAHLI context images of a representative example APXS drill campaign (Okoruso drill site). The sol and APXS target name are shown and yellow circles denote the approximate APXS FOV. MAHLI image identification numbers are given below. (a) Before drilling, two APXS measurements were obtained after the drill site was brushed by the DRT: one centered in the DRT area and one offset ~1 cm to investigate possible heterogeneity on the surface (1330MH0006000010501161C00). The brushed area is the lighter-toned oval ~4 cm wide. (b) One APXS measurement of the drill tailings was centered on the tailings adjacent to the drill hole (1332MH0005930010501233C00). (c) The pre-sieve drill fines were dumped on the ground and the APXS was placed over the thickest portion of the pile (1339MH0001900010501515C00). (d) About 20 sols after driving away from the Okoruso drill site, the post-sieve drill fines were dumped on the ground for APXS analysis (1359MH0001900010502139C00). This post-sieve dump pile measurement was successful because the fines fill the APXS FOV and the pile is >200 μm thick, and it is thus the best representative APXS analysis of the CheMin sample (Tables 4 and 5). The arrow indicates one of five LIBS pits in the fines created by ChemCam.

Figure 4: Volatile-free alkali-silica diagram.

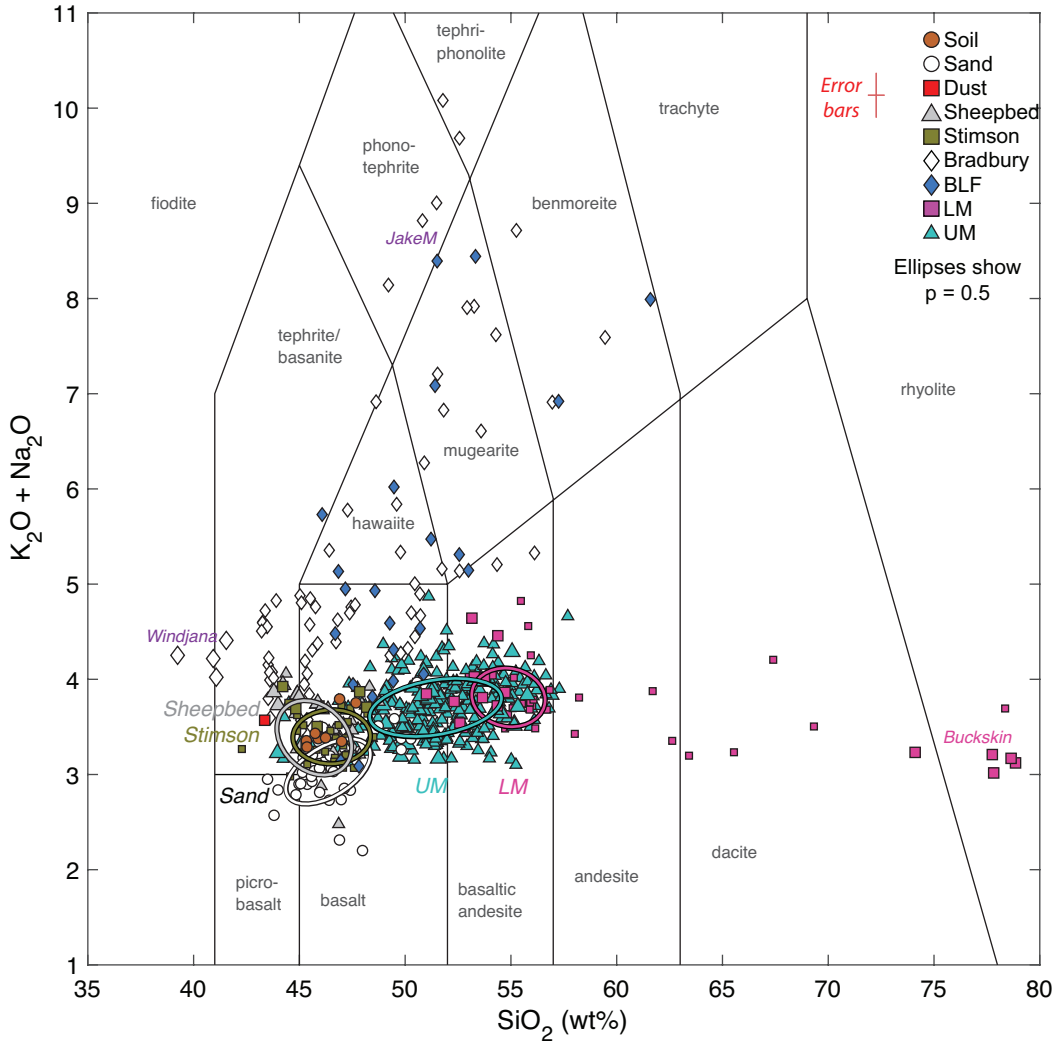

Figure 4: Volatile-free, total alkali versus silica diagram (Maitre et al., 2002) for Gale crater rocks, soils, sand, and dust. Veins, alteration haloes, and other diagenetic features are omitted. Concentrations are renormalized to 100 wt% without SO_3 and Cl. Drill fines are indicated by the larger symbols and Mahalanobis ellipses (probablility = 0.5) are shown for sand, the Sheepbed member, and the Stimson and Murray formations (UM and LM) to aid interpretation of overlapping data points. The Lower Murray (LM) ellipse excludes the high SiO_2 Buckskin targets. Error bars are omitted for clarity; typical error bars are shown.

Figure 5: Volatile element enrichment in soil, sand, dust.

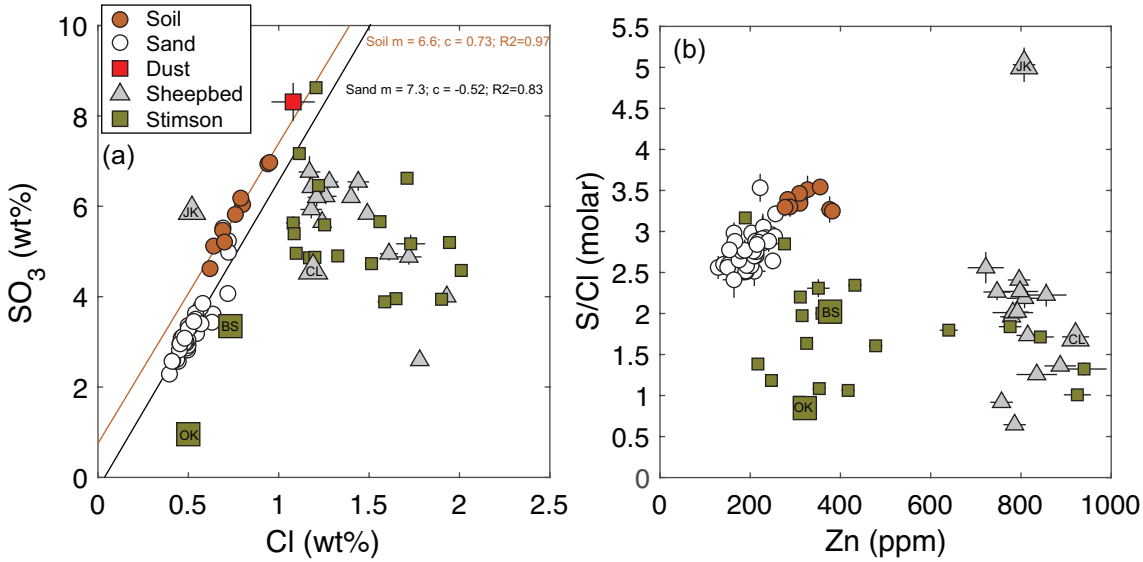

Figure 5: Volatile element concentrations in soil, sand, and dust compared to the basaltic bedrock units Sheepbed and Stimson. The larger symbols denote drill fines from the four drill sites in bedrock: John Klein (JK), Cumberland (CL), Big Sky (BS), and Okoruso (OK). The dust composition is shown in (a) (Berger et al., 2016).

Figure 6: P_2O_5 versus SO_3, Cl, and Zn in sand and soil.

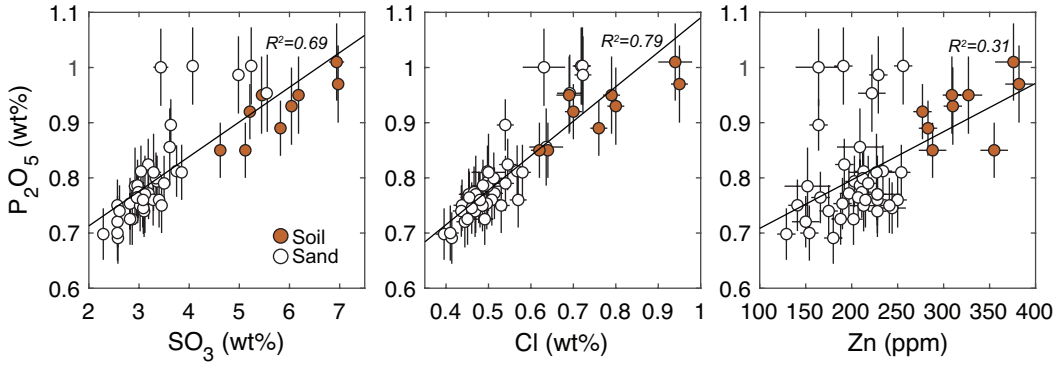

Figure 6: P_2O_5 versus SO_3, Cl, and Zn in sand and soil. The line shows the ordinary least squares regression and R^2 is denoted.

Figure 7: Major element ratios in Gale rocks.

Figure 7: Major element ratios Mg/Si versus Al/Si for (a) the Bradbury group, (b) the Murray formation, and (c) the Stimson formation. The black line delineates a trend consistent with fractionation of mafic/felsic materials, and deviation from this trend indicates open-system alteration (Ming et al., 2006). Larger symbols denote drill fines. Targets discussed in the text and the high silica trends associated with Buckskin (BK; red arrow) and the Stimson fracture haloes (blue arrow) are indicated.

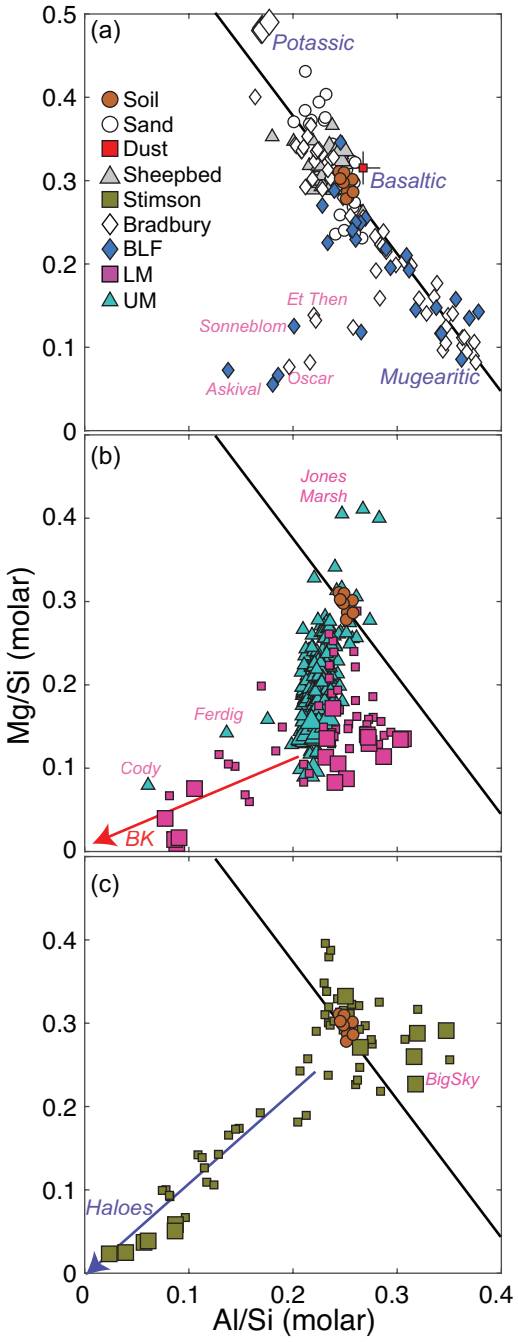

Figure 8: Element ratios for lithified basaltic units

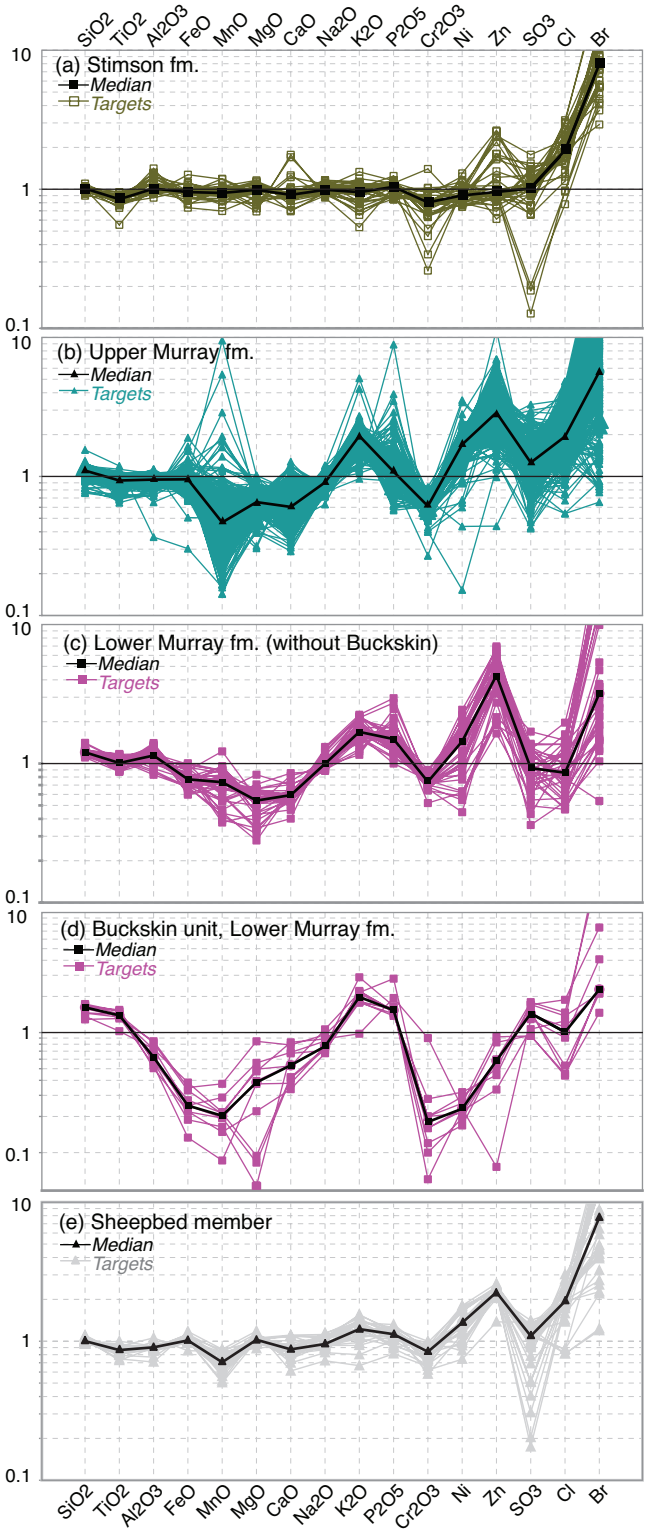

Figure 8: Element ratios in the lithified basaltic sedimentary units, normalized by soil (Sourdough sol 673). The units are shown in stratigraphic order (Figure 1): (a) Stimson formation, (b) upper Murray formation, (c) lower Murray formation excluding the Buckskin unit, (d) the SiO_2-enriched Buckskin unit shown separately for clarity, and (e) the Sheepbed member. Targets with prominent Ca-sulfate veins (SO_3 >15 wt%) are omitted.

Figure 9: Alkalic units

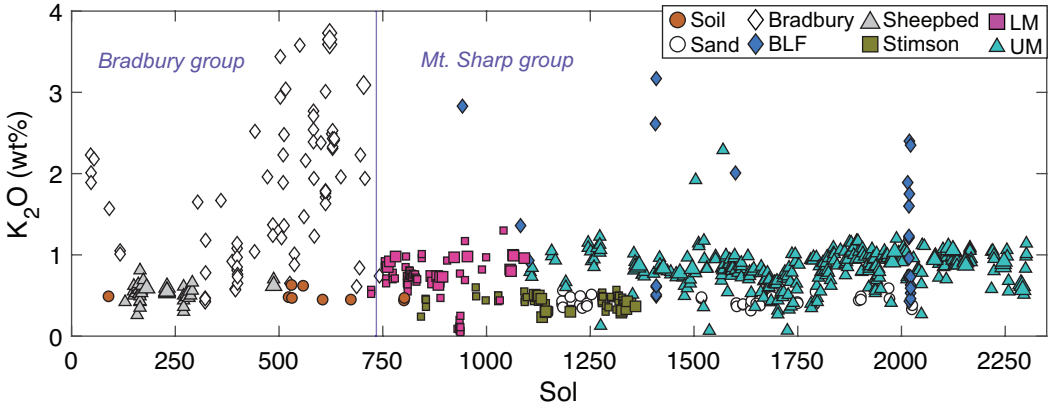

Figure 9: A plot of K_2O versus sol demonstrates the distribution of alkalic rocks along the traverse. The alkalic rocks in the Bradbury group are a mix of outcrop and float; all of the alkalic rocks discovered after sol ~750 on Mt. Sharp units are float (Bradbury-like float; BLF). The Bradbury/Mt. Sharp contact is indicated with the vertical line.

Figure 10: Minor and trace elements in alkalic units

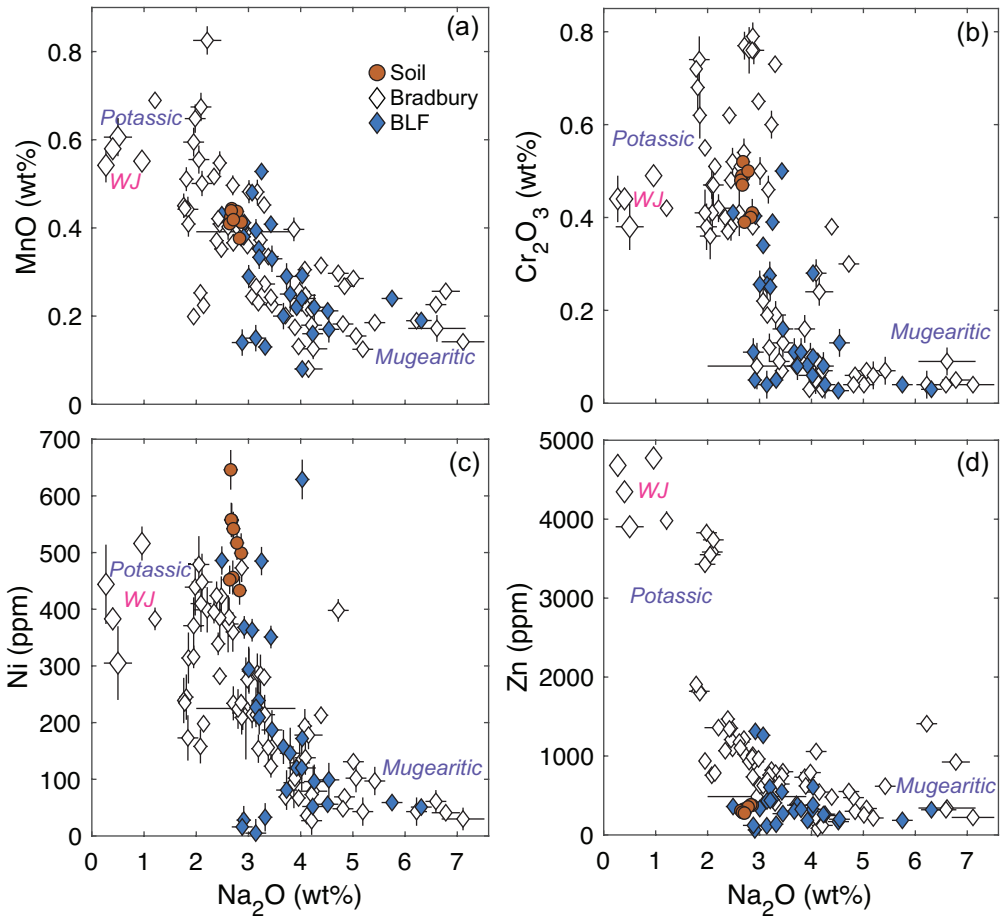

Figure 10: Selected minor and trace elements (a) MnO, (b) Cr_2O_3, (c) Ni, and (d) Zn versus Na_2O in alkalic units. The four measurements of Windjana drill fines (WJ; larger symbols) are denoted.

Figure 11: Fracture halo ratios

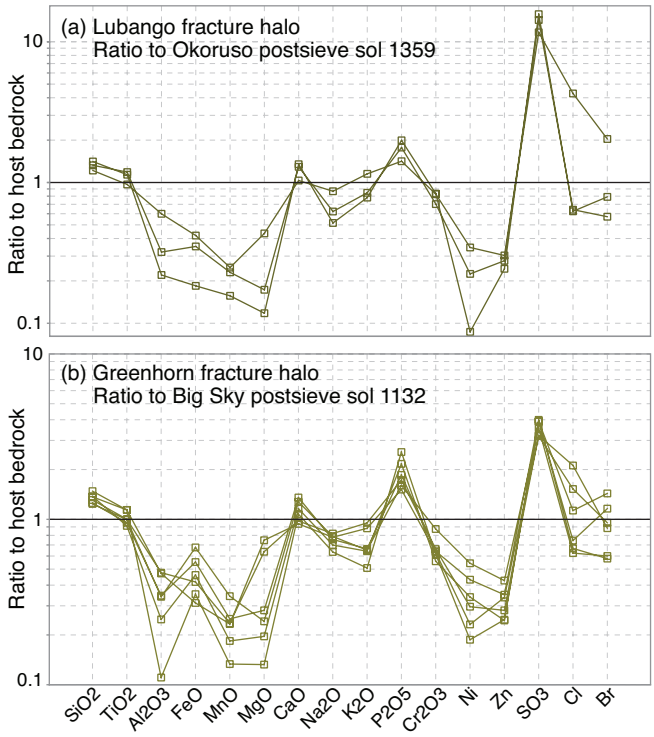

Figure 11. Element ratios of the (a) Lubango and (b) Greenhorn silica-rich haloes normalized by the adjacent, less altered host Stimson formation bedrock.

Figure 12: Calcium and sulfur

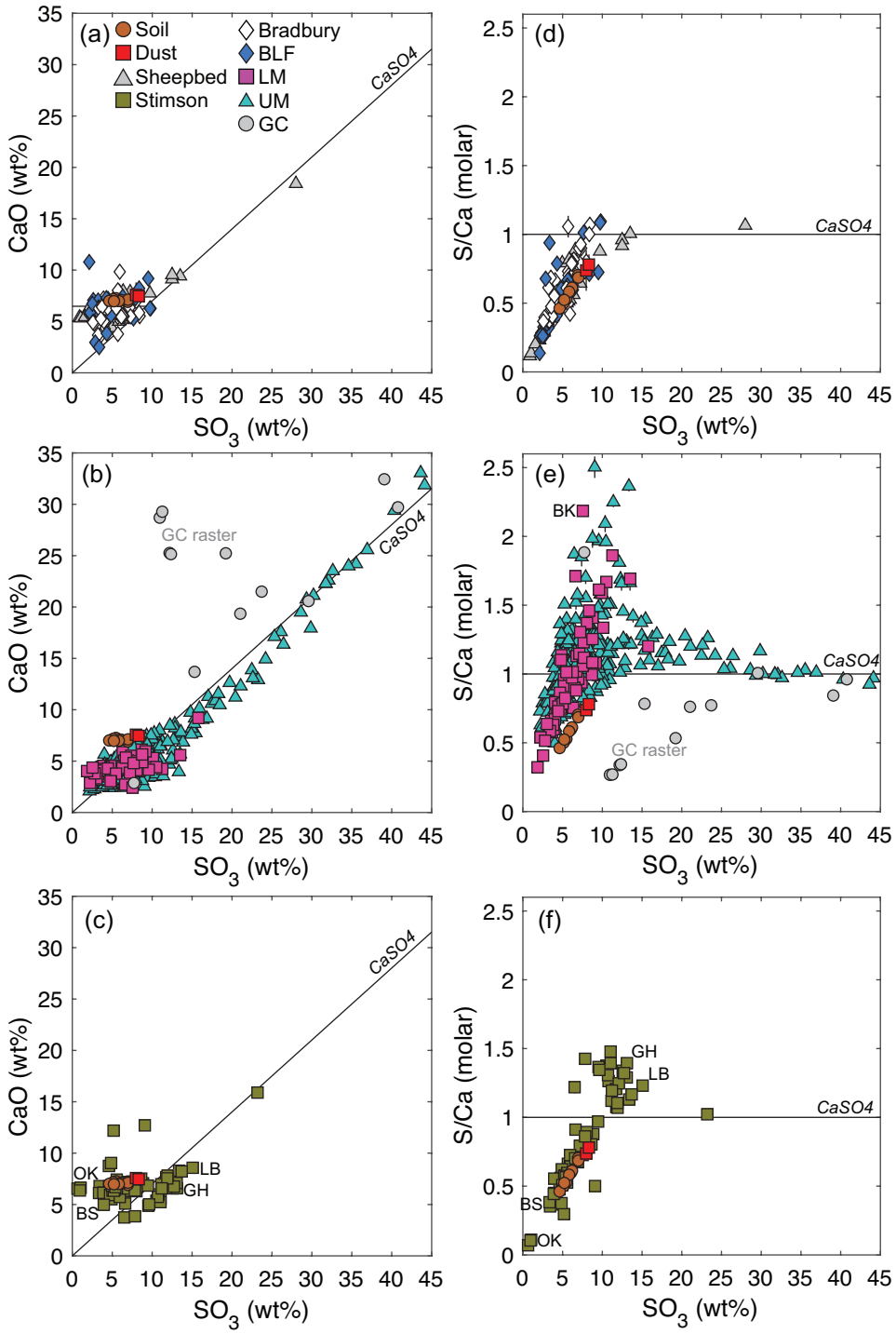

Figure 12: Calcium and S/Ca versus sulfur in alkalic units (a, d), the Murray formation (b, e), and the Stimson formation (c, f). Rasters of Mg-sulfate features are omitted; see Figures 13 and SQW12. The Garden City raster points (GC; sols 930-948) and selected drill targets are denoted. The simple mixing line of pure $CaSO_4$ is shown.

Figure 13: Variation of MgO and CaO with SO_3 in Murray formation bedrock.

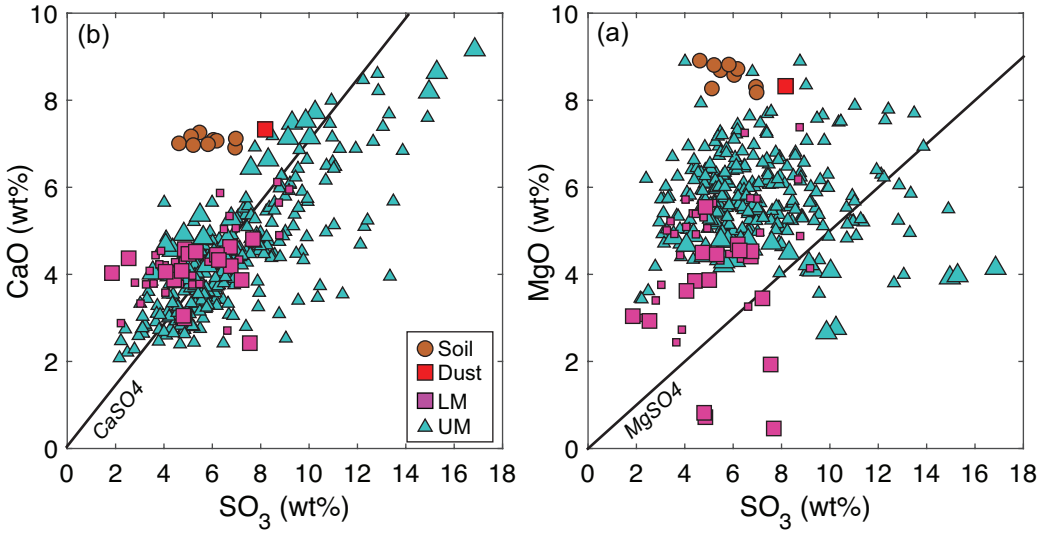

Figure 13: Variation of (a) CaO and (b) MgO with SO_3 in Murray formation bedrock. Drill fines are denoted by larger symbols. The pure mixing lines of $MgSO_4$ and $CaSO_4$ are shown. Targets with Ca-sulfate veins and Mg-sulfate concretions are omitted. The CaO and SO_3 correlation is evidence of Ca-sulfate in the bedrock matrix, although the influence of small veins (< 1 mm) or unseen veins are difficult to assess with MAHLI imagery.

Figure 14: Cl and Br concentrations.

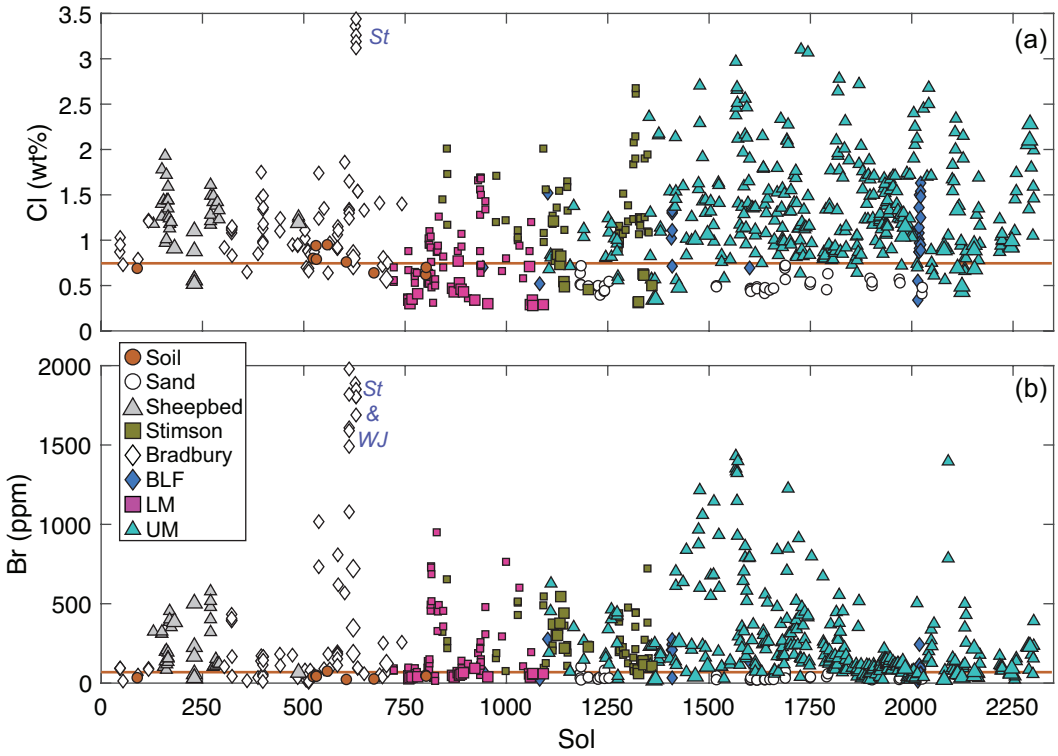

Figure 14: (a) Chlorine and (b) bromine concentrations versus sol for all Gale crater targets. Highly enriched targets Windjana (WJ; sols 612-704) and Stephen (St; sols 627-629) are indicated, and the brown line denotes the median soil concentration.

Figure 15: Evaluation of target preparation methods wrt Cl, Br, SO_3, and S/Cl of unbrushed, brushed, and drilled bedrock.

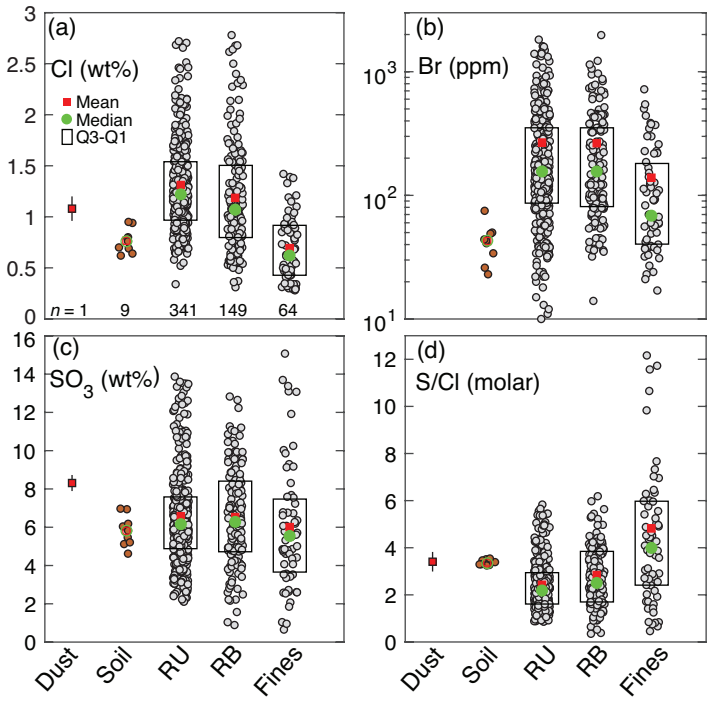

Figure 15: Evaluation of target preparation methods (i.e., brushing and drilling) with respect to the (a) Cl, (b) Br, (c) SO_3, and (d) molar S/Cl in dust, soil, unbrushed (RU), brushed (RB), and drilled (fines) APXS targets. Sulfur- and chlorine-rich veins, concretions, and other diagenetic features are omitted. The number of targets (*n*) for each category is shown in (a). The red square is the mean, the green square is the median, and the box contains the middle 50% of the data.

Figure 16: Murray formation Cl versus Na and K.

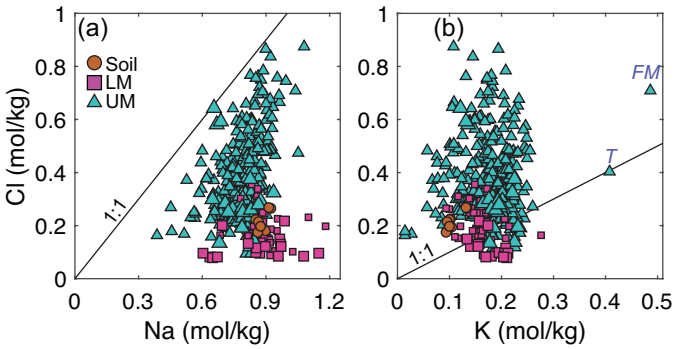

Figure 16: Molar Cl versus (a) Na and (b) K in Murray formation targets. The upper Murray formation has a weak positive correlation between Cl and Na ($r = 0.43$) and no correlation between Cl and K ($r = 0.01$). The 1:1 line shows the pure NaCl and KCl mixing lines. The K-rich targets Thrumcap (T; sol 1504) and Fresh Meadow (FM; sol 1570) are indicated and larger symbols denote drill fines.

Figure 17: P_2O_5 versus sol.

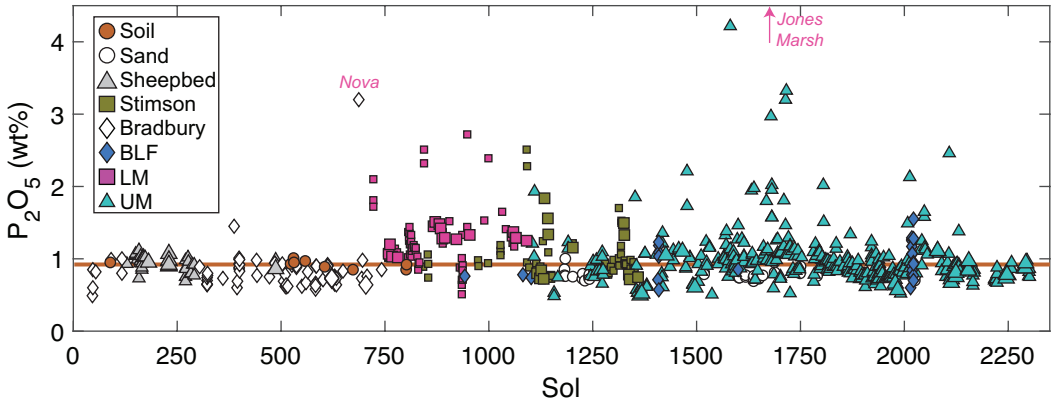

Figure 17: P_2O_5 versus sol. The unique, high P_2O_5 target named Nova is denoted (sol 687) and the target named Jones Marsh (sol 1727; indicated by arrow) with very high P_2O_5 (7.56 ± 0.40 wt%) is not shown. The brown line denotes the median soil concentration.

Figure 18: P_2O_5 versus SiO_2 in Mt. Sharp rocks.

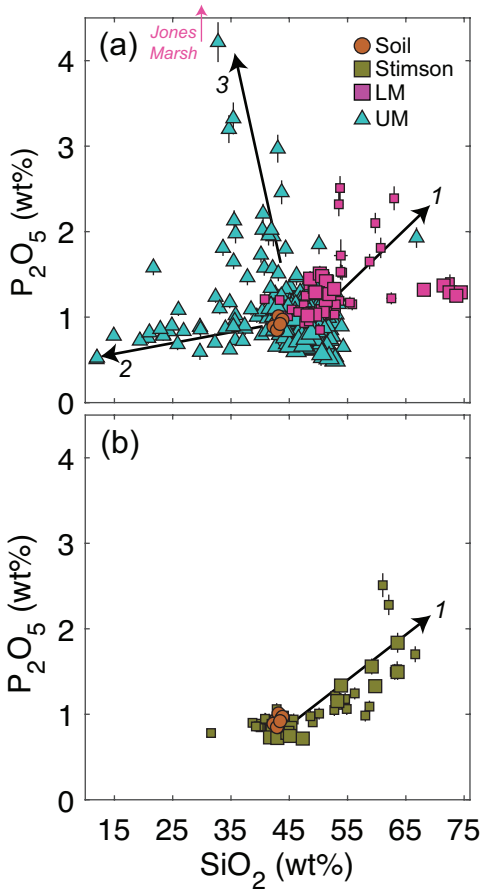

Figure 18: P_2O_5 versus SiO_2 in (a) Murray formation and (b) Stimson formation rocks. The black arrows indicate three trends: (1) bedrock with elevated SiO_2 and P_2O_5 primarily in the lower Murray formation units and Stimson formation Si-rich haloes, (2) bedrock with prominent Ca-sulfate veins in the FOV, and (3) localized, P-rich diagenetic features in the upper Murray units. The red arrow denotes the SiO_2 content of the Jones Marsh with very high P_2O_5 (7.56 ± 0.40 wt%).

Figure 19: Element ratio indicator plots for basaltic fractionation and/or sorting trends

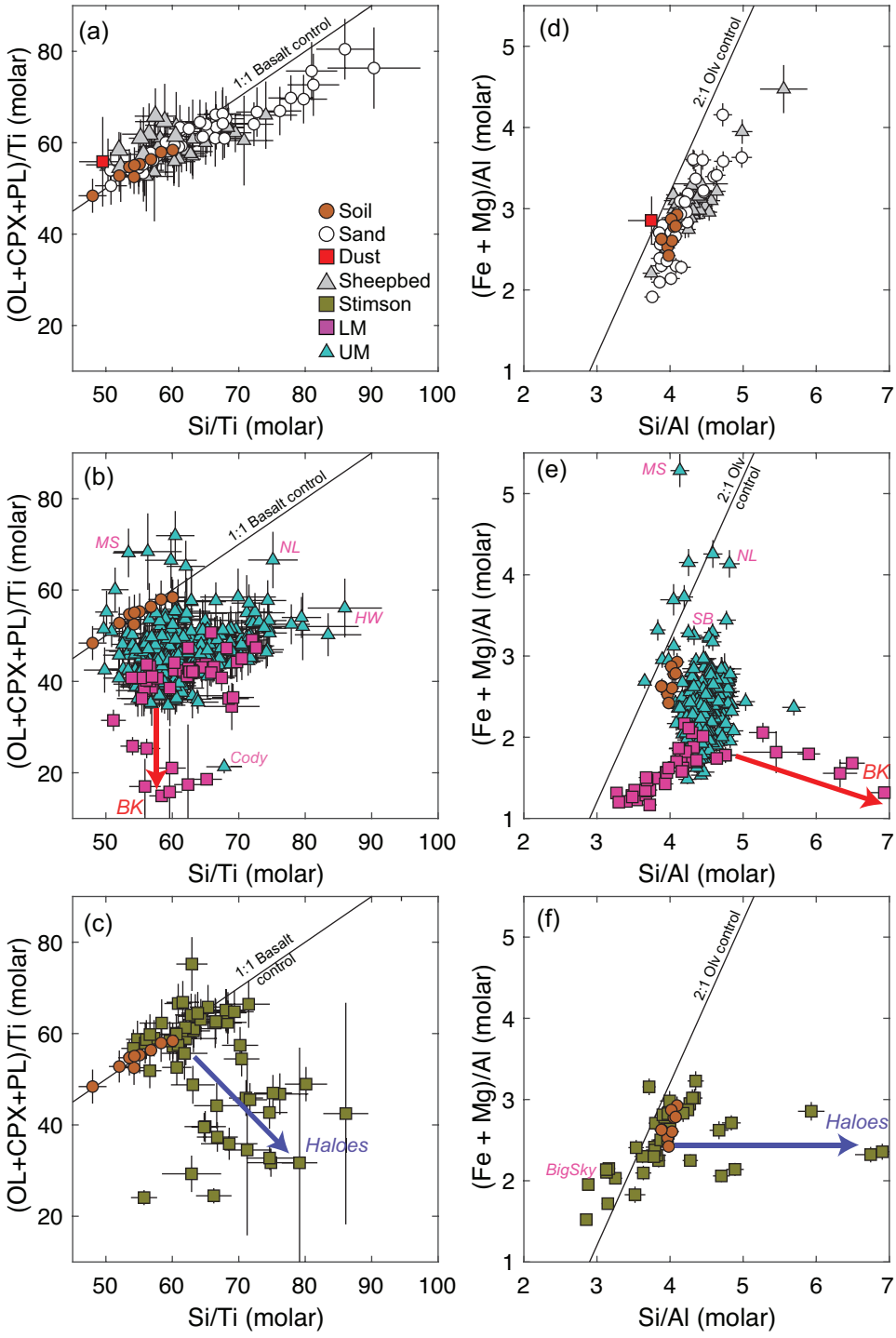

Figure 19: Element ratio indicator plots for fractionation and/or sorting trends in (a-c) a basaltic mineral assemblage containing olivine, clinopyroxene, and plagioclase (OL+CPX+PL) and (d- f) olivine, showing the APXS results for the basaltic units. Ca-sulfate veins are omitted, and the units are shown separately for clarity: (a, d) soil, sand, dust, and the Sheepbed member, (b, e) the Murray

formation, and (c, f) the Stimson formation. The Buckskin (BK) and fracture halo trends are indicated by the blue vectors. For clarity, the full range of Si/Al values for BK (up to 13) and the Stimson haloes (up to 18 is not shown in (f) (see Figure S11). Selected diagenetic features are denoted: Fe-rich Morancy Stream (MS), Newport Ledge (NL), and Sagadahoc Bay (SB); Ti-depleted Haroldswick raster (HW).

Figure 20: Alkalic units

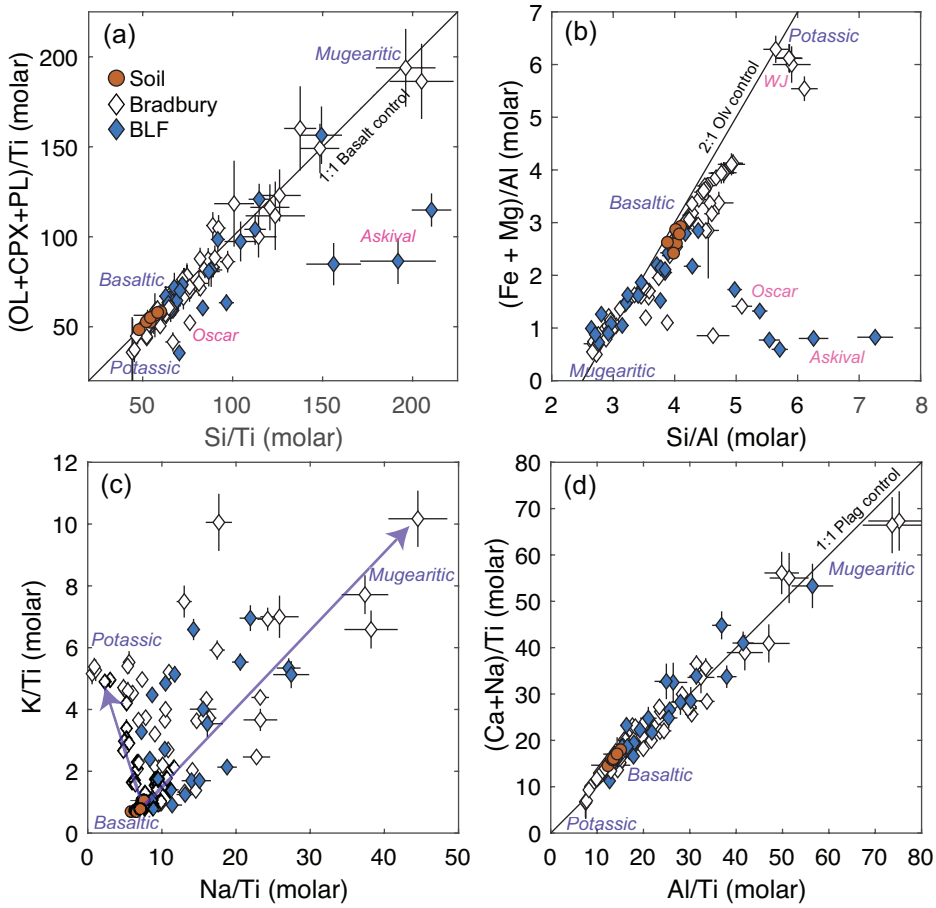

Figure 20: Element ratio indicator plots for fractionation and/or sorting trends in (a) basaltic minerals (OL+CPX+PL), (b) olivine, (c) alkali feldspar, and (d) plagioclase, showing the APXS results for the alkalic units. Three endmembers that delineate trends discussed in the text are denoted: basaltic, mugearitic, and potassic. Geochemical control lines are shown (Stanley & Madeisky, 1996b). Targets with Ca-sulfate veins are omitted.

Figure 21: Modeled Si-rich compositions compared to measured compositions.

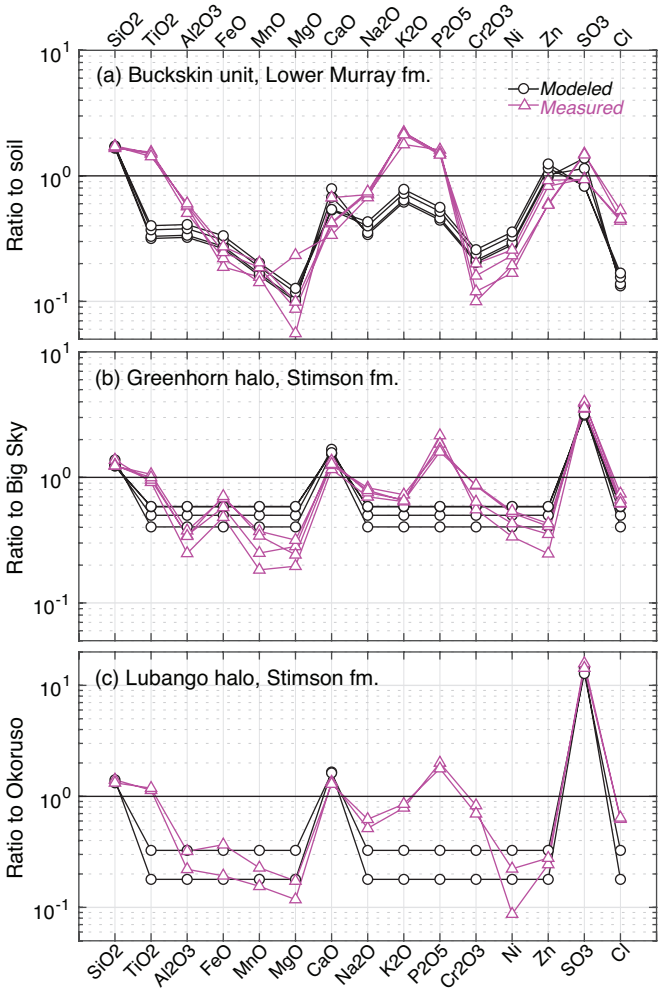

Figure 21: Tests of simple SiO_2 addition models (See supplemental text S2). (a) Measured Buckskin normalized to soil is compared to the modeled composition derived from SiO_2 and Ca-sulfate addition as proposed by Hurowitz et al. (2017). (b) Measured Greenhorn normalized to the less altered parent Big Sky and compared to the modeled composition of simple pure SiO_2 and Ca-sulfate added to a Big Sky composition. (c) Lubango normalized to the less altered parent Okoruso and compared to a modeled Okoruso composition with pure SiO_2 and Ca-sulfate added. Note that the model does not fit well with the observed Ti, K, and P concentrations.

TABLES

Table 1: APXS precision error and accuracy

	Concentration: Stoer[1] drill fines (wt%)	Statistical fitting error (wt%)	Relative accuracy[2] (%)	Limit of detection[2] (wt%)
SiO_2	44.1	0.54	3	1
TiO_2	1.03	0.03	20	0.2
Al_2O_3	8.75	0.19	7	1
FeO	21.5	0.26	7	0.03
MnO	0.17	0.01	8	0.05
MgO	4.72	0.17	14	1
CaO	6.44	0.07	7	0.2
Na_2O	2.45	0.14	11	1
K_2O	0.91	0.04	15	0.2
P_2O_5	0.84	0.05	15	0.3
Cr_2O_3	0.34	0.01	19	0.05
Ni (ppm)	915	50	16	50
Zn(ppm)	850	30	16	30
SO_3	7.59	0.10	15	0.2
Cl	0.89	0.02	30	0.2
Br (ppm)	45	5	20	20

[1] Representative error for an overnight measurement is taken from the sol 2154 analysis of Stoer_dump_centre (spectrum shown in Figure 2a).

[2] Accuracy and limit of detection determined by APXS calibration (Gellert & Clark, 2015).

Table 2: Description of sample preparation methods

Preparation type	Abbreviation (Table 3)	Description	Number of targets[1]
Unbrushed rock	RU	As-is, unbrushed rock surface	408
Brushed rock	RB	Rock surface after brushing by DRT	167
Minidrill	MD	Shallow test drill; ~2-5 mm in depth; APXS deployed over chipped/abraded rock	12
Drill tailings	DT	Drill tailings ejected from the hole without being acquired by SA/SPaH, extracted from a range of depths in the drill hole up to ~5 cm and primarily from the top 2-3 cm	27
DBA drill fines	DBA	Sample dumped from the drill bit assembly (DBA) using the feed extended drilling and feed extended sample transfer (FED/FEST) techniques (sols >1536)	7
Sieved < 150 µm	Postsieve	Sample processed by SA/SPaH, sieved to <150 µm, and dumped on the ground. The targets include "postsieve" in the name	16
Sieved >150 µm	Presieve	Sample processed by SA/SPaH that did not pass through the 150 µm sieve, and dumped on the ground. The targets include "presieve" in the name	10
Sieved 150-1000 µm	Sieve150µm-1mm	Sample processed by SA/SPaH, sieved to 150-1000 µm, and dumped on the ground.	1
Sieved >1000 µm	Sieve1mm	Sample processed by SA/SPaH, sieved to >1000 µm, and dumped on the ground	1
Undisturbed soil/sand	SU	Soil and sand as-is, untouched by the rover hardware	33
Disturbed soil/sand	SD	Soil and sand that has been disturbed by the rover's scoop and/or wheels	9
Failed drill fines	Failed	Sample fines dumped by SA/SPaH but did not fill the APXS FOV and/or was not infinitely thick with respect to APXS sampling depth	21

[1]Number of APXS targets of each preparation method as of sol 2068.

Table 3: APXS results for first 2301 sols of the MSL mission

Table 3: APXS results for the first 2301 sols of the MSL mission. This table is attached as a file named “Berger_table_3_apxs_results_sol2301_v4.xlsx”.

Table 4: APXS results for drilled and scooped samples

APXS results for drilled and scooped samples (sols 0-2301)

Target Name	Sol	Strat Unit	Drill Site (Abbrv.)[1]	Sample Prep[2]	Temperature[3] (C)	Stand off distance (cm)	Lifetime	FWHM Fe (eV)
PortageRP	89	Soil	Rocknest (RN)	SD	-62	2.11	03:14:02	145
APXS_Drill_Site_Raster_Integration_Site 7	230	Sheepbed	John Klein (JK)	Post-sieve	-43	1.48	04:02:14	157
Cumberland_dump_pile_center	487	Sheepbed	Cumber-land (CB)	Post-sieve	-65	1.63	02:00:00	144
DumpPile_Windjana	704	Dillinger	Windjana (WJ)	Post-sieve	-39	0.26	08:00:00	147
Confidence_Hills_fines_postsieve_dump	781	Pahrump Hills	Confidence Hills (CH)	Post-sieve	-42	0.41	04:00:00	145
Mojave2_postsieve_dump	894	Pahrump Hills	Mojave (MJ)	Post-sieve	-40	0.4	04:00:00	147
Telegraph_Peak_postsieve_dump	954	Pahrump Hills	Telegraph Peak (TP)	Post-sieve	-34	0.48	06:30:00	152
Buckskin_post_sieve_dump_twk_corrected	1092	Pahrump Hills	Buckskin (BK)	Post-sieve	-63	0.67	04:00:00	152
Big_Sky_postsieve_dump	1132	Stimson	Big Sky (BS)	Post-sieve	-62	0.42	05:30:00	152
Greenhorn_postsieve_dump	1202	Stimson	Greenhorn (GH)	Post-sieve	-63	0.46	07:00:00	153
Gobabeb_DumpA_APXS	1226	Bagnold Dunes	Gobabeb (GB)	Post-sieve	-65	0.14	07:30:00	148
Lubango_presieve_apxs	1326	Stimson	Lubango (LB)	Pre-sieve	-38	0.5	04:00:00	146
Okoruso_postsieve_dump_apxs	1359	Stimson	Okoruso (OK)	Post-sieve	-39	0.29	08:00:00	146
Oudam_presieve_dump	1368	Hartmann's Valley	Oudam (OU)	Pre-sieve	-41	0.25	08:00:00	146
Marimba2_full_drill_tailings	1426	Karasburg	Marimba (MB)	Tailings	-43	0.25	04:22:19	145
Quela_full_drill_tailings	1466	Karasburg	Quela (QL)	Tailings	-41	1.48	05:30:00	145
Sebina_full_drill_tailings[4]	1496	Sutton Island	Sebina (SB)	Tailings	-41	2.15	04:00:00	145
Ogunquit_Beach_postsieve_dump	1969	Bagnold Dunes	Ogunquit Beach (OB)	Post-sieve	-41	0.82	07:00:00	148
Duluth_DBA_dump_center	2080	Blunts Point	Duluth (DU)	DBA fines	-42	0.67	08:00:00	147
Stoer_dump_centre	2154	Pettegrove Point	Stoer (ST)	DBA	-41	0.83	07:26:27	149
Highfield_dump_centre[5]	2245	Jura	Highfield (HF)	DBA	-40	0.87	01:07:02	148
Rock_Hall_dump_corrected	2291	Jura	Rock Hall (RH)	DBA	-43	0.68	07:00:00	149

[1] Note that the abbreviations listed here correspond with those discussed in presentations of results from CheMin (e.g., Bristow et al., 2018) and SAM (e.g., Sutter et al., 2018).
[2]See Table 2 for an explanation of preparation methods.
[3]Temperature indicates average temperature of the APXS sensor head chassis.
[4]Wind activity impacted the Sebina drill campaign. See supplemental text S1.
[5]Highfield_dump_offset on sol 2245 was of comparable quality and has small compositional differences.

Table 4 continued: APXS best results for CheMin and SAM samples

Compositions of best drilled and scooped samples determined by the APXS (sols 0-2301)

Target Name	Sol	SiO_2	TiO_2	Al_2O_3	FeO	MnO	MgO	CaO	Na_2O	K_2O	P_2O_5	Cr_2O_3	Ni ppm	Zn ppm	SO_3	Cl	Br ppm
PortageRP	89	43.0	1.19	9.37	19.2	0.42	8.69	7.26	2.70	0.49	0.95	0.49	460	330	5.47	0.69	30
APXS_Drill_Site_Raster_Integration_Site7	230	41.1	1.05	8.51	20.7	0.33	8.97	7.87	2.93	0.55	0.92	0.47	710	810	5.91	0.52	30
Cumberland_dump_pile_center	487	41.1	0.99	8.63	22.0	0.29	9.32	6.66	3.01	0.62	0.86	0.46	930	920	4.61	1.19	70
DumpPile_Windjana	704	37.4	1.07	5.62	27.9	0.55	12.3	5.26	0.96	3.09	0.64	0.49	520	4780	3.57	0.57	120
Confidence_Hills_fines_postsieve_dump	781	48.1	1.13	9.73	19.8	0.37	5.55	4.58	2.65	0.98	1.02	0.39	930	2110	4.86	0.41	40
Mojave2_postsieve_dump	894	49.5	1.19	11.4	16.1	0.40	4.55	4.33	3.01	0.73	1.29	0.37	1030	2200	6.27	0.43	70
Telegraph_Peak_postsieve_dump	954	52.7	1.23	10.7	18.7	0.25	2.93	4.37	3.34	0.98	1.33	0.36	520	1230	2.54	0.30	40
Buckskin_post_sieve_dump_twk_corrected	1092	73.7	1.57	5.66	5.49	0.09	0.82	3.05	2.08	0.96	1.25	0.10	130	330	4.80	0.29	60
Big_Sky_postsieve_dump	1132	42.9	1.00	11.5	21.6	0.40	7.49	6.12	3.08	0.46	0.72	0.51	540	380	3.35	0.73	380
Greenhorn_postsieve_dump	1202	53.2	1.00	3.92	15.2	0.14	1.81	7.80	2.43	0.30	1.15	0.45	290	160	11.9	0.46	230
Gobabeb_DumpA_APXS	1226	47.9	0.88	9.78	17.9	0.37	7.57	7.30	2.75	0.49	0.79	0.39	440	200	3.36	0.50	20
Lubango_presieve_apxs	1326	59.7	1.11	3.09	8.22	0.09	1.55	8.22	1.92	0.31	1.33	0.29	110	90	13.7	0.32	60
Okoruso_postsieve_dump_apxs	1359	45.1	0.94	9.64	22.4	0.39	8.97	6.36	3.08	0.37	0.75	0.41	490	320	0.96	0.50	110
Oudam_presieve_dump	1368	51.8	1.05	9.40	18.7	0.22	4.90	4.55	2.59	0.87	0.52	0.32	770	1080	4.36	0.35	20
Marimba2_full_drill_tailings	1426	46.0	1.07	8.49	22.5	0.09	4.58	5.27	2.11	0.83	1.05	0.33	1080	1080	6.78	0.48	260
Quela_full_drill_tailings	1466	44.8	1.05	8.48	18.9	0.22	4.10	7.48	2.19	0.77	1.10	0.29	1000	830	9.30	1.01	40
Sebina_full_drill_tailings[3]	1496	46.2	1.10	8.68	18.3	0.16	4.25	7.13	2.01	0.83	0.61	0.30	1020	810	9.1	1.06	100
Ogunquit_Beach_postsieve_dump	1969	47.5	0.93	10.44	17.37	0.36	7.55	7.14	2.85	0.59	0.76	0.46	440	250	3.4	0.57	23
Duluth_DBA_dump_center	2080	42.9	1.05	7.81	22.1	0.21	2.66	7.52	2.24	0.94	1.11	0.32	920	1420	9.86	0.89	20
Stoer_dump_centre	2154	44.1	1.03	8.75	21.5	0.17	4.72	6.44	2.45	0.91	0.84	0.34	910	850	7.59	0.89	40
Highfield_dump_centre	2245	51.6	0.88	9.64	17.3	0.15	4.29	4.84	2.57	0.89	0.79	0.28	930	660	5.63	0.92	60
Rock_Hall_dump_corrected	2291	37.4	1.00	7.33	20.0	0.08	3.97	8.64	2.13	0.62	0.87	0.31	1000	920	15.28	2.10	230

[1] Note that the abbreviations listed here correspond with those discussed in presentations of results from CheMin (e.g., Bristow et al., 2018) and SAM (e.g., Sutter et al., 2018).
[2]See Table 2 for an explanation of preparation methods.
[3]Temperature indicates average temperature of the APXS sensor head chassis.
[4]Wind activity impacted the Sebina drill campaign. See supplemental text S1.
[5]Highfield_dump_offset on sol 2245 was of comparable quality and has small compositional differences.

Table 5: Statistical error for Table 4

Statistical (precision) error for analyses of drilled and scooped samples (Table 4)[1]

Target Name	Sol	SiO_2	TiO_2	Al_2O_3	FeO	MnO	MgO	CaO	Na_2O	K_2O	P_2O_5	Cr_2O_3	Ni ppm	Zn ppm	SO_3	Cl	Br ppm
PortageRP	89	0.5	0.05	0.19	0.2	0.02	0.25	0.08	0.14	0.02	0.07	0.03	30	20	0.10	0.03	10
APXS_Drill_Site_Raster_Integration_Site7	230	0.4	0.03	0.19	0.3	0.01	0.25	0.08	0.14	0.02	0.07	0.01	40	30	0.08	0.02	5
Cumberland_dump_pile_center	487	0.4	0.03	0.19	0.3	0.02	0.25	0.07	0.14	0.02	0.05	0.03	50	30	0.10	0.04	10
DumpPile_Windjana	704	0.4	0.03	0.19	0.3	0.01	0.25	0.06	0.07	0.10	0.05	0.01	30	150	0.05	0.01	5
Confidence_Hills_fines_postsieve_dump	781	0.5	0.05	0.29	0.3	0.01	0.17	0.06	0.14	0.04	0.07	0.01	50	70	0.08	0.02	5
Mojave2_postsieve_dump	894	0.5	0.05	0.29	0.2	0.01	0.17	0.06	0.14	0.02	0.07	0.01	60	70	0.08	0.02	5
Telegraph_Peak_postsieve_dump	954	0.5	0.05	0.29	0.2	0.01	0.08	0.06	0.14	0.04	0.07	0.01	30	40	0.05	0.01	5
Buckskin_post_sieve_dump_twk_corrected	1092	0.8	0.05	0.19	0.1	0.01	0.83	0.04	0.07	0.04	0.07	0.01	10	10	0.08	0.01	5
Big_Sky_postsieve_dump	1132	0.5	0.03	0.29	0.3	0.01	0.17	0.07	0.14	0.02	0.05	0.01	30	20	0.05	0.02	15
Greenhorn_postsieve_dump	1202	0.5	0.03	0.10	0.2	0.01	0.08	0.08	0.14	0.01	0.07	0.01	20	10	0.13	0.01	10
Gobabeb_DumpA_APXS	1226	0.5	0.03	0.29	0.2	0.01	0.17	0.08	0.14	0.02	0.05	0.01	20	10	0.05	0.01	5
Lubango_presieve_apxs	1326	0.6	0.05	0.10	0.1	0.01	0.83	0.08	0.07	0.01	0.07	0.01	10	10	0.15	0.01	5
Okoruso_postsieve_dump_apxs	1359	0.5	0.03	0.29	0.3	0.01	0.25	0.07	0.14	0.01	0.05	0.01	20	10	0.03	0.01	5
Oudam_presieve_dump	1368	0.5	0.03	0.19	0.2	0.01	0.17	0.06	0.14	0.04	0.05	0.01	40	40	0.05	0.01	5
Marimba2_full_drill_tailings	1426	0.5	0.03	0.19	0.3	0.01	0.17	0.06	0.07	0.04	0.07	0.01	60	40	0.08	0.02	10
Quela_full_drill_tailings	1466	0.5	0.03	0.19	0.2	0.01	0.08	0.08	0.14	0.02	0.07	0.01	50	20	0.13	0.02	5
Sebina_full_drill_tailings	1496	0.5	0.03	0.19	0.2	0.01	0.17	0.08	0.14	0.04	0.05	0.03	50	20	0.15	0.03	10
Ogunquit_Beach_postsieve_dump	1969	0.5	0.03	0.29	0.2	0.01	0.17	0.08	0.14	0.02	0.05	0.01	25	10	0.05	0.02	5
Duluth_DBA_dump_center	2080	0.5	0.03	0.19	0.3	0.01	0.08	0.08	0.07	0.04	0.07	0.01	50	50	0.10	0.02	5
Stoer_dump_centre	2154	0.5	0.03	0.19	0.3	0.01	0.17	0.07	0.14	0.04	0.05	0.01	50	30	0.10	0.02	5
Highfield_dump_centre	2245	0.5	0.03	0.29	0.2	0.01	0.17	0.07	0.14	0.04	0.05	0.03	50	30	0.13	0.03	5
Rock_Hall_dump_corrected	2291	0.4	0.03	0.19	0.3	0.01	0.08	0.10	0.07	0.02	0.05	0.01	50	30	0.17	0.03	10

[1]Concentrations are in wt% unless otherwise noted

SUPPLEMENTARY MATERIAL

Table S1: Summary statistics for APXS results sols 0-2301

The supplementary file named 'Berger_tableS2_apxs_summary_sol2301_v1.xlsx' contains a statistical summary the APXS results from sols 0-2301 with grouping by stratigraphic position and/or composition as defined in the text.

Table S2: Sulfur allocation to crystalline and amorphous fractions of drilled samples.

Table S2: Sulfur allocation to crystalline and amorphous fractions of drilled samples.

Unit	Drill targets	Bulk SO_3 (wt%)	Crystalline fraction SO_3 (wt%)	Amorphous fraction SO_3 (wt%)	Amorphous fraction (%)	Fraction of bulk S in the amorphous fraction (%)
Sheepbed member	JK, CB	5.26	3.02	10.77	25-30	53-67
Kimberley formation	WJ	3.57	0.87	13.95	20	80
Pahrump Hills member	CH, MJ, TP, BK	4.62	1.26	9.90	20-55	74-91
Stimson formation	BS	3.35	0.89	17.08	15	76
Stimson formation haloes	GH, LB	12.8	4.09	8.71	65-70	65-70

The allocation of SO_3 into crystalline and amorphous fractions is from (Morrison et al., 2018) and the mean SO_3 concentration is shown.

Figure S1: Traverse maps with APXS target locations.

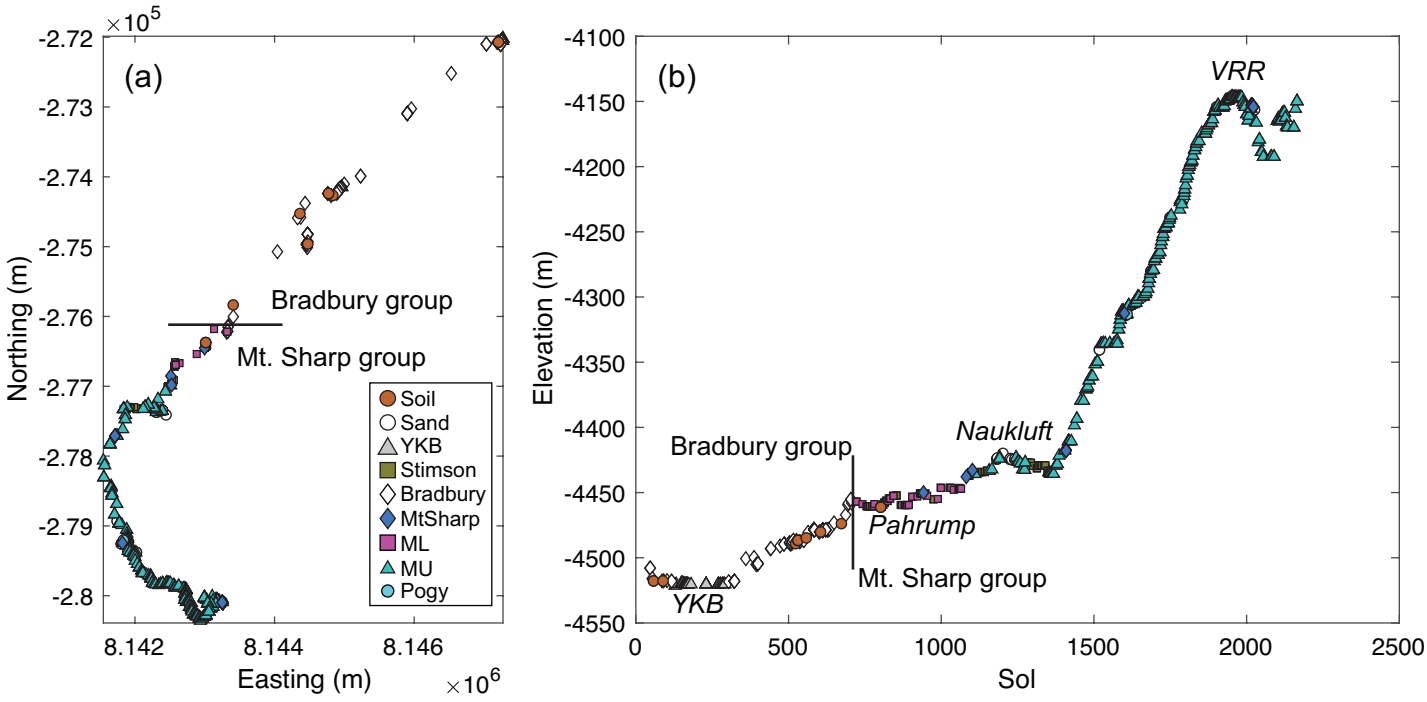

Figure S1: Traverse maps with APXS target locations (see also Figure 1). All APXS targets are shown. The contact between the Bradbury group and Mt. Sharp group and selected waypoints are denoted.

Figure S2: Example of a low-quality APXS spectrum.

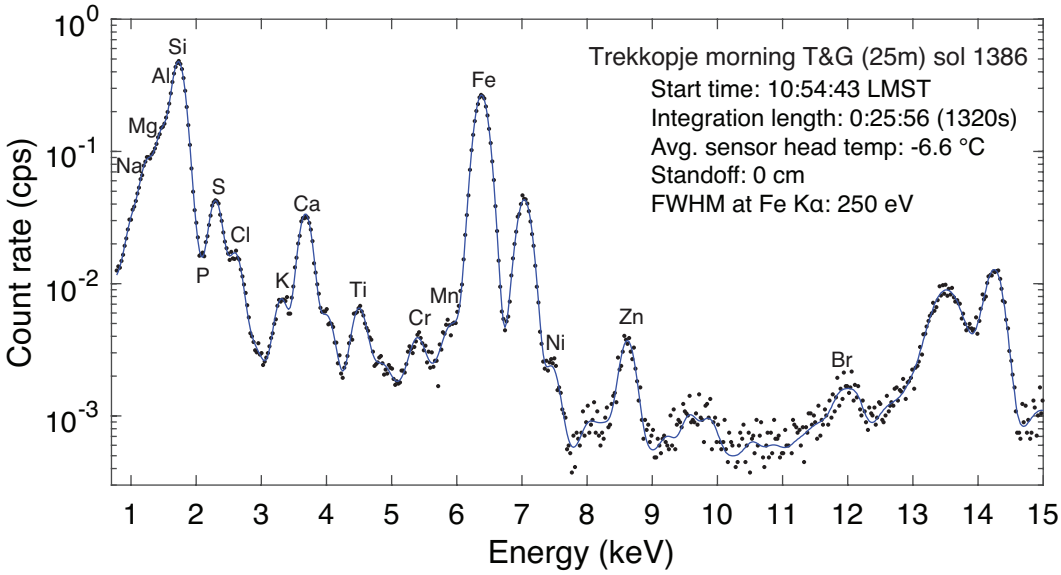

Figure S2: Example of a low-quality APXS spectrum. This spectrum was acquired on sol 1386 on the morning touch-and-go target Trekkopje. The morning temperature at ~11:00 was warmer than expected, resulting in low resolution with FWHM of Fe Kα = 250 eV. As resolution decreases, the LOD for minor and trace elements increases, and the peaks near the Si and Fe peaks have greater error and may not be detectable (Na, Mg, Al, P, Mn, Ni). Low-quality spectra are relatively rare because the tactical team works to ensure that APXS measurements are not planned when temperatures are warmer. Exceptions to this happen when the APXS is used for drill reconnaissance or when the temperature is unexpectedly warm. Nine low-quality measurements with FWHM of Fe Kα >250 eV have been acquired (~1% of the APXS database sols 0-2301), and these data should be given careful consideration with respect to the reported error. The locations of Kα peaks of the 16 elements reported in Tables 3 and S1 are indicated. The full APXS spectrum is not shown (15-25 keV omitted).

Figure S3: Images of the MSL APXS on Mars.

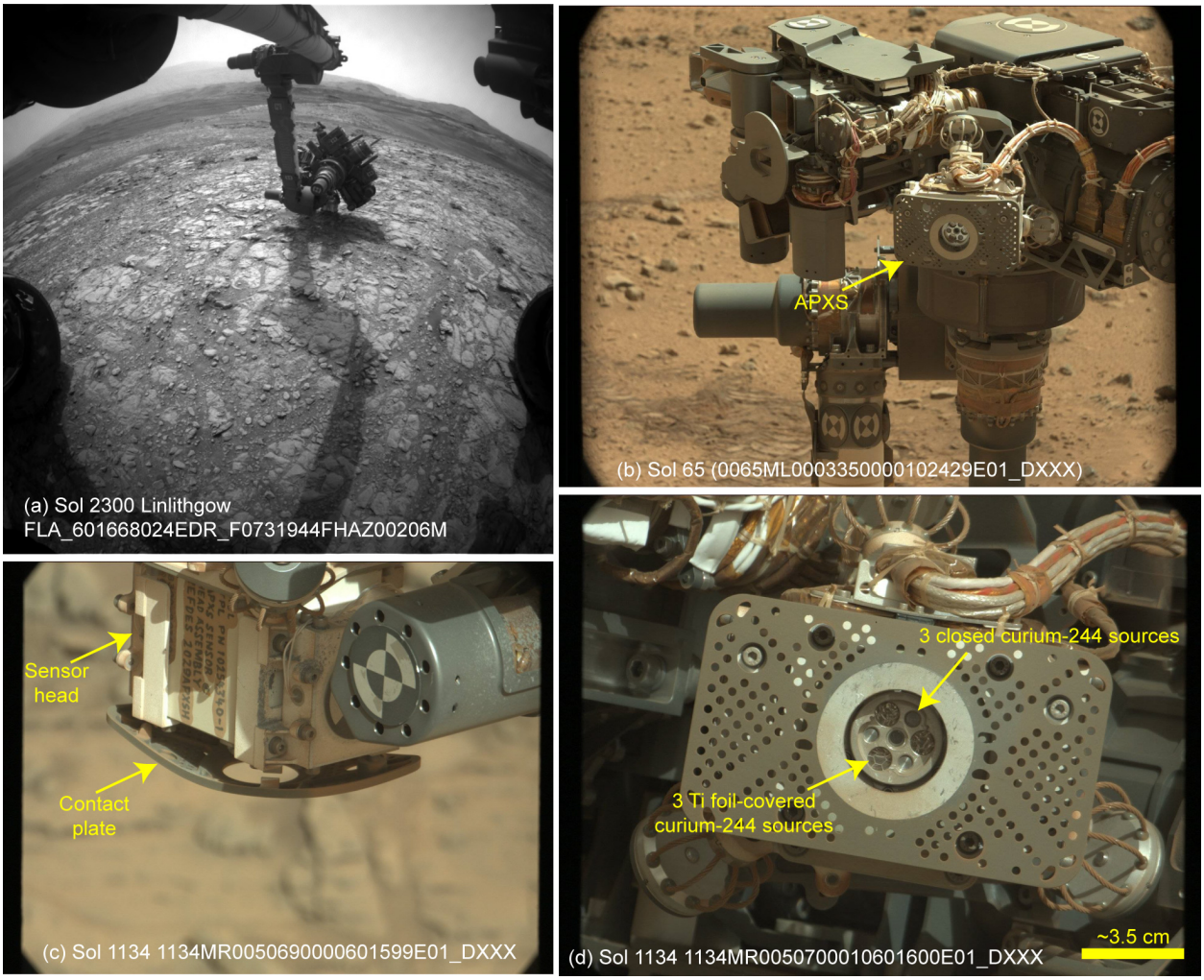

Figure S3: Images of the MSL APXS on Mars. (a) Front Hazard Avoidance Camera (Hazcam; Maki et al., 2012) image of the APXS deployed to the target Linlithgow on sol 2300. (b) Left Mastcam (Bell et al., 2017) image of the APXS on sol 65. (c) Right Mastcam image of the side of the APXS on sol 1134. (d) Right Mastcam image of the APXS contact plate and six curium-244 sources surrounding a central X-ray detector. Image numbers are shown.

Figure S4: Distribution of CaO and SO_3 in the Gale stratigraphy.

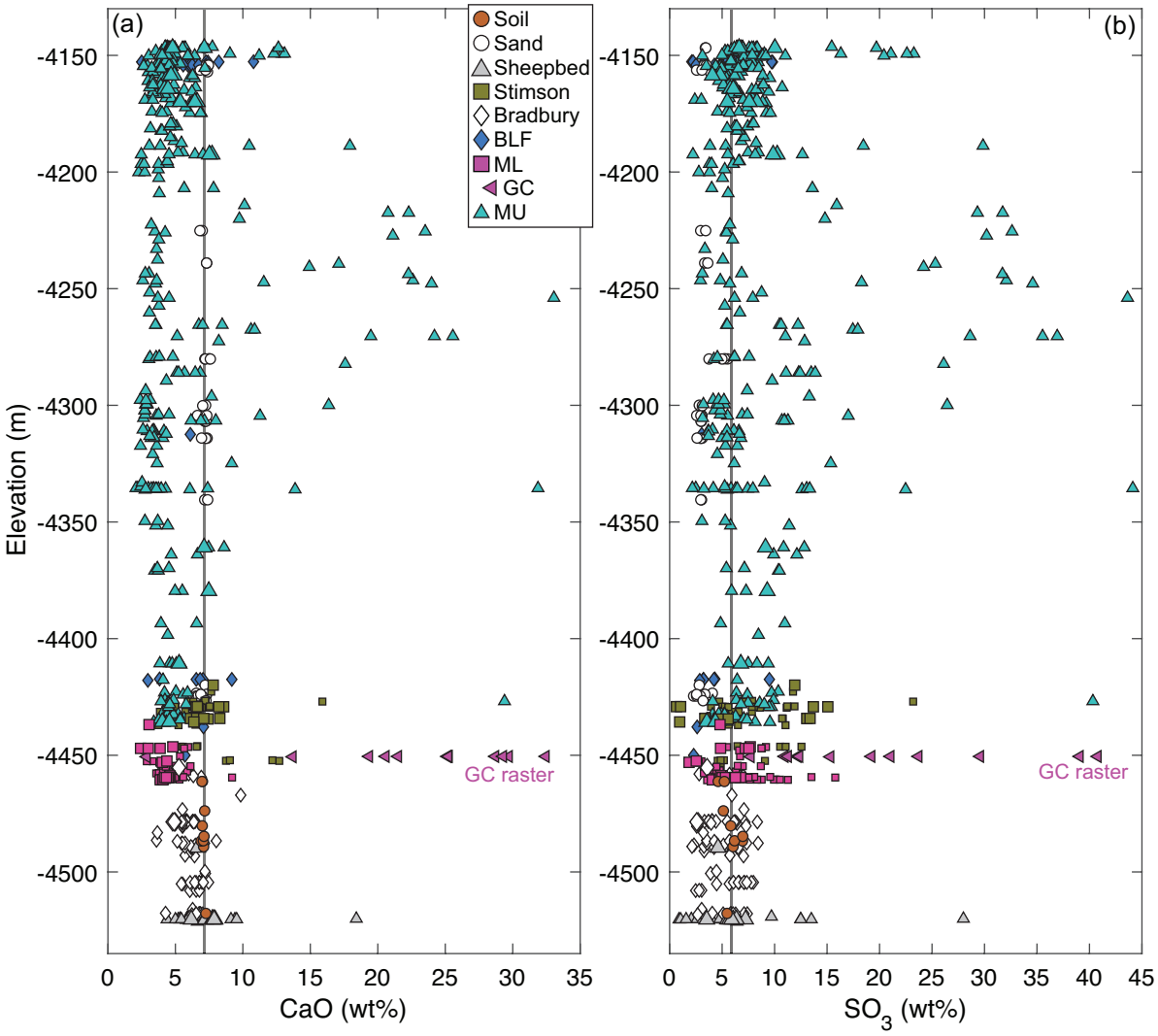

Figure S4: Distribution of (a) CaO and (b) SO_3 in the Gale stratigraphy. The vertical line indicates the average soil concentrations. The distribution of (Ca + S) enriched targets does not necessarily represent the actual distribution of veins because they are typically avoided by the rover operations team when possible. However, the common concordant veins of the Blunt's Point member (-4180 to -4280 m) are apparent because they were difficult to discern in targeting imagery and Ca-sulfates were more commonly enriched in SO_3. The Garden City vein raster is denoted (GC).

Figure S5: APXS rasters of Ni-rich nodules with evidence of Mg-sulfate.

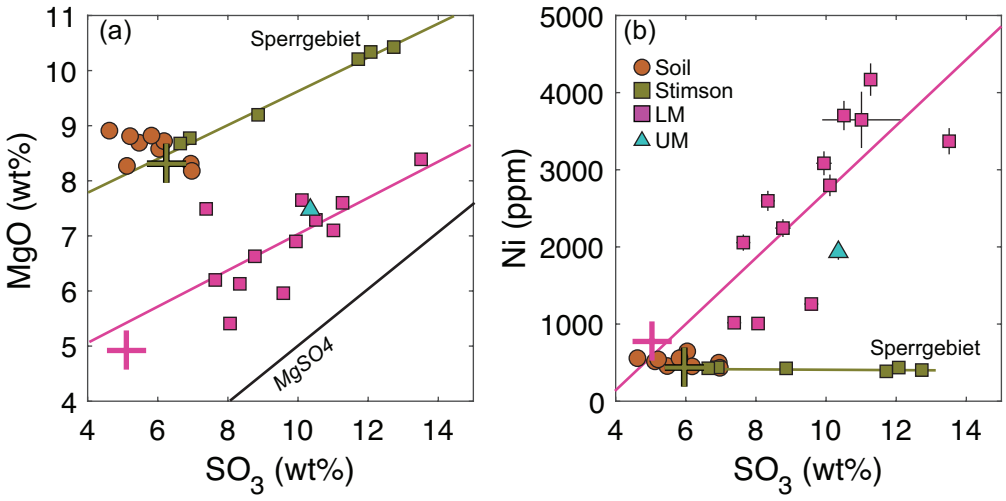

Figure S5: APXS analyses of nodules with evidence of Mg-sulfate. The targets include rasters of concretions found in the Pahrump Hills member (Morrison, Rosamond, Potatoe; sols 767-810) and one concretion located on Stimson bedrock at the Murray/Stimson contact at Naukluft plateau (Sperrgebiet; sol 1277). The MgO:SO_3 weight ratio inferred from linear fits to the rasters is 0.30 – 0.35, which is less than the MgO:SO_3 weight ratio of a pure $MgSO_4$ phase. The green and magenta crosses denote the median Stimson formation and LM bedrock, respectively. The green (m = 0.3; c = 6.7 wt%)) and magenta (m = 0.30; c = 3.6 wt%) lines are linear fits to the Stimson formation and LM nodules, respectively. The mixing line of pure $MgSO_4$ is shown (black).

Figure S6: MgO, CaO and SO_3 in Mt. Sharp drill fines.

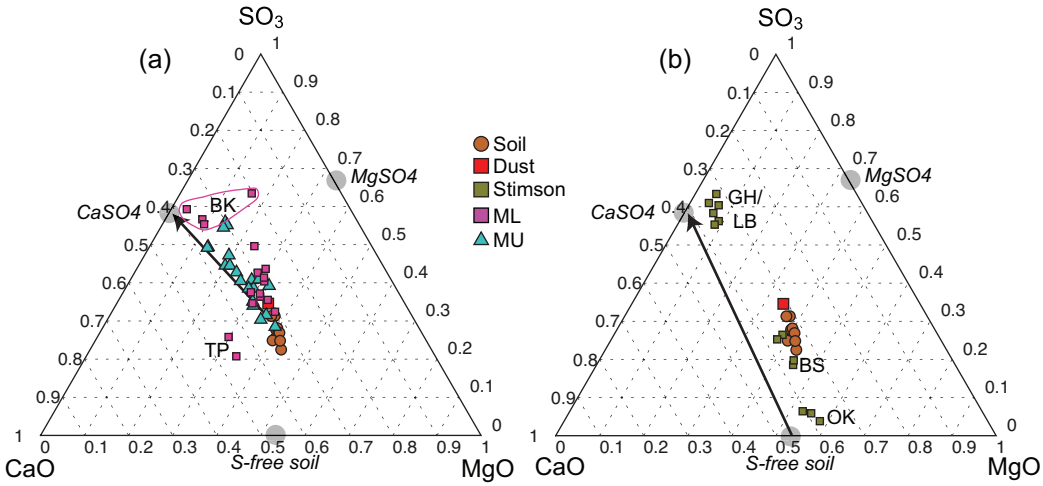

Figure S6: MgO, CaO, and SO_3 ternary for drill fines in the (a) Murray formation and (b) Stimson formation Select targets are indicated with abbreviations from Table 4. Pure $CaSO_4$ and $MgSO_4$ nodes are shown, as well as the sulfur-free soil composition with CaO/MgO ~0.5. The Ca-sulfate component dominates the sulfur trends, but not all of the sulfur is coupled with Ca, as indicated by the deviations from hypothetical $CaSO_4$ mixing trends (arrows).

Figure S7: Comparison of SO_3 in unbrushed, brushed, and drill fines targets.

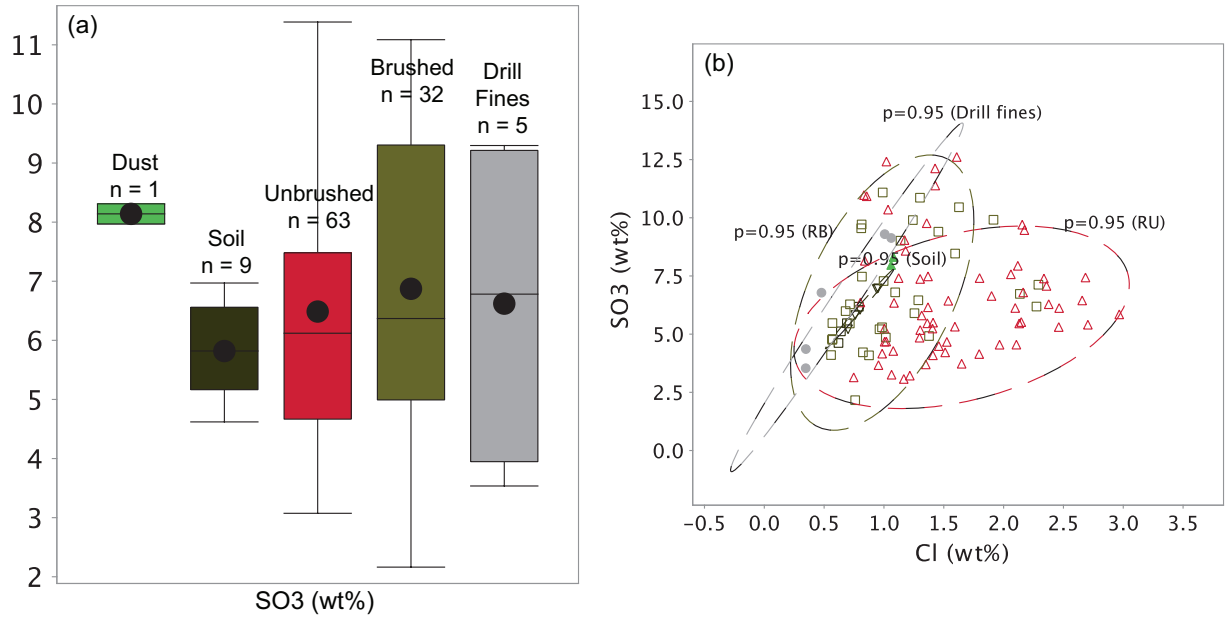

Figure S7: Comparison of SO_3 in unbrushed, brushed, and drill fines targets. (a) Tukey box plot comparison of SO_3 concentrations in unbrushed, brushed, and drilled bedrock. Only the Hartmann's Valley and Karasburg bedrock targets are shown, because all have low variability in elemental composition. Targets with Ca-sulfate veins are omitted. The number of targets (n) for each category is shown. The black circle is the mean, the line is the median, the central box is the middle 50% of data, the whiskers are extreme values and the symbols are outliers. (b) SO_3 versus Cl in the same targets shown in (a). Robust Mahalanobis ellipses are shown for each category in (a). These data suggest that there is no systematic difference in SO_3 content between unbrushed, brushed, and drill fines targets in bedrock with similar compositions. The key implications are (1) sulfur is a major component of most Gale bedrock units (>1 wt%) and (2) sulfur in APXS analyses is not simply due to modern airfall dust.

Figure S8: P_2O_5 versus CaO in Bradbury group rocks.

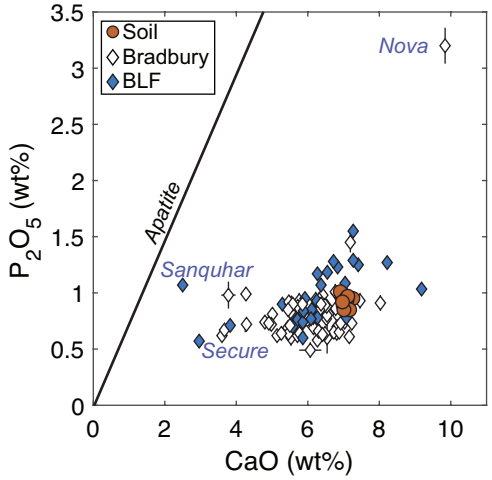

Figure S8: P_2O_5 versus CaO in Bradbury group rocks. All targets in the alkalic units of the Bradbury and Mt. Sharp groups are shown. The eight targets with low CaO (e.g., Sanquhar and Secure) correspond with the targets that deviate from the igneous Al/Si versus Mg/Si trend in Figure 7a. Nova, a unique, P-rich float rock analyzed on sol 687, is denoted. This rock is a loose fragment of float that was found during the traverse between the Kimberley and lower Mt. Sharp. Nova has elevated P_2O_5 and CaO at a P:Ca weight ratio consistent with the addition of apatite to an unaltered and/or isochemically altered igneous composition. Strontium is also enriched in Nova (300 ± 30 ppm), which is further evidence of apatite because Sr tends to substitute for Ca in the mineral. We interpret the composition of Nova to be that of an igneous rock with ~5% apatite. No other targets with this composition were discovered, and the origin and context are unknown. Nova was also the subject of a MAHLI and ChemCam investigation consisting of a series of images of the LIBS laser coupling with the target and generating plasma; no P peak was observed in the spectra, suggesting that the element is not distributed uniformly in the rock, but rather in grains that were not hit by the laser (O. Forni, personal communication).

Figure S9: Log plot of P_2O_5 versus MnO in Mt. Sharp rocks.

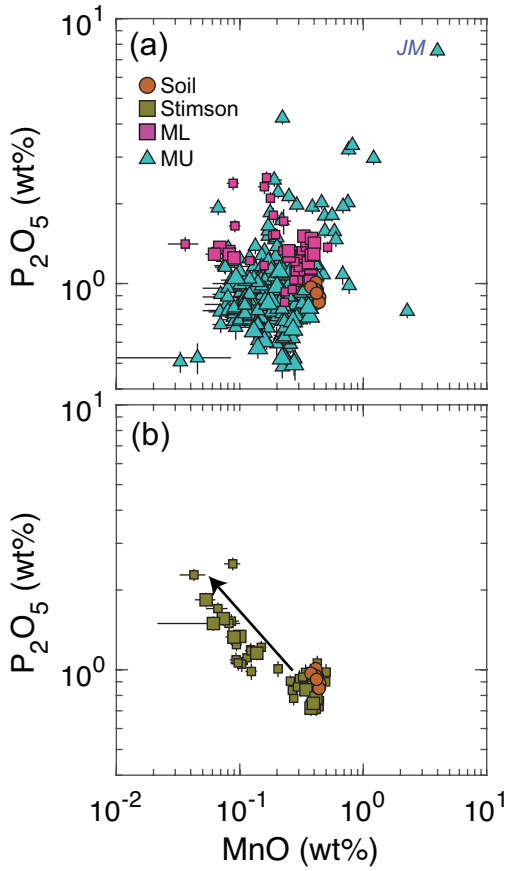

Figure S9: Log plot of P_2O_5 versus MnO in Mt. Sharp rocks. (a) The upper Murray formation bedrock (UM) has P-rich diagenetic features (see Figure 17), some of which have Mn enrichments (e.g., Jones Marsh; indicated by JM). MnO enrichments also occur without corresponding P_2O_5 enrichments. (b) The Stimson formation fracture haloes have enriched P_2O_5 and depleted MnO (arrow) indicating that the Mn leaching and P enrichment are related. The Mn and P observations indicate in situ mobilization of the two elements, but they are not necessarily coupled. Larger symbols denote drill targets.

Figure S10: Tukey box plot comparison of MgO, Mg/Si, and CaO of unbrushed, brushed, and drilled Murray formation bedrock.

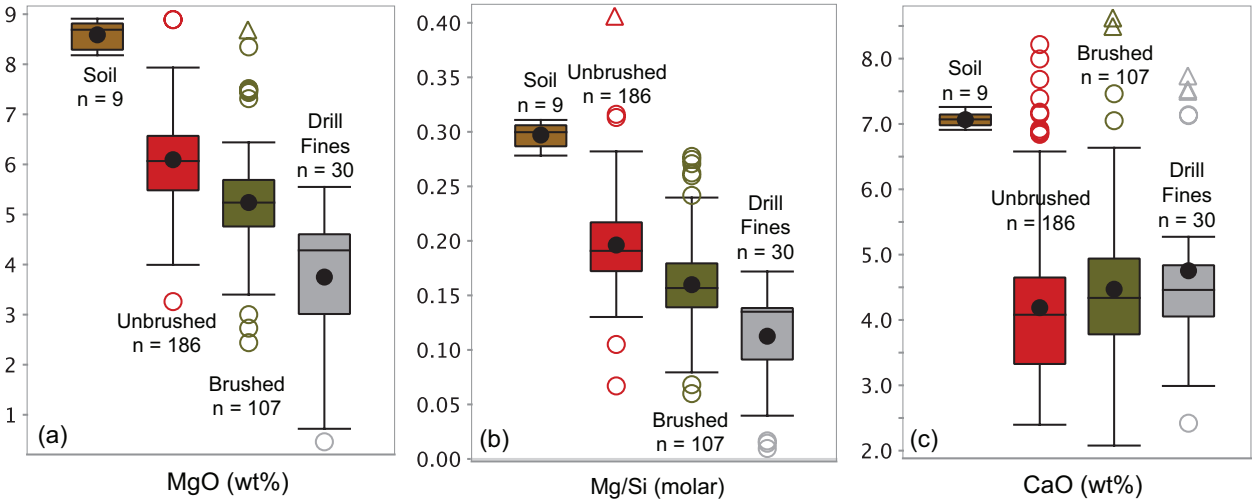

Figure S10: Tukey box plot comparison of MgO, Mg/Si, and CaO of unbrushed, brushed, and drilled Murray formation bedrock. All Murray bedrock targets without prominent Ca-sulfate veins are shown (< 9 wt% CaO and < 12 wt% SO_3). The number of targets (n) for each category is shown. The black circle is the mean, the line is the median, the central box is the middle 50% of data, the whiskers are extreme values and the symbols are outliers. The APXS analysis of unbrushed and brushed surfaces includes dust, which has the same MgO (8.3 ± 0.4 wt%) and Mg/Si (0.32 ± 0.02) as soil (Berger et al., 2016). The effective APXS sampling depth for Mg is ~4 µm, therefore, a thin layer of dust contributes to the Mg signal. The lower MgO in drill fines indicates that all Murray formation bedrock is depleted in MgO, relative to soil. The unbrushed and brushed targets in Figure 7b likely form a Mg/Si mixing line between depleted bedrock and dust. The effect of dust is not apparent in CaO, which is consistent with the greater effective APXS sampling depth for Ca (~10 µm); however, Ca-sulfate in small veins and/or the bedrock matrix adds uncertainty to this conclusion (see Figure 12).

Figure S11: Igneous models full scale for comparison.

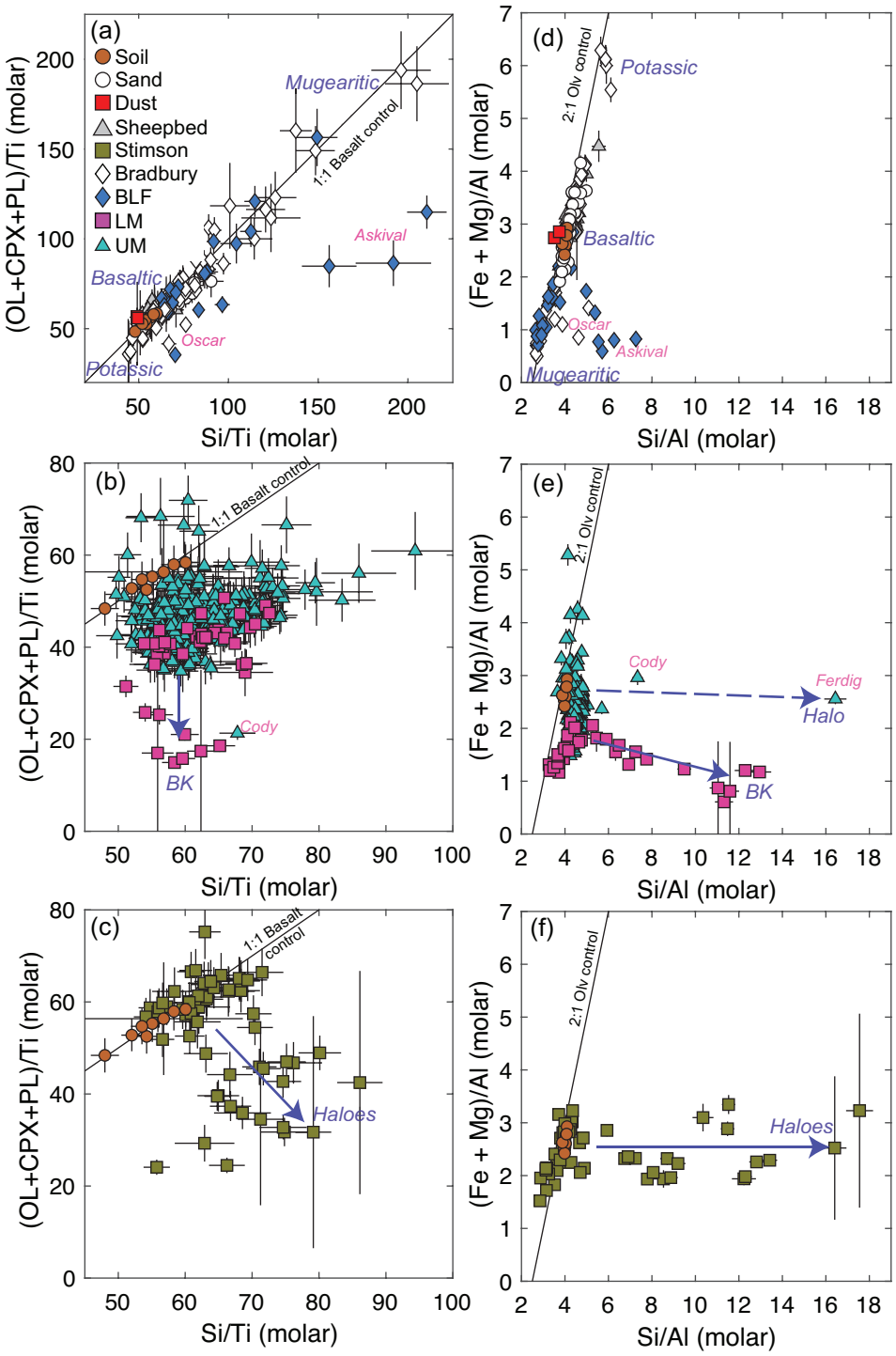

Figure S11: This figure is the same as Figure 19; however, it shows the full range of fracture haloes and the Buckskin unit.

Figure S12: Igneous geochemical trends in Mauna Kea whole rock samples.

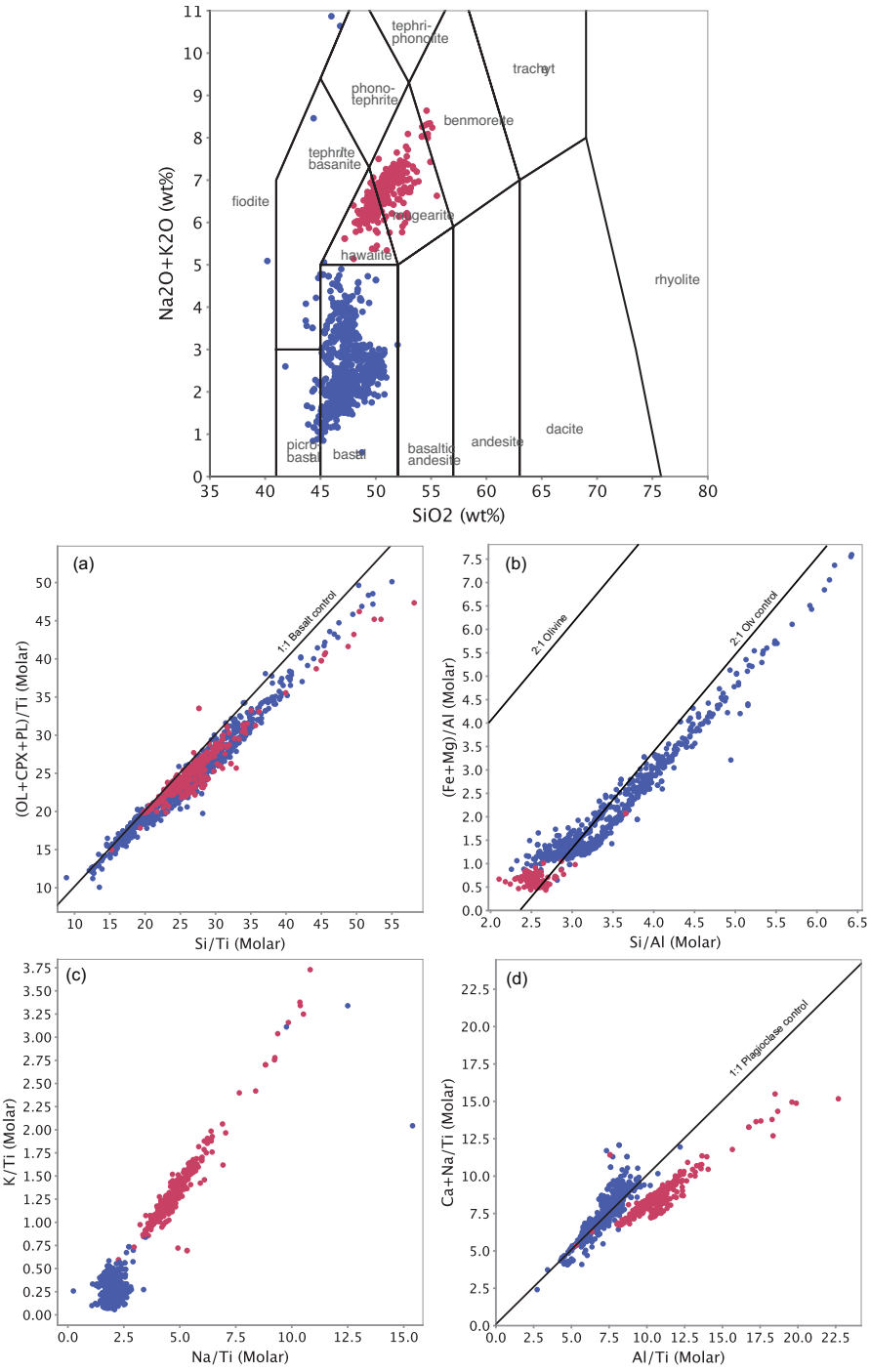

Figure S12: Igneous geochemical trends in Mauna Kea post-shield volcanic whole rock samples. Red and blue symbols denote higher- and lower-alkali content as shown in the TAS classification diagram. Note that Ti is higher in the Mauna Kea rocks and the Ti-normalized absolute values are thus lower than in Gale crater APXS data; nevertheless, the element ratio trends are comparable. Data are from Georoc.

Supplementary text S1: Silica deconvolution model testing silica addition

Hurowitz et al. (2017) developed a model for the Pahrump Hills compositions of Telegraph Peak and Buckskin based on elemental trends in a plot of CIA versus silica. The hypothesis is that the silica-rich Buckskin composition is due to the simple addition of Ca-sulfate and silica to a rock with a Telegraph Peak composition.

We applied this model using a linear, least-squares deconvolution (Matlab script included below) to test how accurately it reflects the bulk composition of Buckskin. The sums in Tables S2-1, S2-2, and S2-3 are near 1, which is evidence that the deconvolution can be used to calculate plausible model compositions. The estimate of 0.30 of Telegraph Peak is in agreement with the Hurowitz estimate. Using these fractions, the model composition of each Buckskin target was calculated and normalized to 100 wt% (Table S2-4). Results are shown in Figure 21. We conclude that the modeled compositions are significantly different than the measured compositions (Figure 21). This simple addition model does not capture the elevated Ti, Na, K, and P. Nor does it properly predict the degree to which Ni and Zn are depleted.

```
% Adapted from the Ramsey and Christensen 1998 spectral deconvolution model
from eq. 4

Endmember matrix input
Oxide Telegraph_Peak_postsieve_dump silica      Ca-sulfate
"SiO2_pct"      52.7       100  0
"TiO2_pct"      1.23       0    0
"Al2O3_pct"     10.74      0    0
"FeO_pct"       18.68      0    0
"MnO_pct"       0.24       0    0
"MgO_pct"       2.93       0    0
"CaO_pct"       4.37       0    41
"Na2O_pct"      3.34       0    0
"K2O_pct"       0.98       0    0
"P2O5_pct"      1.33       0    0
"Ni_pct"        0.051      0    0
"Zn_pct"        0.12       0    0
```

```
"Ge_pct"        0.0141     0     0
"Cr2O3_pct"     0.36       0     0
"SO3_pct"       2.54       0     59
"Cl_pct"        0.3        0     0
```

```
X = % endmember matrix oxides
U = %enter in unk matrix of Buckskin targets

fraction = (X' * X)^(-1) * (X' * U); % calculates fraction of each endmember
in the unknown and makes a matrix with each row corresponding to an endmember
and each column corresponding to an unknown


%% generate the model and residuals

model = zeros(length(U), length(fraction));
R = zeros(length(U), length(fraction));

n = length(fraction);
i = 1;
for i = 1:n

    model(:, i) = (fraction(1, i) * X(:, 1))...
        + (fraction(2, i) * X(:, 2))...
        + (fraction(3, i) * X(:, 3));
end

R(:, :) = model(:,:) ./ U(:, :); %calculates R value = Model/Actual
```

Table S2-1: Linear least squares deconvolution results for the Murray formation targets.

Target name	Fraction of Telegraph_Peak_postsieve_dump	Fraction of Silica	Fraction of Ca-sulfate	Sum
Buckskin_DRT_raster2	0.34	0.50	0.09	0.93
Buckskin_mini_start_hole	0.28	0.57	0.11	0.96
Buckskin_Full_Drill_Tailings_APXS	0.29	0.57	0.09	0.95
Buckskin_presieve_dump	0.33	0.57	0.06	0.96
Buckskin_post_sieve_dump_twk_corrected	0.36	0.55	0.06	0.96

Table S2-2: Linear least squares deconvolution results for the Stimson altered halo (Big Sky/Greenhorn) targets.

Target name	Fraction of least altered bedrock Big_Sky_postsieve_dump	Fraction of Silica	Fraction of Ca-sulfate	sum
Greenhorn_full_drill_tailings	0.40	0.42	0.17	0.99
Greenhorn_presieve_dump	0.50	0.32	0.18	1.00
Greenhorn_post_dump_offset	0.58	0.28	0.14	1.01
Greenhorn_postsieve_dump	0.59	0.28	0.15	1.01

Table S2-3: Linear least squares deconvolution results for the Stimson altered halo (Okoruso/Lubango) targets.

Target name	Fraction of least altered bedrock Okoruso_postsieve_dump_apxs	Fraction of Silica	Fraction of Ca-sulfate	Sum
Lubango_fulldrill_tailings	0.18	0.56	0.23	0.96
Lubango_presieve_apxs	0.33	0.45	0.20	0.98

Table S2-4: Modeled compositions (wt% unless denoted ppm) of Buckskin targets.

Model renormalized	Buckskin_DRT_raster2	Buckskin_mini_start_hole	Buckskin_Full_Drill_Tailings_APXS	Buckskin_presieve_dump	Buckskin_post_sieve_dump_twk_corrected
SiO_2	72.99	74.72	76.24	77.59	76.55
TiO	0.45	0.36	0.38	0.43	0.46
Al_2O_3	3.91	3.18	3.33	3.72	4.00
FeO	6.80	5.54	5.79	6.47	6.96
MnO	0.09	0.07	0.08	0.09	0.09
MgO	1.07	0.87	0.91	1.01	1.09
CaO	5.61	5.92	5.09	3.99	4.02
Na_2O	1.22	0.99	1.04	1.16	1.25
K_2O	0.36	0.29	0.30	0.34	0.37
P_2O_5	0.48	0.39	0.41	0.46	0.50
Ni (ppm)	0.02	0.02	0.02	0.02	0.02
Zn (ppm)	0.04	0.04	0.04	0.04	0.05
Ge (ppm)	0.01	0.00	0.00	0.00	0.01
Cr_2O_3	0.13	0.11	0.11	0.12	0.13
SO_3	6.71	7.41	6.17	4.45	4.39
Cl	0.11	0.09	0.09	0.10	0.11